Kobe University Repository : Kernel

PDF issue: 2024-08-17

Development of Monte Carlo Simulators for Integrated Nanoscale Devices

Koba, Shunsuke

(Degree)
博士（工学）

(Date of Degree)
2014-03-25

(Date of Publication)
2015-03-01

(Resource Type)
doctoral thesis

(Report Number)
甲第6095号

(URL)
https://hdl.handle.net/20.500.14094/D1006095

※ 当コンテンツは神戸大学の学術成果です。無断複製・不正使用等を禁じます。著作権法で認められている範囲内で、適切にご利用ください。

Doctoral Dissertation

Development of Monte Carlo Simulators for Integrated Nanoscale Devices

ナノスケール集積デバイスの
モンテカルロシミュレータの開発

January, 2014

Graduate School of Engineering
Kobe University

Shunsuke Koba

木場 隼介

Abstract

Until recently, downscaling of the MOSFETs based on Dennard's scaling law has been the most effective way to improve integrated circuit device performance. However, as a result of miniaturization for over 50 years, the device size has become nanoscale, and VLSI technology has confronted many problems. Not only short channel effects such as drain induced barrier lowering and threshold voltage roll-off but also discrete impurity dopant fluctuation in the channel region has become significant, and performance improvement of VLSI depending only on the scaling law has been becoming increasingly difficult. Moreover, problems caused by quantum mechanical effects such as gate leakage current across the gate oxides and source-to-drain (SD) tunneling, impact by increased acoustic phonon scattering and surface roughness scattering caused by spatial fluctuation of quantized subbands, both of which are more significant in silicon-on-insulator (SOI) structure and double gate (DG) structure, and the effects of ballistic transport, which is enhanced because of decreased scattering number in the channel, have come into being. Though all of them are very important phenomena which determine the limit in miniaturization of MOSFETs, neither of them can't be described by the classical drift-diffusion model, which was the basis of the current LSI design technology.

To cope with the situation, introduction of new device structures and new device materials have been gaining much attention as the technologies which don't depend only on the miniaturization. In the research and development activities for such future integrated nanoscale devices, a device simulator that has the ability to describe aforementioned new physical phenomena precisely and to simulate new device structures and new materials is indispensable. However, such comprehensive device simulation method has not been proposed yet. Therefore, this thesis focused on the development of simulators which satisfy such demands.

First, to focus on the modeling of the scattering mechanisms, a semi-classical MC simulator which can fully incorporate major scattering mechanisms for 2D electron gases (2DEGs), with increase in acoustic phonon deformation potential and spatial fluctuation of quantized subbands taken into account, is developed. To focus on the scattering treatment, quantum transport effect along the source-to-drain direction is ignored. To describe electron transport in the inversion-layers, electron states are obtained by self-consistently solving 1D Schrödinger equation and Poisson's equation along the gate-to-substrate direction, and the results are combined with the 1D MC simulator along the transport direction with the phonon scatterings and surface roughness scatterings.

The validity of the simulator is demonstrated by comparisons with the experimental results of electron mobility in bulk MOSFET and SOI MOSFETs. As a result, it is shown that reliable scattering modeling is constructed.

Furthermore, the simulator is extended to 2D semi-classical MC method for the DG MOSFETs with a significant improvement in the treatment of source and drain electrode which enables us to estimate subthreshold characteristics, which is regarded next to impossible using MC simulator. A new approach to directly calculate the quasi-ballistic transport parameters for ultrasmall DG MOSFETs is also proposed. The

results have demonstrated that the ballistic transport in DG MOSFETs is enhanced due to channel length (L_{ch}) scaling until L_{ch} = 10 nm, but when L_{ch} is further scaled to less than 10 nm, SR scattering intensified by spatial fluctuation of quantized subbands drastically degrades ballistic transport. The results indicate that performance improvement is difficult even if MOSFETs are scaled less than 10 nm, which is very important viewpoint for the discussion of the miniaturization limits.

Next, a quantum-mechanics-based MC simulator is developed for rigorously incorporating quantum transport effect along the source-to-drain direction. The simulator is based on Wigner transport equation (WTE) and the method is called 'Wigner Monte Carlo (WMC)' simulator. WMC method solves WTE using MC algorithm and incorporates not only scattering effects but also quantum transport effects more precisely. Therefore, the method is thought to have the ability suitable for the simulation of integrated nanoscale devices. This study is the first successful attempt of WMC simulation in Asia. Furthermore, the WMC quantum simulation method is extended to multi-subband (MS) simulation and effects of quantum transport effects in silicon DG MOSFETs with channel length of less than 10 nm are investigated. As a result, it is demonstrated that the quantum reflection makes significant differences in the microscopic features of electron transport and can even reduce the drain current at on-state. On the other hand, SD tunneling is shown to play a crucial role in the subthreshold properties of scaled MOSFETs with channel lengths of less than 6 nm.

Finally, in order to demonstrate the applicability of WMC method to new channel material MOSFETs, III–V channel MOSFETs are simulated. III–V compound semiconductors are expected to replace Si as the channel material in n-channel MOSFETs because of their lower transport effective mass and higher electron mobility than Si. Therefore, treatments of conduction band structure in III-V MOSFETs and polar optical phonon scattering, which is intrinsic to the compound semiconductor materials, are described, and the treatments are incorporated to WMC simulator in order to investigate the impact of SD direct tunneling in III–V channel MOSFETs with $In_{0.53}Ga_{0.47}As$ and InP. As a result, it was found that subthreshold current increase due to SD direct tunneling becomes more remarkable in both $In_{0.53}Ga_{0.47}As$ and InP MOSFETs, owing to its considerably lower effective mass compared to Si. In addition, the critical channel length for which a drastic increase in subthreshold current occurs due to SD direct tunneling was found to be about 20 nm for both $In_{0.53}Ga_{0.47}As$ and InP MOSFETs. Since this value is significantly larger than that for Si MOSFET, SD direct tunneling can be a major obstacle to downscale III-V MOSFETs into L_{ch} < 20 nm.

Hence, to go beyond the end of the roadmap, we will need a material selection for suppressing SD direct tunneling while maintaining the high current drivability. We suggested that the choice of a material with a heavier transport mass might be one option.

Table of contents

1. Introduction

This chapter provides an introduction and overview of the research conducted in this dissertation. Section 1.1 describes overview of device scaling and its challenges. In Section 1.2, counter measures to cope with the challenges are described. Section 1.3 introduces conventional device simulators and its challenges. In section 1.4, objectives of this thesis are presented. Section 1.5 describes the organization of the remainder of this dissertation.

1.1 Overview of device scaling

1.1.1 Device performance and mobility universal curve

A Device structure of a MOSFET and its use in integrated circuits

Figure 1.1 (a) shows the fundamental device structure of a metal-oxide-semiconductor (MOS) field-effect transistor (FET). Whether n-channel MOSFET (nMOS) or p-channel MOSFET (pMOS), flow of carriers through the channel (electrons for nMOS and holes for pMOS), and therefore current density, are controlled by switching the gate voltage V_G on and off. In the integrated circuits, as shown in Fig. 1.1 (b), a pair of nMOS and pMOS, which is called complementary MOS (CMOS), is the most basic construction of the switching devices. CMOS structure has an advantage that a non-operating CMOS cell doesn't cause power consumption. Therefore, CMOS-based integrated circuits are the most widely used among various options of switching devices.

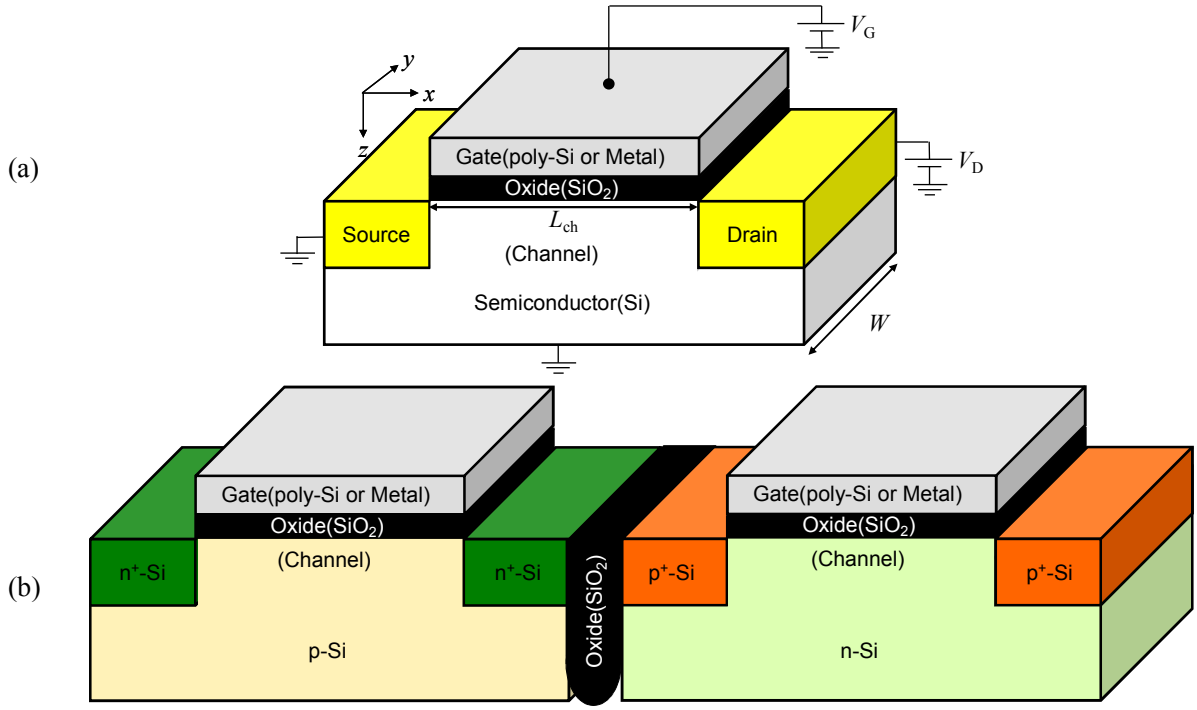

Fig. 1.1 Device structure of (a) a MOSFET and (b) a CMOS structure.

B Relation between carrier mobility and device performance

Carriers in semiconductor materials or MOSFETs don't move freely. Their movement is affected by the arrayed crystal atoms, which determines the band structure and effective mass. Quantization of the crystal atom vibrations, which is called phonons, impurities in the crystal, and lattice defects cause the scattering of carriers. Also in MOS structure, surface roughness (SR) on Si/SiO_2 interface also causes scattering. Therefore, carriers in the devices are constantly scattered by these scattering mechanisms. Averaged interval between successive scattering events is called mean-free-time τ. If there is no scattering, carriers are unlimitedly accelerated by the electric field, but in reality, carrier velocity has finite value due to scattering events. If electric field is sufficiently low, relation between carrier velocity and electric field is expressed as follows:

$$\mathbf{v} = \mu \mathbf{E}, \tag{1.1}$$

where $\mathbf{v}$ is a velocity vector and $\mathbf{E}$ is an electric field. μ is a quantity called mobility, which is defined as

$$\mu \equiv \frac{q\tau}{m^*}, \tag{1.2}$$

where, q is elementary charge, m^* is the effective mass of the material, and τ is the mean-free-time. Drain current of the long-channel MOSFET is approximated using mobility μ as [1]

$$I_D = \begin{cases} \mu \cdot C_{OX} \cdot \dfrac{W}{L_{ch}} \cdot \left((V_G - V_{th}) \cdot V_D - \dfrac{1}{2} \cdot V_D^2 \right), & (V_G - V_{th} < V_D) \\ \mu \cdot C_{OX} \cdot \dfrac{W}{L_{ch}} \cdot \dfrac{(V_G - V_{th})^2}{2}, & (V_G - V_{th} \geq V_D) \end{cases} \tag{1.3}$$

where C_{OX} is capacitance of the oxide and V_{th} threshold voltage of the MOSFET. W, L_{ch}, V_G, and V_D are indicated in Fig. 1.1. As shown in Eq. (1.3), within the same technology node and operating voltage, performance of MOSFETs is determined by mobility. Therefore, mobility is regarded as the barometer of the channel material.

C Mobility universal curve

Mobility for the bulk Si crystal is known to be 1300–1500 cm^2/Vs [1], which is determined by phonon scatterings. On the other hand, mobility in the Si MOSFET is known to be significantly lower than the bulk mobility [2]. This is because, if MOS structure is formed, other scattering mechanisms such as SR, ionized impurities, and scattering due to lattice defect also affects the mean-free-time of carriers. Not only that, mobility determined by phonon scattering is known to be dependent on the electric field along the depth direction of the MOS structure.

As a result, mobility in Si MOSFET is substantially degraded compared to bulk Si crystal, and has dependency on the electric field applied in the depth direction. The electric field is called effective field E_{eff}. Among the scattering mechanisms, Coulomb scattering in the low effective field E_{eff}, phonon scattering in all E_{eff} region, and SR scattering in mid- and high-E_{eff} region play significantly important role in determination of carrier mobility for bulk MOSFETs.

Fig. 1.2 demonstrates this situation, and the curve is called mobility universal curve. In particular, for operating range of MOSFETs, phonon and SR scatterings have significant effect on the device performance. Therefore, precise estimation of device performance requires inclusion of scattering by both of them.

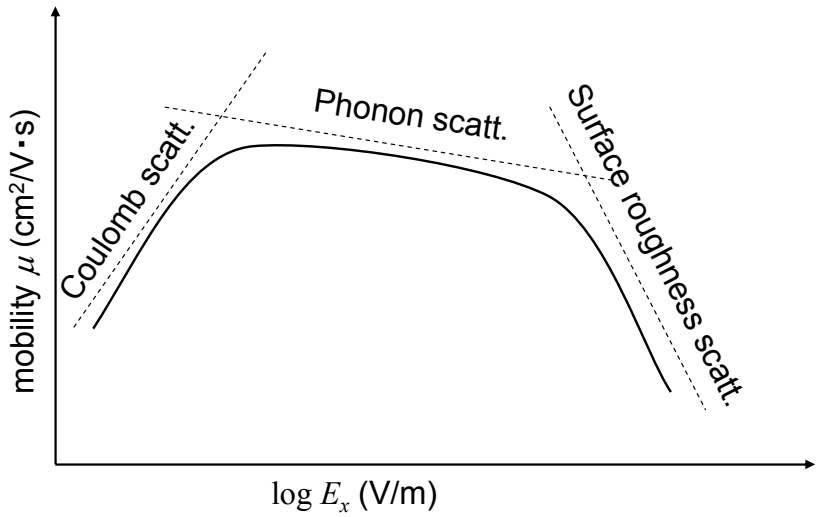

Fig. 1.2 Schematic view of mobility universal curve [2].

1.1.2 Device scaling, short channel effects, and ballistic transport

A. Dennard's scaling law and short channel effects

For more than fifty years since the invention of transistor by W. Shockley, J. Bardeen, and W. H. Brattain, downscaling of the MOSFETs based on Dennard's scaling law [3], as is shown in Fig. 1.3, has been the most effective way to improve integrated circuit device performance. Table 1.1 shows the changes in the device parameters if a device is miniaturized according to constant electrical field scaling model. If electrical field isn't kept constant, transverse and longitudinal electric fields become too high as devices are scaled down. As a result, insulation breakdown occurs, or current drive controllability is lost due to punch-through current. Constant

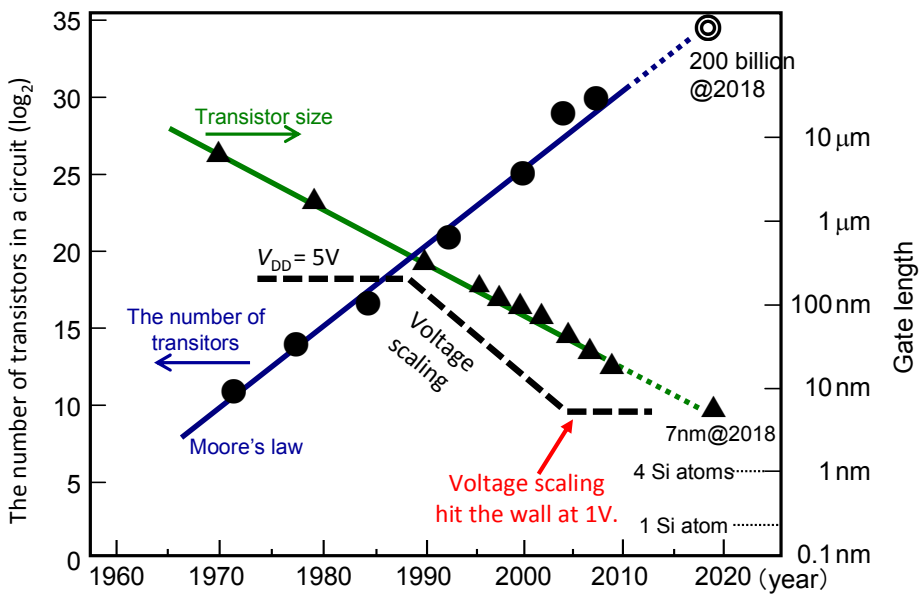

Fig. 1.3 Scaling trend of Si MOSFETs (Moore's law).

TABLE 1.1: Device parameters.

Device parameters	Scaling factor
Gate length L_G	$1/k$
Gate width W	$1/k$
Gate oxide thickness T_{OX}	$1/k$
Junction depth x_j	$1/k$
Substrate impurity density N_A	k
Voltage V (V_G, V_D, V_{th})	$1/k$
Electric field E	1

TABLE 1.2: Performance parameters.

Performance parameters	Scaling factor
Current density I	$1/k$
Gate capacitance C_G	$1/k$
Delay time CV/I	$\mathbf{1/k}$
Power consumption $P=VI$	$1/k^2$
Power density P/A	**1**

electric field scaling is necessary to avoid such situations. However, an important conclusion of Dennard's scaling law consists not only in the constant electric field premise itself but also in the improvement of operation speed while keeping power density constant, as shown in Table 1.2. In spite of many past predictions on the limitation of device scaling, device processing node has reached as small as 22 nm. However, as the device size becomes small, not only mobility degradation discussed above but also short channel effects such as the drain-induced barrier lowering (DIBL) and the threshold voltage (V_{th}) roll-off have been becoming more significant due to gate control degradation. As a result, increase in leakage current and V_{th} variation has become influential to the correct operation of integrated circuits.

Also, gate leakage current across the gate oxides can't be ignored any longer in terms of static power consumption, becoming obstacles of miniaturization.

B. Ballistic transport

Furthermore, it is common view that ballistic transport is enhanced for ultrashort channel devices. Fig. 1.4 shows a concept of ballistic transport. Ballistic transport is characterized by the relation between mean-free-path λ and the channel length L_{ch} of the MOSFET. Inside Si channel, the value of λ is known as a few nm to not more than 20 nm, though the value is significantly dependent on the kinetic energy of carriers. When channel length was long enough compared to mean-free-path λ, electron transport is governed by scattering. Hence, device performance is determined by mobility μ. However, in ultimately scaled devices, the number of scattering events

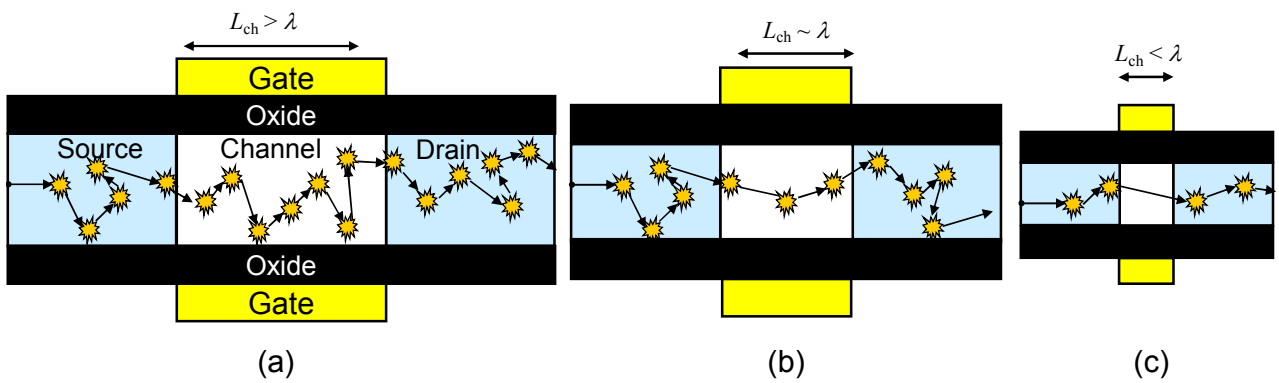

Fig. 1.4 A picture of quasi-ballistic transport of carriers. (a) diffusional transport regime, (b) quasi-ballistic regime, and (c) ballistic regime.

during the transport decreases. If channel length is short enough compared to mean-free-path λ, electron can pass through the channel without a single scattering. This is the concept of ballistic transport. Also, a situation that electrons pass through the channel with a few times of scattering events is called quasi-ballistic transport. At any rate, ballistic transport has been expected to boost device performance of MOSFETs, while a picture of carrier transport in MOSFETs is drastically changed. According to ref. 1, drain current in the quasi-ballistic transport regime is expressed using an injection velocity v_{inj} and a backscattering coefficient R, instead of conventional mobility μ and saturation velocity v_{sat}.

On the one hand, SOI or DG MOSFETs with an intrinsic channel are considered to have an advantage to achieve ballistic transport, because impurity scattering is absent in the channel region [4]. On the other hand, such ultrathin channel devices suffer from an increased acoustic phonon (AP) scattering and a new type of SR scattering caused by spatial fluctuation of quantized subbands [5]. Therefore, performance prediction in the quasi-ballistic MOSFETs is thought to be more difficult than ever.

1.2 Introduction of new structures and new channel materials

1.2.1 New structures for nanoscale MOSFETs

To cope with such situations, technology boosters have been intensively researched and introduced. Before introducing technology boosters, electron state in Si is briefly explained.

Si has six equivalent elipsoidal valleys near X points of the bandstructure, and in <110>-oriented and (001) confined Si, these six valleys are distinguished by transport effective mass as 2-fold valleys and 4-fold valleys with smaller and larger transport mass, respectively, as shown in Fig. 1.5 (a). In Si channel, an inversion layer is formed, where electrons are confined in the triangular potential as shown in Fig. 1.5 (b). In the triangular potential, electrons lose degrees of freedom along the depth direction due to the confinement effect. As is well known from

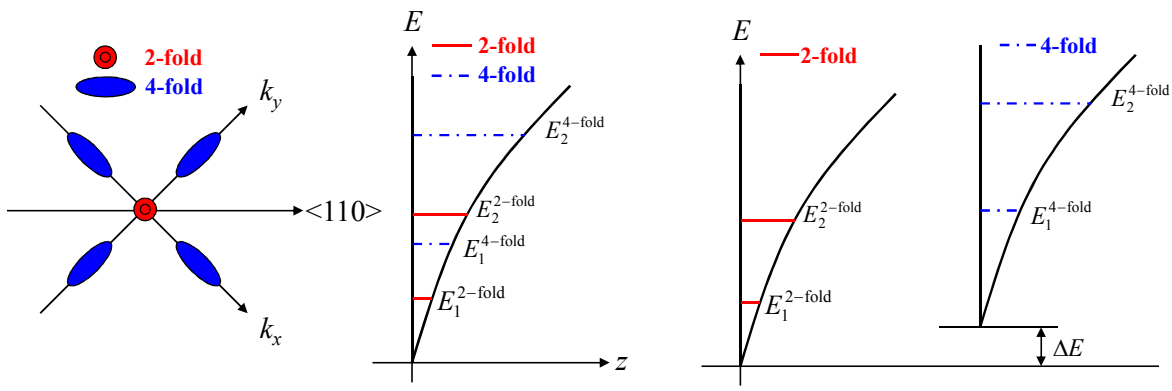

(a) (b) (c)

Fig. 1.5 (a) Conduction band structure of <110>-oriented and (100) confined Si used in the simulation, and (b) typical subband splitting caused by confinement, where $E_n^{2-\mathrm{fold}}$ and $E_n^{4-\mathrm{fold}}$ denote eigen energies of n-th subband in 2– and 4–fold valleys. (c) Schematic view of band splitting in Si induced by strain technology.

quantum mechanics, wave function is confined in the potential and energy quantization is observed. Such quantized eigen energies are called quantized subbands. As confinement mass is higher in 2-fold valleys and lower in 4-fold valleys, if MOS structure is implemented, subband spritting [6,7] occurs as shown in Fig. 1.5 (b).

A. Introduction of strain technology and high-k materials

To enhance the device performance, lower transport mass is an important factor, because it is thought to directly contributes to high drain current density. Therefore, ways to utilize the lower transport mass of 2-fold valleys have been sought. A major way to boost the device performance is strain technology. If uniaxial tensile strain is induced to the <110> oriented silicon channel, band splitting in 2-fold and 4-fold valleys is induced and the band energy gap becomes large, as shown in Fig. 1.5 (c). At the same time, transport effective mass for 2-fold valleys becomes even smaller. As a result, the strain technology makes it possible to increase channel mobility and to achieve low-voltage operation. Since 2004, strained-Si technology was implemented to 90nm-node MOSFET [8] to pull up the mobility.

Not only that, mainly for the suppression of gate leakage current [9], materials with high dielectric (high-k) materials were also introduced to the gate insulator in 2007, which enabled the introduction of thicker gate insulator while maintaining gate capacitance.

B. New device structures

In addition to introduction of strain technology and high-k materials, to further pursue the scaling trend by improving device performance, the use of new device structures is proposed. Fig. 1.6 shows device structures of nanoscale MOSFETs. In ultra-scaled bulk MOSFETs, electrons are distributed into the depth direction (z direction in Fig. 1.6 (a)), and gate controllability is drastically degraded. Therefore, to solve the problem, SOI structure is proposed, in which electrons are confined between two oxides, and gate controllability is improved. Moreover, DG MOSFET introduces back gate. With this structure, quantitatively speaking, gate control is doubled compared to SOI MOSFET. Also, SOI and DG MOSFETs with an intrinsic channel are considered to have advantages of high immunity to the V_{th} roll-off and of achieving high ballistic transport efficiency, both of which are because of the absence of impurities in the channel region [4].

On the other hand, in reality, in spite of earlier proposal, planar DG structure is technologically difficult to implement, because an efficient way to fabricate back gate hasn't been found until now, as far as the author knows. As a result, not DG structure, but FinFET structure is introduced for mass production. Since FinFET is a 3D structure and has three Si/SiO_2 interfaces, it seems that FinFET and DG MOSFET have quite different gate controllability. However, their features are quite similar unless Fin height is smaller than about 10 nm. Therefore, if Fin height is enough larger than Fin thickness, 2D DG MOSFET can be assumed to be a good approximation for FinFET. Most recently, in 2011, 22 nm node microprocessors with 3D tri-gate FinFETs were announced by Intel. Thanks to such technological development, the downscaling has been successful until today.

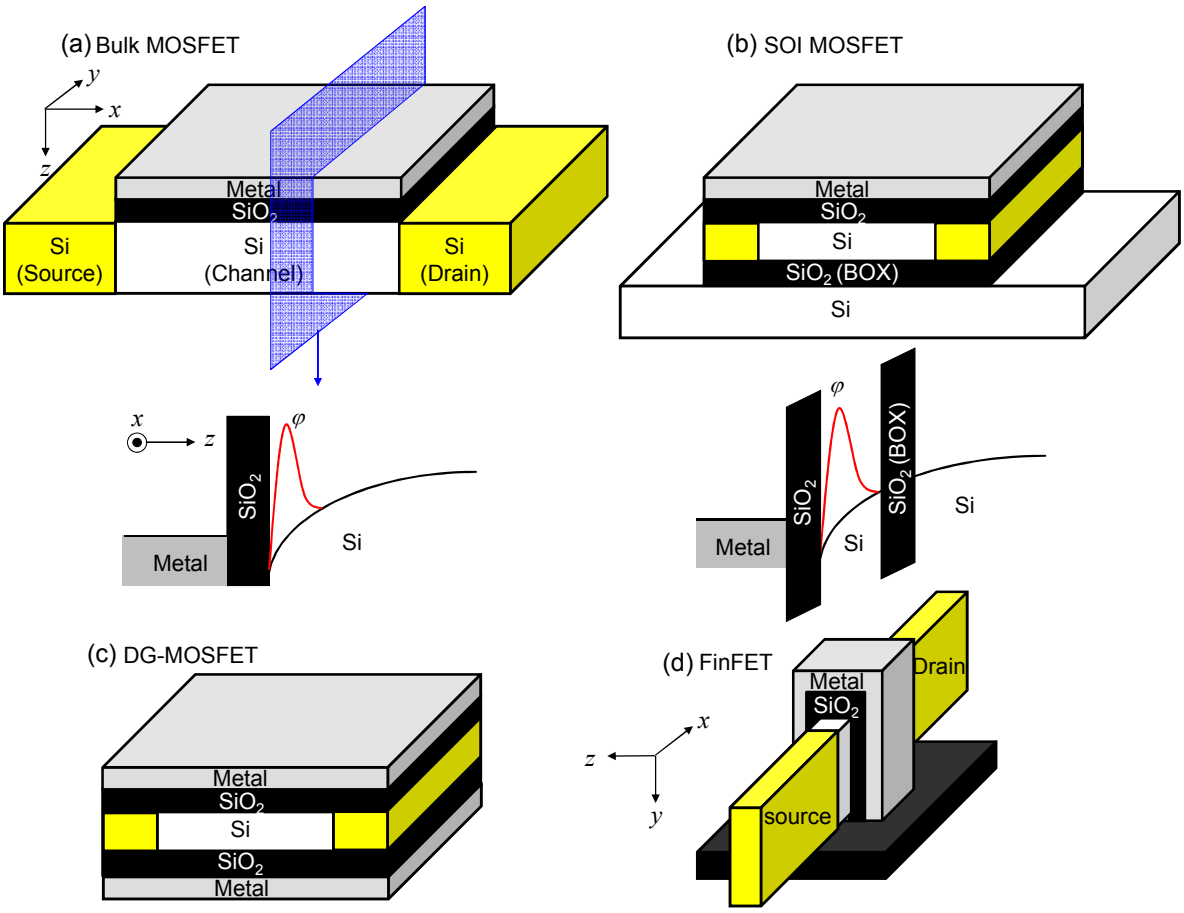

Fig. 1.6 Device structures for nanoscale MOSFETs. (a) Conventional bulk MOSFET, (b) SOI MOSFET, (c) DG MOSFET, and (d) FinFET. Cross-sectional view of potential energy and electron wave function profiles along the confinement direction is also depicted for (a) and (b).

TABLE 1.3: Effective mass and mobility of electrons and holes for representative channel materials, where m_0 is the free electron mass and m_t and m_l is transverse and longitudinal effective masses. m_{HH} and m_{LH} stand for heavy hole and light hole effective masses [1,10].

		Si	Ge	InP	$In_{0.53}Ga_{0.47}As$
Electrons	Effective mass (m_0)	0.19/0.92 (m_t/m_l)	0.082/1.467 (m_t/m_l)	0.082	0.046
	Mobility ($cm^2/V \cdot s$)	1300–1500	3900	5400	20000
Holes	Effective mass m_{HH}/m_{LH} (m_0)	0.49/0.16	0.28/0.044	0.45/0.12	0.51/0.22
	Mobility ($cm^2/V \cdot s$)	430	1900	200	450

1.2.2 Quest for new channel materials

Furthermore, new channel materials such as Ge and III–V compound semiconductors have been proposed and extensively studied to replace Si. In particular, because of their higher electron mobility and significantly lower electron effective mass as shown in Table 1.3, III–V materials are expected for n-channel MOSFETs. Among III–V materials, it is worth noting that the high performance of MOSFETs with InGaAs [11–15] and InP [16] channels has already been experimentally demonstrated.

On the other hand, for III–V materials, many issues to be settled are piled up. For example, in III–V MOSFETs, electrons are distributed deeply into the substrate because of their small effective masses, and therefore, confinement structures such as SOI, DG, or Fin structures are strongly required to achieve good gate controllability, whereas quest for the suitable insulator materials is still under way. Also, scattering by polar optical phonon is intrinsic to the III–V materials. Not only that, their use in MOSFETs may lead to more serious quantum transport effects along the channel direction such as quantum reflection and tunneling, because of their smaller effective masses and enhanced ballistic transport compared to Si. Therefore, performance predictions of III–V materials must consider scattering by polar optical phonons and quantum transport effects. Scattering rate formulation of polar optical phonons is described in chapter 5.

1.3 Conventional device simulation methods

In spite of technology boosters mentioned above, as the gate length of the MOSFETs has reduced down to 10 nm scale, quantum transport effects along the channel direction such as source–drain (SD) direct tunneling, quantum reflection inside the channel region and quantum repulsion in the source and drain regions have become more and more important. On the other hand, for such ultra-scaled devices, it is a common view that ballistic transport is enhanced because of decreased scattering number in the channel. However, it is known that AP scattering rate becomes higher in SOI and multi-gate MOSFETs than that in bulk Si MOSFETs, and not only that, a new type of surface roughness scattering caused by spatial fluctuation of quantized subbands emerges in extremely scaled SOI channels. Therefore, a device simulation with precise treatment of both scattering and quantum transport is indispensable for performance projection of future nano-scale MOSFETs and understanding of physical mechanisms inside them.

A. Drift diffusion model

When device size was larger enough for quantum effects to be hidden, classical simulation methods such as drift diffusion model and semi-classical Monte Carlo (MC) simulation were widely used. The popular drift-diffusion model is derived from the Boltzmann transport equation (BTE) by considering moments of the BTE. The model is usually based on the set of current equation, continuity equation, and Poisson's equation. This model was widely used because of its significant simplicity, but the model has difficulty in treating scattering precisely.

B. Semi-classical MC method

Semi-classical MC method is a particle-based approach and also based on BTE like drift diffusion model. MC method's advantage is a simple and rigorous treatment of scattering. MC particles represent real carriers, so MC particles can be directly scattered according to the scattering rate. Thus, MC method can easily and rigorously include scattering effects. Scattering rate is obtained according to the Fermi's golden rule, which is quantum mechanical approach. Hence, scattering is treated quantum mechanically. This is why the method is called *semi*-classical MC method. Since MC method has been shown to have the ability to quantitatively reproduce experimental results, the method has been also one of the most widely used simulation methods.

However, now device size is already too small for drift diffusion model. Semi-classical Monte Carlo method also can't be applied in the depth direction, because quantum confinement effect is already significant. Thus, various quantum device simulation approaches which can treat quantum mechanical effects have been proposed. Here, some major simulation approaches are introduced.

C. Non-equilibrium Green's function method (*NEGF*)

One of the most commonly used quantum simulation approaches is non-equilibrium Green's function method (NEGF) [17], which can rigorously describe quantum effects and scattering effects. Theory of the method dates back to 1950s and 60s. NEGF has an advantage when combined with atomistic simulation such as *ab-initio* calculation and tight binding method. *Ab-initio* or tight binding Hamiltonian can accurately describe the band structure compared to effective mass approximation, so this advantage is very appealing. Therefore, the method is widely used in the performance prediction of nanoscale devices. However, incorporating inelastic scattering mechanisms or describing detailed physical phenomena occurring inside the device is not as easy as MC method in general.

D. Quantum-corrected MC method

Another commonly used simulator is a quantum-corrected (QC) MC simulator [18], which can easily incorporate multiple scattering mechanisms, and has the ability to illustrate microscopic phenomena, such as a position-dependent analysis of scattering events. QCMC simulator appeared in late 1990s to early 2000s. The most important achievement of QCMC is its success in describing quantum effect with MC method. As shown in the following chapter, MC simulator is based on particle approach, and thus we can directly monitor the particles in the device. Therefore, the method makes it easier to understand physical phenomena inside the device. However, since this method uses approximation for describing quantum effects, higher-order energy quantization or quantum interference effect such as quantum reflection can't be simulated by the method.

E. Multi-subband MC method

Since electrons in the MOSFETs are strongly confined to have 2D nature, which is called 2D electron gases (2DEGs), a simulation technique to solve 2DEG problems precisely should be introduced [19]. One of the ways to extend the ability of MC methods is multi-subband (MS) MC method. For the devices with a uniform width or a uniform cross-sectional structure, quantum effects can be safely separated into those along the confinement

direction and those along the transport direction, and a mode space expansion method (MSEM) can be applied [20]. Therefore, for devices with long channel length (i.e., L_{ch} > 8 nm for Si) or for mobility calculation, classical (Boltzmann-transport-equation-based) MC (BMC) method can well reproduce device characteristics. However, since MSBMC method doesn't have the ability to simulate quantum effects along the transport direction, the method isn't reliable for devices with channel length for which quantum transport effects become significant.

1.4 Objectives of this work

Therefore, in this research, bearing such background in mind, I aimed at developing a MSMC simulator which can fully incorporate major scattering mechanisms for 2DEGs and a 'Wigner Monte Carlo (WMC)' simulator, which solves Wigner transport equation (WTE) using MC method and rigorously incorporates quantum transport effects. The Wigner Monte Carlo method was proposed with a concept of 'affinity' by Shifren et al [21] and extended to the simulators of MOSFETs by Querlioz et al [22], and the method was shown to have the ability to simulate quantum transport effect in MOSFETs rigorously [23]. By combining WMC method and MSMC method, i.e., MSWMC method, devices in which both quantum confinement effects and quantum transport effects take place can be accurately simulated.

Such simulators are useful with the view of not only precise performance prediction and selection of device structures and materials but also resolution of unexplained physical phenomena in the integrated nanoscale MOSFETs. Such application results of the simulator will also be shown in the remained part of the thesis.

1.5 Overview of this thesis

Chapter 2 and chapter 3 focus on the precise treatment of scattering mechanisms in nanoscale MOSFETs.

Chapter 2 focuses on the establishment of rigorous scattering treatment. A MSBMC simulator applicable for nanoscale MOSFETs are introduced and scattering rates for major scattering mechanisms derived for 2DEG are also introduced with the treatment in increased AP scattering and surface roughness scattering due to quantized subband energy fluctuation, while quantum transport effect along the channel direction is ignored to focus on the impact of scattering mechanisms. The validity of proposed scattering mechanism modeling is demonstrated by comparisons with the experimental results and our simulation results for electron mobility in bulk MOSFET and SOI MOSFETs.

In chapter 3, the MSBMC simulator developed in chapter 2 is extended to the DG MOSFETs with a significant improvement in the treatment of source and drain electrode that enables us to estimate subthreshold characteristics, which is regarded next to impossible using MC simulator. A new method to directly calculate the quasi-ballistic transport parameters for ultrasmall DG MOSFETs is proposed, and the results have demonstrated that the ballistic transport in DG MOSFETs is enhanced due to L_{ch} scaling until L_{ch} = 10 nm, but when L_{ch} is further scaled to less than 10 nm, SR scattering intensified by spatial fluctuation of quantized subbands drastically degrades ballistic transport. The results indicate that performance improvement is difficult even if MOSFETs are scaled less than 10 nm, which is very important viewpoint for

the discussion of the miniaturization limits. A technological development needed to receive the benefits of ballistic transport in the sub-10 nm regime is also discussed.

Chapter 4 and chapter 5 focuses on quantum transport effect in nanoscale MOSFETs.

In chapter 4, a MSWMC quantum transport simulator for Si DG MOSFET, which can fully incorporate quantum transport effects, is developed and its ability is shown. By using the MSWMC simulator, it is demonstrated that the quantum reflection makes significant differences in the microscopic features of electron transport and can even reduce the drain current at on-state, but it does not necessarily produce drastic change in the macroscopic properties including the drain current. On the other hand, the SD tunneling plays a crucial role in the subthreshold properties of scaled MOSFETs with channel lengths of less than 6 nm. It is also demonstrated that the WMC approach has the ability to describe quantum-classical transition of carrier transport in the diffusive transport regime dominated by scattering.

In chapter 5, our MSWMC simulator is applied to MOSFETs with III–V channel materials to show that it can be applicable to the new materials. III-V compound semiconductors are expected to replace Si as the channel material in n-channel MOSFETs. Treatments of conduction band structure in III-V MOSFETs and polar optical phonon scattering, which is intrinsic to the compound semiconductor materials, are described in the anterior half of the chapter.

In the last half of the chapter, the impact of source-to-drain direction quantum transport effect on the III–V MOSFETs was investigated, with simulations of $In_{0.53}Ga_{0.47}As$ and InP MOSFETs, which have the most developed process technology. As a result, it was found that subthreshold current increase due to SD direct tunneling becomes more remarkable both in $In_{0.53}Ga_{0.47}As$ and InP MOSFETs owing to its significantly lower effective mass compared to Si. In addition, the critical channel length for which a drastic increase in subthreshold current occurs due to SD direct tunneling was found to be about 20 nm for both $In_{0.53}Ga_{0.47}As$ and InP MOSFETs. Since this value is significantly larger than that for Si MOSFETs, SD direct tunneling can be a major obstacle to downscale III-V MOSFETs into $L_{ch} < 20$ nm.

It is suggested that the choice of a material with a heavier transport mass might be one option to go beyond the end of the roadmap.

In chapter 6, summarization of the achievements in this thesis is provided, and discussions on the direction of future nanoscale integrated device research and the role of the simulation study in the development of the devices are made.

References

[1] Y. Taur, and T. Nin, *Fundamentals of Modern VLSI Devices*, Cambridge University Press, 1998.

[2] S. Takagi, A. Toriumi, M. Iwase, H. Tango, IEEE Trans. Electron Devices **41**, 2357 (1994).

[3] R. H. Dennard, F. H. Gaensslen, V. L. Rideout, E. Bassous, and A. R. LeBlnac, IEEE J. Solid-State Circuits **9**, 256 (1974).

[4] K. Natori, J. Appl. Phys. **76**, 4879 (1994).

[5] K. Uchida, H. Watanabe, A. Kinoshita, J. Koga, T. Numata, and S. Takagi, IEDM Tech. Dig., 2002, p. 47.

[6] S. Takagi, J. Koga, and A. Toriumi, Jpn. J. Appl. Phys. **37**, 1289 (1998).

[7] S. Takagi, J. Koga, and A. Toriumi, IEDM Tech. Dig., 1997, p. 219.

[8] S. Takagi, N. Sugiyama, T. Mizuno, T. Tezuka, and A. Kurobe, Mat. Sci. and Eng. B **89**, 426 (2002).

[9] C. M. Osburn, I. Kim, S. K. Han, I. De, K. F. Yee, S. Gannavaram, S. J. Lee, C.-H. Lee, Z. J. Luo, W. Zhu, J. R. Hauser, D.-L. Kwong, G. Lucovsky, T. P. Ma, and M. C. Öztürk, IBM J. Res. and Dev. **46**, 299 (2002).

[10] S. Takagi, J. Electronics, Information, and Communication Engineers **92**, 43 (2009) (in Japanese).

[11] M. Radosavljevic, B. Chu-Kung, S. Corcoran, G. Dewey, M. K. Hudait, J. M. Fastenau, J. Kavalieros, W. K. Liu, D. Lubyshev, M. Metz, K. Millard, N. Mukherjee, W. Rachmady, U. Shah, and R. Chau, IEDM Tech. Dig., 2009, p. 319.

[12] J. A. del Alamo, Nature **479**, 317 (2011).

[13] Y. Yonai, T. Kanazawa, S. Ikeda, and Y. Miyamoto, IEDM Tech. Dig., 2011, p. 307.

[14] X. Zhou, Q. Li, C. W. Tang, and K. M. Lau, Appl. Phys. Express **5**, 104201 (2012).

[15] S. H. Kim, M. Yokoyama, N. Taoka, R. Iida, S. Lee, R. Nakane, Y. Urabe, N. Miyata, T. Yasuda, H. Yamada, N. Fukuhara, M. Hata, M. Takenaka, and S. Takagi, Appl. Phys. Express, **5** 014201 (2012).

[16] S. H. Kim, M. Yokoyama, N. Taoka, R. Iida, S. Lee, R. Nakane, Y. Urabe, N. Miyata, T. Yasuda, H. Yamada, N. Fukuhara, M. Hata, M. Takenaka, and S. Takagi, Appl. Phys. Lett. **98**, 243501 (2011).

[17] L. V. Keldysh, Sov. Phys. JETP **20**, 1018 (1965).

[18] H. Tsuchiya and U. Ravaioli, J. Appl. Phys. **89**, 4023 (2001).

[19] M. V. Fischetti and S. E. Laux, Phys. Rev. B **48**, 2244 (1993).

[20] J. S.-Martin, A. Bournel, F. Monsef, C. Chassat, and P. Dollfus, Semicond. Sci. Technol. **21**, L29 (2006).

[21] L. Shifren, C. Ringhofer, and D. K. Ferry, IEEE. Trans. on Electron Devices **50**, 769 (2003).

[22] D. Querlioz, P. Dollfus, V.-N. Do, A. Bournel, and V. L. Nguyen, J. Comput. Electron. **5**, 443, (2006).

[23] D. Querlioz, J. Saint-Martin, V.-N. Do, A. Bournel, and P. Dollfus, IEEE Trans. on Nanotechnol. **5**, 737, (2006).

[24] H. Tsuchiya, K. Fujii, T. Mori, and T. Miyoshi, IEEE Trans. on Electron Devices **53**, 2965 (2006).

2. Development of Monte Carlo simulator applicable for nanoscale MOSFETs

Scattering is one of the most important factors to determine the device performance of MOSFETs. Therefore, a simulator with reliable scattering treatments is indispensable for the performance and physics projection of the MOSFETs. Therefore, in this chapter, reliable scattering treatments for 2D electron gases (2DEGs) are proposed and their validity is demonstrated with the electron mobility calculation of bulk Si MOS and SOI MOS structures. To focus on the modeling of scattering mechanisms, quantum effect along the transport direction is ignored in chapter 2 and 3. The validity of the scattering modeling is demonstrated by comparisons with experimental results of mobility in bulk and SOI MOSFETs.

2.1 Monte Carlo method coupled with Schrödinger equation

In this thesis, we consider bulk MOSFET, SOI MOSFET, and DG MOSFET. In all cases, triangular potential well or quantum well is formed within the channel and electrons are strongly confined to behave as 2DEG, resulting in subband splitting [1,2]. To describe electron transport of 2DEG in the inversion-layers, we employed the MSBMC approach, in which Schrödinger equation and Poisson's equation are self-consistently solved and potential profile, quantized subband, wave functions, and scattering rates are obtained before MC simulation. Then, MC simulation is conducted using the results by the Schrödinger-Poisson (SP) solver. Scattering processes considered in this paper are AP, optical phonons (OP), ionized impurity, and SR scatterings, all of whose scattering rates are formulated for 2DEG as described below.

MC method is one of the most widely used approaches to solve Boltzmann transport equation numerically [3]. Boltzmann transpoort equation is given as

$$\frac{\partial f}{\partial t} + \mathbf{v} \cdot \nabla_{\mathbf{r}} f - \frac{1}{\hbar} \nabla_{\mathbf{r}} U \cdot \nabla_{\mathbf{k}} f = Cf \,, \tag{2.1}$$

where f is a distribution function, $\mathbf{r}$ the position vector (x, y, z), $\hbar$ the Dirac constant, U stands for potential energy, and C collision operator, i.e., Cf stands for collision term. Scattering rates are obtained with Fermi's golden rule, which means that scattering is treated by the perturbation theory in quantum mehcanics. That is, drift-diffusion movement of electron is expressed classically, whereas scattering is treated quantum-mechanically. This is why MC solution of BTE is called 'semi-'classical MC method, which we refer as BMC method. Derivation of scattering rates is described in the following section.

In an effective mass approximation, parabolic band structure is assumed. According to BTE, equations-of motion for electrons during a free flight are expressed as follows.

$$\frac{d\mathbf{r}}{dt} = \mathbf{v} = \frac{\hbar \mathbf{k}}{m^*}, \tag{2.2}$$

$$\frac{d\mathbf{k}}{dt} = -\frac{1}{\hbar}\nabla_{\mathbf{r}} U = -\frac{q\mathbf{E}}{\hbar}. \tag{2.3}$$

However, as electrons' kinetic energy becomes higher, discrepancy between parabolic band approximation and real band structure becomes larger. Therefore, nonparabolicity is usually introduced to improve the accuracy of effective mass approximation as

$$E_{\mathbf{k}}(1 + \alpha E_{\mathbf{k}}) = \frac{\hbar^2 k^2}{2m^*}, \tag{2.4}$$

where α is the nonparabolicity coefficient of the $E - \mathbf{k}$ relationship. In that case Eq. (2.2) is modified with nonparabolicity coefficient as

$$\frac{d\mathbf{r}}{dt} = \mathbf{v} = \frac{\hbar \mathbf{k}}{m^*(1 + 4\alpha E_{\mathbf{k}})}. \tag{2.5}$$

After the free flight, electrons are scattered according to collision term *Cf*, changing wave vector, kinetic energy, valley, and subband.

For the simulation of MOS structures with uniform electric field along the transport direction, and therefore for the mobility calculation, movement of electrons in real space need not be simulated in MSWMC method, because carrier distribution along *x* and *y* direction depicted in Fig. 2.1 (a) can be assumed uniform, and carrier distribution along confinement direction is already obtained using SP solver, as is depicted in Fig. 2.1 (b).

A flow chart of BMC simulation for MOS structures is described in Fig. 2.2. Note that in realistic simulation of MOS structure, electron distribution, electric field, and potential profile can be assumed to be uniform in *x* and *y* direction, as is discussed above. Therefore, calculation of electron position *x*, *y* and also drift of a wave number vertical to the transport direction (k_y) is unnecessary. Also, in *z* direction, not BMC method but Schrödinger equation is solved to obtain the quantum mechanical electron profile and subband profile. Accordingly, position *z* and wave number k_z are also unnecessary for MC equations-of-motion.

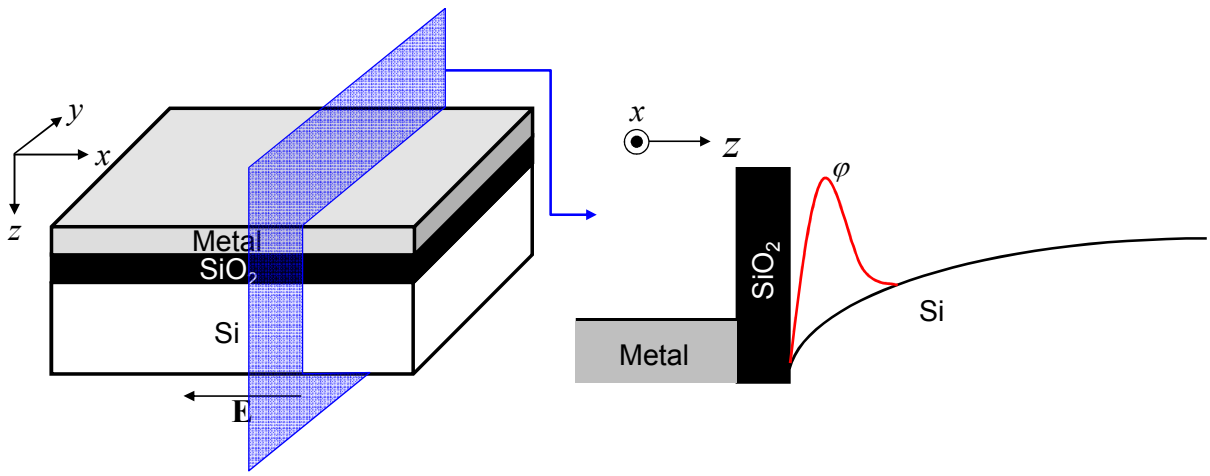

Fig. 2.1 (a) Schematic view of a MOS structure, and (b) its cross-sectional view of potential energy and electron wave function profiles along the confinement direction.

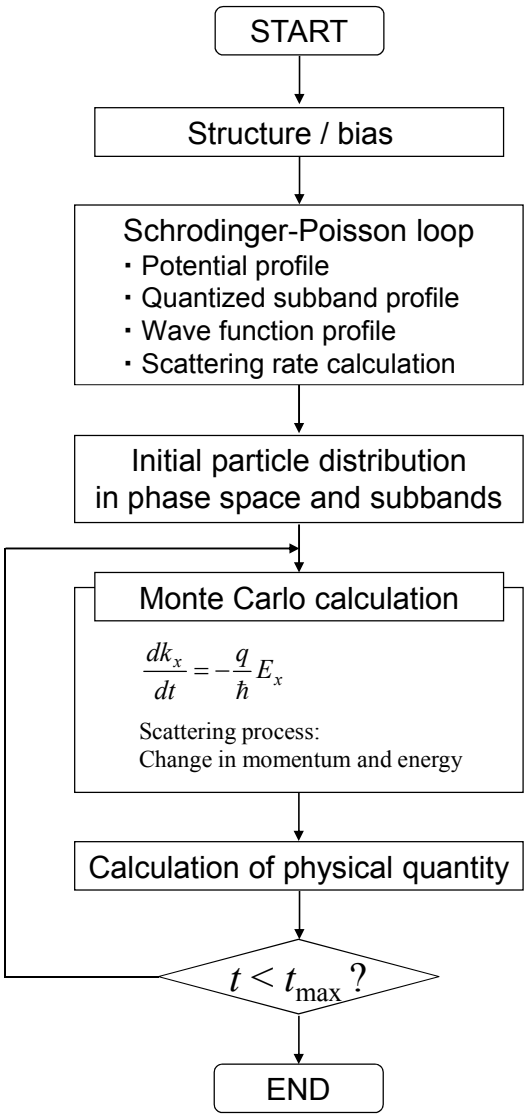

Fig. 2.2 A flowchart of Monte Carlo simulation conducted in mobility calculation.

For simulation of MOSFETs with non-uniform potential distribution along the transport direction, i.e., MOSFETs with source and drain, position x must be calculated. Simulation method in such a case will be discussed in chapter 3. Initial distribution of carriers is determined according to the result of SP solver, which solves Schrödinger equation

$$\left[-\frac{\hbar^2}{2m^*} \frac{d^2}{dz^2} + U(z) \right] \psi_n(z) = E_n \psi_n(z) \tag{2.6}$$

and Poission's equation

$$\frac{d}{dz}\left(\varepsilon_r \frac{d\varphi(z)}{dz} \right) = -\frac{e}{\varepsilon_0} [N_D(z) - n(z) + p(z)] \tag{2.7}$$

self-consistently, where $\psi_n(z)$ and E_n is a wave function and eigen energy (or quantized subband energy) for n-th subband, $\varphi(z)$ the potential distribution along the confinement direction, and Potential energy distribution for electrons is obtained using $\varphi(z)$ as

$$U(z) = E_C(z) - q\varphi(z), \tag{2.8}$$

where $E_C(z)$ is the (relative) energy of the bottom of the conduction band. Schematic view of the eq. (2.8) is shown in Fig. 2.3. During the SP loop, electron distribution for each valley and subbands is calculated according to the results of eq. (2.6) and (2.7) , and the obtained electron distribution $n(z)$ is re-assigned to SP calculation. These process are repeated until conversion criterion is satisfied. This process is called self-consistent calculation. Then, scattering rate is calculated with converged $\psi_n(z)$, E_n and $\varphi(z)$, and these information is used in the subsequent MC calculation.

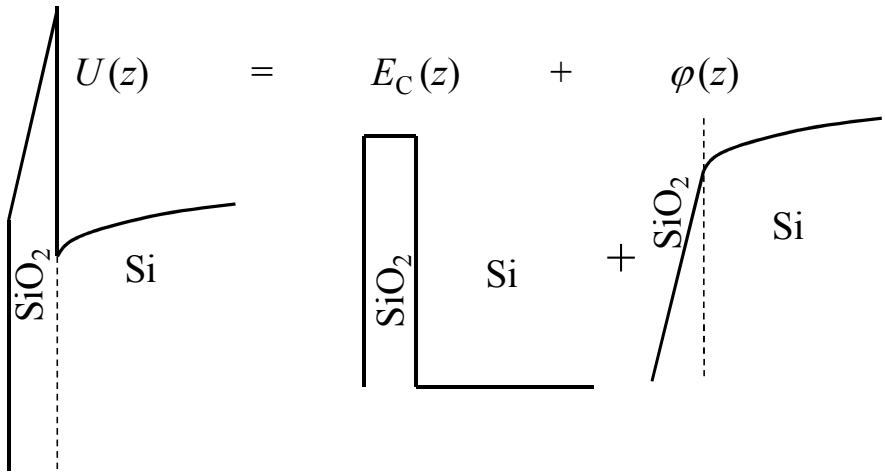

Fig. 2.3 Schematic view of eq. (2.8). Potential energy $U(z)$ is described as asum of $E_C(z)$ and $\varphi(z)$.

After self-consistent result of SP solver is obtained, MC loops are executed, in which particles are drifted and scattered according to the electric field along the transport direction and calculated scattering rate. Mobility is estimated by averaging each electron's velocity. Electron's movement in real space x, y, z and wave number k_z isn't simulated. Wave number k_x and k_y, kinetic energy E_x and E_y determined by E–k dispersion, and E_z determined by quantized subband energy, is simulated in the MC calculation.

2.1.1 Free flight and scattering process

A. Determination of the free-flight time

Carriers are scattered after a free flight of time τ. Determination of free flight time τ is a very complex procedure.

First, a total scattering rate for a energy is obtained as a sum of scattering rates for each scattering mechanism as

$$W_T(E_k(t)) = \sum_{j=1}^{N} W_j(E_k(t)) \tag{2.9}$$

where j is an index of scattering processes, W_j is a scattering rate of a process j.

$$P_f(t+dt) = P_f(t)\{1 - W_T(E_k(t))dt\}, \tag{2.10}$$

where $P_f(t)$ is the probability for an electron *not* to be scattered before time t. Therefore, a Talor expansion of 1st order yields

$$P_f(t) + \frac{dP_f(t)}{dt}dt \approx P_f(t) - P_f(t)W_T(E_k(t))dt \ , \tag{2.11}$$

subtracting $P_f(t)$,

$$\frac{dP_f(t)}{dt}dt \approx -P_f(t)W_T(E_k(t))dt \tag{2.12}$$

is obtained. This is a differencial equation with an answer of

$$P_f(t) = C\exp\left\{-\int_0^t W_T(E_k(t))\ dt'\right\}, \tag{2.13}$$

where C is the integral constant. An electron's free flight can be assumed to start at $t = 0$, therefore C is assumed 1. As a result,

$$P_f(t) = \exp\left\{-\int_0^t W_T(E_k(t))\ dt'\right\} \tag{2.14}$$

is obtained. Finally, probability for an electron to be scattered after a free flight of time τ is expressed as

$$P(\tau) = W_T(E_k(t))\exp\left\{-\int_0^\tau W_T(E_k(t))\ dt'\right\}. \tag{2.15}$$

The direct use of this scattering probability is unrealistic because electron kinetic energy is time-dependent and scattering rate is dependent on electrons' energy. Therefore, to make determination of free flight time τ possible, the difference between maximum scattering rate and the scattering rate at a certain energy is defined as "scattering rate of no scattering event $W_0(E_k(t))$". Such scattering rate is called 'virtual scattering'. In that case, total scattering rate $W_0(E_k(t)) + W_T(E_k(t))$ is constant for any kinetic energy. The value is expressed as

$$W_0(E_k(t)) + W_T(E_k(t)) = \sum_{j=0}^{N} W_j(E_k(t)) = W_{T,\max} \equiv \Gamma \ . \tag{2.16}$$

In that case, $P(\tau)$ can be analytically integrated as

$$P(\tau) = \Gamma\exp\left(-\int_0^\tau \Gamma\, dt\right) = \Gamma e^{-\Gamma\tau} \ . \tag{2.17}$$

Therefore, interval of scattering events τ is expressed as

$$\tau = -\frac{\ln(P(\tau)/\Gamma)}{\Gamma} = -\frac{\ln(r_1)}{\Gamma}, \tag{2.18}$$

where r_1 is a random number valued between 0 to 1.

B. Treatment of scaterring process

After the selection of scattering mechanism, final valley and subband are determined according to normalized table, and then final energy $E_f(k)$ and wave number $\mathbf{k}_{\|}$ is determined according to the energy conservation law and random number. $E_f(k)$ is determined as follows:

$$E_f(k) = E_i(k) \pm \hbar\omega + (E_m^{\nu} - E_n^{\nu'}) \tag{2.19}$$

where ν and ν' are indices of initial and final valley, m and n are indices of initial and final subband, and $\hbar\omega$ is an energy obtained or lost by the scattering event.

C. Determination of final wave vector $\mathbf{k}'$

Scattering rate is obtained by the isotropic band approximation with a 2D density-of-state mass m_d^*. Thus, determination of final wave vector requires Herring-Vogt transformation. First, wave number k_x and k_y are transformed according to the following equation.

$$\begin{bmatrix} k_x^* \\ k_y^* \end{bmatrix} = U \begin{bmatrix} k_x \\ k_y \end{bmatrix}, \tag{2.20}$$

where U is given as

$$U = \begin{bmatrix} \sqrt{m_d^* / m_y^*} & 0 \\ 0 & \sqrt{m_d^* / m_z^*} \end{bmatrix}. \tag{2.21}$$

Herring-Vogt transformation transforms wave vector on an equi-energy ellipse into one on an equi-energy circle. Relation between final kinetic energy and final wave vector is expressed using transformed wave vector $\mathbf{k}^*$ as

$$E_k(1 + \alpha E_k) = \frac{\hbar^2}{2}\left(\frac{k_y^2}{m_y^*} + \frac{k_z^2}{m_z^*}\right) = \frac{\hbar^2 k^{*2}}{2m_d^*}. \tag{2.22}$$

If a scattering mechanism is elastic, final wave vector is determined on the equi-energy circle using rotation matrix as

$$\begin{bmatrix} k_x'^* \\ k_y'^* \end{bmatrix} = \begin{bmatrix} \cos\theta & \mp\sin\theta \\ \pm\sin\theta & \cos\theta \end{bmatrix} \begin{bmatrix} k_x^* \\ k_y^* \end{bmatrix}, \tag{2.23}$$

where a sign of rotation angle is determined randomly regardless of scattering mechanism.

If a scattering mechanism is inelastic, final wave number is obtained as

$$\begin{bmatrix} k_x'^* \\ k_y'^* \end{bmatrix} = \begin{bmatrix} \cos\theta & \mp\sin\theta \\ \pm\sin\theta & \cos\theta \end{bmatrix} \begin{bmatrix} k'^* k_y^* / k^* \\ k'^* k_z^* / k^* \end{bmatrix}. \tag{2.24}$$

Finally, inverse Herring-Vogt transform is used to obtain the final wave vector $\mathbf{k}^* = (k_y^*, k_z^*)$ on the ellipsoidal band structure from wave vector $\mathbf{k}'^* = (k_y'^*, k_z'^*)$.

$$\begin{bmatrix} k_y' \\ k_z' \end{bmatrix} = U^{-1} \begin{bmatrix} k_x'^* \\ k_y'^* \end{bmatrix}, \tag{2.25}$$

where U^{-1} is expressed as

$$U^{-1} = \begin{bmatrix} \sqrt{m_y^* / m_d^*} & 0 \\ 0 & \sqrt{m_z^* / m_d^*} \end{bmatrix}. \tag{2.26}$$

2.2 Scattering treatment of two-dimensional electron gas

Since carrier transport is strongly dependent on carrier mobility at on-state, an accurate modeling of scattering mechanisms is indispensable.

Scattering rate is derived using Fermi's golden rule

$$S(i,f) = \frac{2\pi}{\hbar} \left| \left\langle \mathbf{k}'_{\parallel}, n_{\mathbf{q}'} \middle| H' \middle| \mathbf{k}_{\parallel}, n_{\mathbf{q}} \right\rangle \right|^2 \delta(E'_{\parallel} - E_{\parallel} \mp \hbar\omega_{\mathbf{q}}), \tag{2.27}$$

where H' is the perturbation Hamiltonian and $\delta(x)$ is Dirac's delta function, indicating energy conservation law.

By integrating $S(i,f)$ with final state $\mathbf{k}'$, scattering rate is obtained as

$$W(E) = \frac{\Omega}{(2\pi)^3} \int_{-\infty}^{\infty} S(i,f) d\mathbf{k}'. \tag{2.28}$$

In the MC simulation, not only scattering rate but also scattering angle θ, which is defined as an angle between initial and final wave vector $\mathbf{k}$ and $\mathbf{k}'$, has significant influence. Schematic view of scattering angle is shown in Fig. 2.4.

Specifically, if a scattering process is anisotropic forward one, the influence of scattering can be less significant than isotropic scattering. On the other hand, if a scattering process is backward one, it can substantially affect device performance. Therefore, anisotropy of scattering effect should be investigated in detail.

As for determination of final state wave vector, for isotropic scattering such as non-polar phonon scattering, scattering angle is determined using random number as

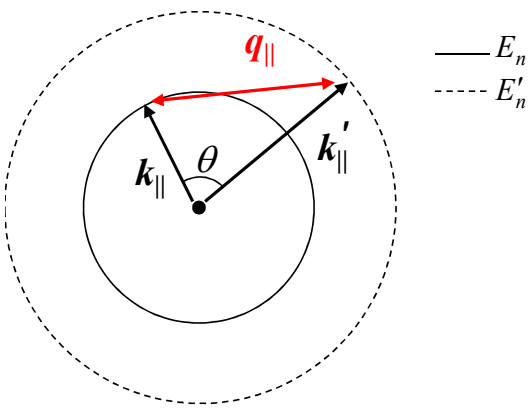

Fig. 2.4 Schematic view of scattering angle.

$$r = \frac{1 - \cos\theta}{2}, \tag{2.29}$$

therefore, scattering angle is analytically obtained as

$$\cos\theta = 1 - 2r \,. \tag{2.30}$$

On the other hand, for anisotropic scattering, $W(\theta)$ is defined as the scattering rate for angle within θ, and scattering probability within an angle θ is tabulated by calculating

$$\frac{W(\theta)}{W(E)} \,. \tag{2.31}$$

After tabulation, scattering angle is determined using random number r, that is, if random number r is valued between $W(\theta)/W(E)$ and $W(\theta+\Delta\theta)/W(E)$, scattering angle is determined as θ.

Hereafter, specific scattering rates and scattering angles for major scattering processes are described. If a scattering angle can be analytically obtained, the equation is shown, and if not, $W(\theta)/W(E)$ is shown.

2.2.1 Elastic acoustic phonon scattering

Movement of an electron in the periodic crystal lattice isn't disturbed by the regularly-arrayed atoms, but is disturbed by the displacement of atoms around their equilibrium position, i.e. lattice vibration. It is usually assumed that the displacements of atoms around their equilibrium position are small and the interaction between them can be described by harmonic potentials. In the quantum approach, quantized lattice vibration is called phonon, and scattering by phonons is called phonon scattering. Phonon scattering is characterized by its strong temperature dependency. However, for the room temperature, electron-phonon interaction is one of the dominant scattering processes for describing carrier transport in the semiconductor.

We can identify the AP and OP branches. AP branches represent vibration which adjacent atoms move in the same direction, and it causes local dilation or contraction of the crystal as shown in Fig. 2.5, which results in the change of band gap, affecting electron's movement. On the other hand, optical phonons (OPs) represent vibration which adjacent atoms move in the opposite direction, and OP doesn't involve local dilation or contraction of the crystal, but movement of the atoms in the opposite direction directly affects the electrons' momenta.

In terms of scattering rate, it is rather important whether a scattering is intra-valley or inter-valley, or whether scattering process is elastic or inelastic, than whether the scattering is AP or OP.

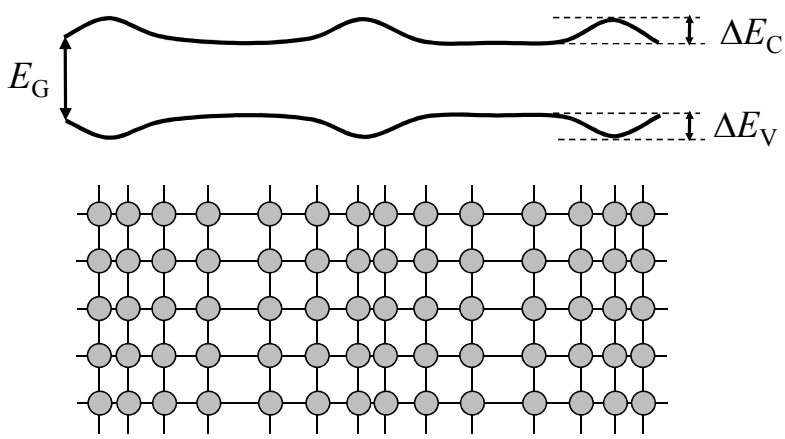

Fig. 2.5 Schematic view of a deformation of the crystal.

In silicon, intra-valley OP scattering is prohibited. Therefore, intra-valley AP scattering and inter-valley phonon scatterings are considered.

Intra-valley AP scattering involves phonons with wave number $q \sim 0$ and phonon energy with $\hbar\omega_{\mathbf{q}} \sim 0$. Hence, Intra-valley AP phonon scattering can be treated as elastic scattering, though, strictly speaking, it is non-elastic.

When the confinement direction is set as z, elastic intra-valley AP scattering rate we used is expressed as

$$\Gamma_{\mathrm{ac}} = \frac{D_{\mathrm{ac}}^2 k_{\mathrm{B}} T \sqrt{m_x m_y}}{2\hbar^3 \rho v^2}(1+2\alpha E')\int \varphi_m^2(z)\varphi_n^2(z)\, dz\,, \tag{2.32}$$

where D_{ac} is the deformation potential of AP, whose treatment will be discussed later. ρ is the crystal density, v the sound velocity, k_{B} the Boltzmann constant, T the temperature and assumed to be 300 K in the present work. m_x and m_y are the effective masses in the x and y axes, with $m_l = 0.98\ m_0$ and $m_t = 0.19\ m_0$. α is a nonparabolicity parameter and set as 0.5 eV^{-1}. E' is a kinetic energy of final state, and $\varphi_m(z)$ and $\varphi_n(z)$ are the electron wave function of initial and final states along the confinement direction, respectively.

Note that between v and ρ, the following equation holds:

$$v = \sqrt{c_{\mathbf{L}} / \rho}\,, \tag{2.33}$$

where c_{L} is the lattice constant of the crystal. Elastic AP scattering is treated as isotropic process, so scattering angle is determined by eq. (2.10).

2.2.2 Inelastic phonon scattering

Both acoustic and optical inelastic inter-valley phonon scattering rates are expressed as

$$\Gamma_{\mathrm{inelastic}} = \frac{N_v D_{\mathrm{op}}^2 \sqrt{m_x m_y}}{2\hbar^2 \omega_{\mathrm{op}} \rho}(1+2\alpha E')\left[N_q + \frac{1}{2} + \sigma\right]\int \varphi_m^2(z)\varphi_n^2(z)\, dz\,, \tag{2.34}$$

where N_v is the number of possible final valleys, D_{op} the deformation field, $\hbar\omega_{\mathrm{op}}$ the phonon energy, N_q the average number of phonons at a temperature. σ is given as 1/2 for phonon emission and $-1/2$ for phonon absorption. For inelastic inter-valley phonon scatterings, we adopted the widely-used parameter set proposed in ref. 3.

Inelastic phonon scattering is also treated as isotropic process, and scattering angle is determined by eq. (2.29).

2.2.3 Ionized impurity scattering

The expression we employed for ionized impurity scattering rate is the following one, which was reported to well express experimental mobility over a wide range of electron density [4,5], and is given as

$$\Gamma_{\mathrm{imp}} = \frac{e^4 \sqrt{m_x m_y}(1+2\alpha E')}{8\pi\hbar^3 \varepsilon^2}\int_0^{2\pi} d\theta \left\{ \int_0^{T_{\mathrm{Si}}} dz_0\, N_{\mathrm{imp}}(z_0) \left| \int_0^{T_{\mathrm{Si}}} dz \frac{\varphi_m(z) e^{-\Delta k(\theta)|z-z_0|}\varphi_n(z)}{\Delta k(\theta) + Q_{\mathrm{scr}}(\Delta k)} \right|^2 \right\}, \tag{2.35}$$

where θ is the scattering angle between the initial and final wave vector $\mathbf{k}$ and $\mathbf{k}'$, $\Delta k = |\mathbf{k} - \mathbf{k}'|$, ε the dielectric permittivity of Si and assumed to be 11.9 ε_0, $N_{\mathrm{imp}}(z_0)$ the impurity density (donor or acceptor concentration) at position z_0, and Q_{scr} the temperature-dependent screening function given as [5,6]

$$Q_{\mathrm{scr}}(\Delta k) = \frac{e^2 n_{\mathrm{scr}}}{2\varepsilon k_B T} g_1\left(\frac{\Delta k \lambda_{\mathrm{th}}}{4\sqrt{\pi}}\right) \times \int_0^{T_{\mathrm{Si}}} \int_0^{T_{\mathrm{Si}}} dz' dz\ \varphi_1^2(z)\varphi_1^2(z') e^{-\Delta k|z-z'|} \quad , \tag{2.36}$$

where n_{scr} is sheet electron density of the lowest subband, which contributes to the screening, λ_{th} stands for thermal wave length and the function $g_1(x)$ is defined as

$$g_1(x) = \frac{1}{x} e^{-x} \int_0^x e^{t^2} dt \quad , \tag{2.37}$$

which is derived from real part of plasma dispersion function [6].

Ionized impurity scattering has strong anisotropy and its anisotropy has kinetic energy dependency as shown in Fig. 2.6.

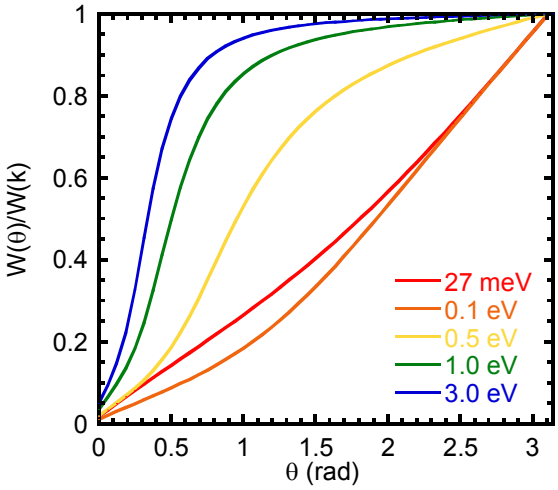

Fig. 2.6 Kinetic energy dependency of scattering angle for ionized impurity scattering, where both doping concentration and electron density are set as 1.0×10^{26} m^{-3}.

2.2.4 Surface roughness scattering

Oxide/semiconductor interface such as Si/SiO_2 interface is not perfectly flat, as shown in Fig. 2.7. Therefore, electrons are scattered with non-flat interface, which is called SR scattering. Moreover, with a quantum mechanics, fluctuation in the body thickness caused by SR results in the discrepancy in the energy level is also a cause of scattering. As a result, we must include both classical SR scattering caused by the diffuse reflection of carriers and

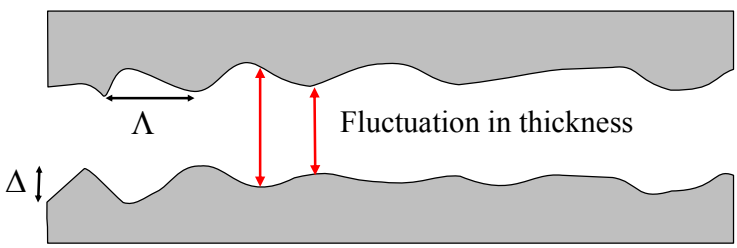

Fig. 2.7 Schematic view of SR and its characteristic parameters. Fluctuation in thickness causes the fluctuation of quantized subband energy.

SR caused by the fluctuation of quantized subbands.

In this dissertation, so-called Prange-Nee term [7] is introduced for SR scattering. Although this approach is simple and further advanced approaches are presented [8–10], we considered the approach accurate enough to express SR scattering in SOI devices, since it can include both scatterings due to the diffusive reflection at the Si/SiO_2 interfaces and spatial fluctuation of quantized subbands. Throughout this paper, we used an exponential spectrum with root-mean-square Δ = 0.5 nm and correlation length Λ = 1.0 nm for the roughness spectrum. Here, it should be noted that root-mean-square Δ and correlation length Λ are statistically and experimentally obtained ones, or simply used as fitting parameters. Therefore, although Δ and Λ are indicated in Fig. 2.7, strictly speaking, the true Δ and Λ are statistically averaged value of those indicated in the figure.

Expression of SR scattering rate is given as

$$\Gamma_{\mathrm{sr}} = \frac{(1+2\alpha E')\sqrt{m_x m_y}}{\pi\hbar^3} \times \int_0^{2\pi} d\beta \frac{\pi\Delta_m^2\Lambda^2}{(1+|\Delta k|^2\Lambda^2/2)^{3/2}} \left| \frac{\hbar^2}{2m_z} \frac{d\varphi_n(0)}{dz} \frac{d\varphi_m(0)}{dz} \right|^2 , \tag{2.38}$$

where $(\hbar^2/2m_z)(d\varphi_n(0)/dz)(d\varphi_m(0)/dz)$ is the Prange-Nee term [7]. If SOI or DG structure is considered, SR scattering at back interface must be also included. In that case, Prange-Nee term for back interface i.e., $(\hbar^2/2m_z)(d\varphi_n(T_{\mathrm{Si}})/dz)(d\varphi_m(T_{\mathrm{Si}})/dz)$, is added to eq. (2.38). As shown in Fig. 2.8, SR scattering is also anisotropic scattering process.

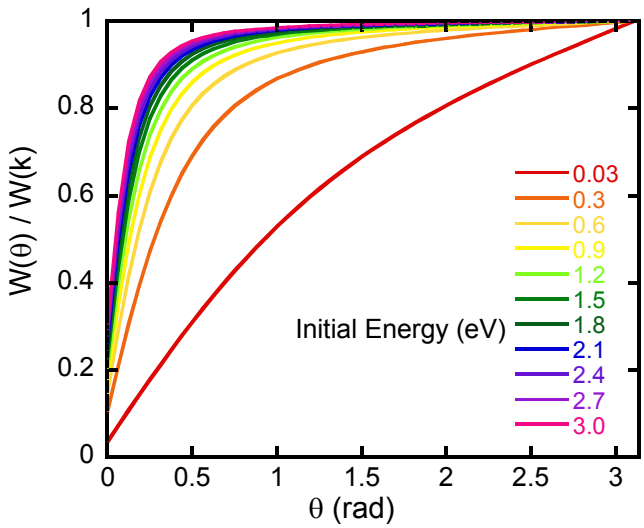

Fig. 2.8 Energy dependency of scattering angle for roughness scattering, where T_{Si} = 3nm is employed.

2.3 Spatially variable deformation potential in acoustic phonon scattering

D_{ac} is an important parameter to characterize AP scattering. However, D_{ac} has fundamentally anisotropic nature and in addition, D_{ac} for 2DEG exhibits kinetic energy dependency, and strictly speaking, is influenced by screening effect [11-13]. Therefore, an exact treatment of D_{ac} for 2DEG becomes very complicated, and in many

cases D_{ac} is assumed to be isotropic and independent of energy for simplicity [3,14,15]. The *constant* value of D_{ac} which agrees with experimental bulk Si mobility is known to be 9.0–9.5 eV [3,14,15], but these values cannot replicate universal curve for bulk MOS inversion-layer mobility for the aforementioned reasons, and thus D_{ac} = 12–13 eV [15,16] is widely used in MOS simulations (cD_{ac} model). However, in SOI MOSFETs, the use of D_{ac} = 12–13 eV results in overestimation of electron mobility, suggesting that effective isotropic D_{ac} is even higher than 13 eV in SOI channels and may exhibit a SOI thickness (T_{Si}) dependency.

In this study, we employed a spatially *variable* D_{ac} model (vD_{ac} model), which has been proposed by Ohashi et al [17,18], in order to consider T_{Si}-dependent D_{ac}. vD_{ac} model treats D_{ac} as spatially variable, that is, D_{ac} sharply increases at MOS interfaces as shown in Fig. 2.9, which has been demonstrated to well reproduce experimental mobility in SOI MOSFETs [17]. Note that we must include effects both from front and back interfaces for SOI and DG structures, and hence averaged D_{ac} inside Si channel increases as compared with that in bulk MOS structure.

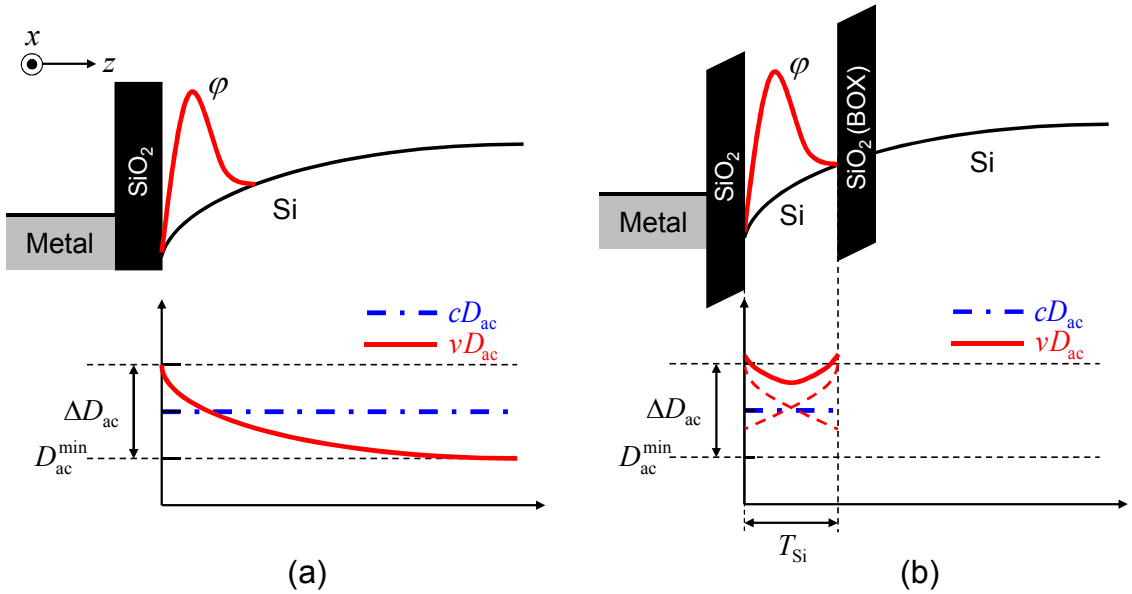

Fig. 2.9 Constant D_{ac} (cD_{ac}) and variable D_{ac} (vD_{ac}) models for (a) bulk MOS and (b) SOI MOS structures. Drastic increase of D_{ac} near the interfaces is depicted. We used expressions for D_{ac} (z) proposed in refs. 19 and 20. Note that we must include effects both from front and back interfaces for SOI and DG structures, and hence averaged D_{ac} inside Si channel increases as compared with that in bulk MOS structure.

For bulk MOS structure depicted in Fig. 2.9 (a), following expression has been proposed [17,18].

$$D_{ac}(z) = \Delta D_{ac} \exp(-z / L_{ac}) + D_{ac}^{min} . \tag{2.39}$$

D_{ac}^{min} represents bulk deformation potential (9.0 eV) and ΔD_{ac} is defined as 7.0 eV. $L_{ac} = 2.5$ nm is a damping factor and z is a position measured from the Si/SiO_2 interface along the confinement direction. When SOI or DG structure is simulated, as depicted in Fig. 2.9 (b), D_{ac} is calculated using the following equation.

$$D_{ac}(z) = \Delta D_{ac} \exp(-z / L_{ac}) + \Delta D_{ac} \exp\{(z - T_{Si}) / L_{ac}\} + D_{ac}^{min} . \tag{2.40}$$

We have implemented both cD_{ac} and vD_{ac} models in the calculation of AP scattering rate, and then calculated electron mobilities for bulk Si MOSFET and SOI MOSFET.

2.4 Comparison between simulated and experimental electron mobilities for MOSFETs

To confirm the validity of our MC simulator, we have calculated electron mobility of bulk Si MOS and SOI MOS structures, and made a comparison with experimental results. Table 2.1 shows the parameters used in the calculation of scattering rates.

It should be noted that scattering processes considered in this section are AP, OP and SR scattering, while ionized impurity scattering is not considered because effect of impurity scattering is insignificant unless effective normal electric field (E_{eff}) is sufficiently low. A (001) surface is assumed and transport direction is set as <110>. Accordingly, conduction band structure is split into 2-fold valleys with a higher electron mobility and 4-fold valleys with a lower one. Unless mentioned, temperature is assumed 300K for all following results in this thesis.

TABLE 2.1: Scattering parameters for Si used in the simulation.

effective mass m^* (m_0)		0.19 (m_t) / 0.92 (m_l)	
nonparabolicity α (eV^{-1})		0.5	
cristal density ρ (kg/m^3)		2329.0	
sound velocity v_s (m/s)		9040.0	
phonon types		deformation potential	phonon energy (meV)
elastic acoustic phonon		9.5 eV(bulk crystal) 13.0 eV (MOS inversion layers)	—
inelastic phonons	*f*-TA	3×10^7 eV/cm	19.0
	f-LA	2×10^8 eV/cm	47.4
	f-TO	2×10^8 eV/cm	59.0
	g-TA	5×10^7 eV/cm	12.0
	g-LA	8×10^7 eV/cm	18.5
	g-LO	1.1×10^9 eV/cm	61.2

2.4.1 Bulk Si MOSFET

First, Fig. 2.10 shows the calculated electron mobility in bulk MOS inversion-layer versus E_{eff}. Results obtained by using cD_{ac} (9.0 eV), cD_{ac} (13 eV), vD_{ac} are plotted as triangles, reversed triangles and circles, respectively. Experimental curve[19] for substrate acceptor concentration $N_A = 2 \times 10^{16}$ cm^{-3} is also plotted as solid line. As pointed out in ref. 19, mobility in medium E_{eff} region is mainly determined by AP scattering, and

thus the approach using cD_{ac} (9.0 eV) obviously overestimates electron mobility except for high E_{eff} region. On the other hand, it can be confirmed that both vD_{ac} and cD_{ac} with 13 eV well reproduce experimental electron mobility of bulk Si MOSFET.

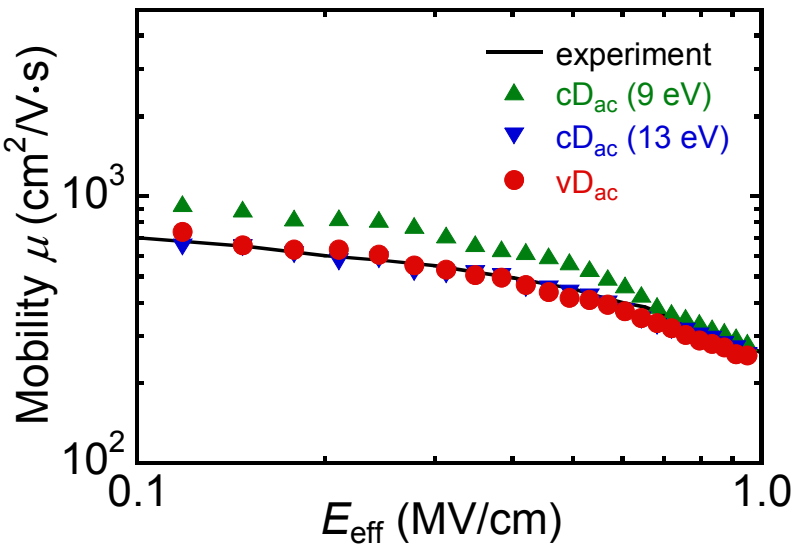

Fig. 2.10 Electron mobility in bulk MOS inversion-layer versus effective normal field E_{eff}. Results obtained by using cD_{ac} (9.0 eV), cD_{ac} (13 eV), vD_{ac} are plotted as triangles, reversed triangles and circles, respectively. Experimental curve [19] for substrate acceptor concentration $N_A = 2 \times 10^{16}$ cm^{-3} is also plotted as solid line.

2.4.2 Ultrathin SOI MOSFET

Next, Fig. 2.11 shows T_{Si} dependency of SOI electron mobility computed for a medium electric field of E_{eff} = 0.3 MV/cm. Circles, squares, and triangles represent the experimental [20], vD_{ac}, and cD_{ac} (13 eV) results, respectively. In Fig. 2.11, a mobility enhancement around T_{Si} = 3 ~ 4 nm is observed in both cD_{ac} (13 eV) and vD_{ac} models, which is explained by modulation in electron occupancy of each conduction band valley, i.e., when T_{Si} < 4 nm, most of electrons occupies the 2-fold valleys with a higher electron mobility due to the formation of a sufficiently lower quantized energy subband in the 2-fold valleys [1,2]. However, vD_{ac} model indicates a slighter mobility enhancement, and it also indicates a decrease in mobility from T_{Si} = 8 to 6 nm, both of which are similar tendencies as those of the experiment. The above results mean that cD_{ac} (13 eV) model overestimates the SOI electron mobility, because the increase in D_{ac} coming from the back interface cannot be incorporated in cD_{ac} model. Consequently, vD_{ac} model is more accurate than cD_{ac} model compared to experimental mobilities, especially for ultrathin body SOI MOSFETs with T_{Si} < 8 nm. Here, the discrepancy in SOI thickness exhibiting the mobility peak may be due to the assumption taken in the simulation, i.e. infinitely high potential barrier at the Si/SiO_2 interfaces for solving Schrödinger equations. The assumption should increase eigen energies of confined electrons, leading to an increased energy gap between split subbands. In the next chapter, quasi-ballistic transport in ultrasmall DG MOSFETs is discussed based on the MC technique with the scattering models explained in this section.

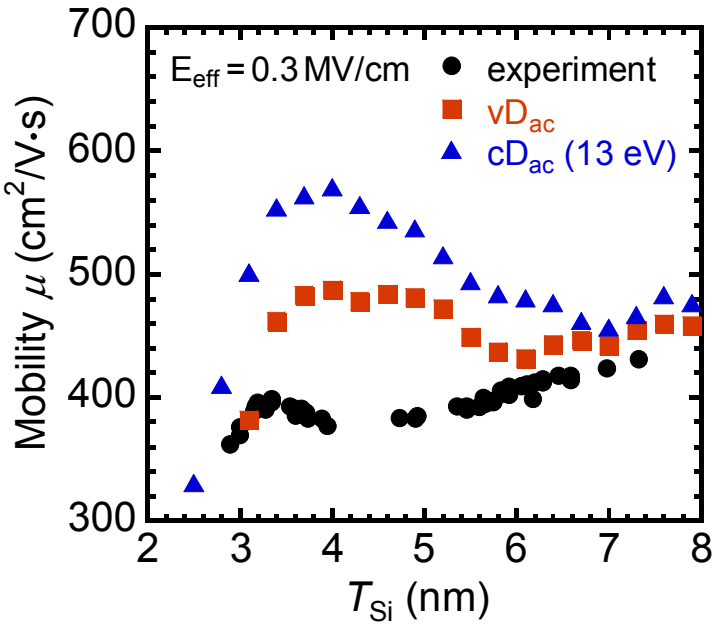

Fig. 2.11 T_{Si} dependency of SOI electron mobility computed for a medium electric field of E_{eff} = 0.3 MV/cm. Circles, squares, and triangles represent the experimental [20], vD_{ac}, and cD_{ac} (13 eV) results, respectively.

2.5 Summary

In this chapter, a multi-subband MC method for 2DEGs used in this thesis is described and scattering rates for 2DEGs are formulated. The treatment in increased AP scattering and SR scattering due to quantized subband energy fluctuation is also discussed.

The validity of the scattering rates is demonstrated with comparisons of simulated mobilities with experimental ones of a bulk MOSFET and SOI MOSFETs. As a result, experimental mobility for bulk MOSFET is accurately reproduced and it is shown that T_{Si} dependency of mobility is more accurately described with *vD*ac approach. In chapter 3, the effect of T_{Si} dependent D_{ac} increase and SR scattering due to quantized subband energy fluctuation on the ballistic transport in the ultra-scaled devices will be investigated.

References

[1] S. Takagi, J. Koga, and A. Toriumi, Jpn. J. Appl. Phys. **37**, 1289 (1998).

[2] S. Takagi, J. Koga, and A. Toriumi, IEDM Tech. Dig. 1997, p. 219.

[3] C. Jacoboni and L. Reggiani, Rev. Mod. Phys. **55**, 645 (1983).

[4] D. Querlioz and P. Dollfus, *The Wigner Monte Carlo method for nanoelectronic devices* (Wiley, New York, 2010) Chap. 3, p. 89.

[5] F. Monsef, P. Dollfus, and S. G.-Retailleau, J. Appl. Phys. **95**, 3587 (2004).

[6] A. L. Fetter, Phys. Rev. B **10**, 3739 (1974).

[7] R. E. Prange and T.-W. Nee, Phys. Rev. **168**, 779 (1968).

[8] D. Esseni, IEEE Trans. Electron Devices **51**, 394 (2004).

[9] S. Jin, M. V. Fischetti, and T.-W. Tang, IEEE Trans. on Electron Devices **54**, 2191 (2007).

[10] P. Toniutti, D. Esseni, and P. Palestri, IEEE Trans. on Electron Devices **57**, 3074 (2010).

[11] M. V. Fischetti and S. E. Laux, Phys. Rev. B **48**, 2244 (1993).

[12] M. V. Fischetti and S. E. Laux, J. Appl. Phys. **80**, 2234 (1996).

[13] M. V. Fischetti, J. Appl. Phys. **89**, 1232 (2001).

[14] K. Hess, *Advanced theory of semiconductor devices* (Wiley-IEEE Press, New York, 2000) Chap. 7, p. 89.

[15] S. Takagi, J. L. Hoyt, J. J. Welser, and J. F. Gibbons, J. Appl. Phys. **80**, 1567 (1996).

[16] D. Esseni, P. Palestri, and L. Selmi, “Carrier scattering in silicon MOS transistors,” in *Nanoscale MOS transistors*, Cambridge University Press, New York, 2011, pp. 112–206.

[17] T. Ohashi, T. Takahashi, N. Beppu, S. Oda, and K. Uchida, IEDM Tech. Dig. 2011, p. 390.

[18] T. Ohashi, T. Takahashi, T. Kodera, S. Oda, and K. Uchida, extended abstracts of SSDM 2012, 2012, p. 807.

[19] S. Takagi, A. Toriumi, M. Iwase, H. Tango, IEEE Trans. Electron Devices **41**, 2357 (1994).

[20] K. Uchida, J. Koga, and S, Takagi, J. Appl. Phys. **102**, 074510 (2007).

3. Quasi-ballistic transport analysis of nanoscale Si MOSFETs

It is a common view that ballistic transport is enhanced due to channel length scaling because of decreased scattering number. On the other hand, as demonstrated in chapter 2, acoustic phonon scattering rate becomes higher in SOI MOSFETs than that in bulk Si MOSFETs, and not only that, a new type of surface roughness scattering caused by spatial fluctuation of quantized subbands emerges in extremely scaled SOI channels. Thus, in this chapter the influences of these scattering mechanisms on ballistic transport in ultrathin body Si MOSFETs are examined based on Monte Carlo simulation technique.

3.1 Quasi-ballistic MOSFETs

3.1.1 A picture of quasi-ballistic transport of carriers

As described in chapter 1, in ultimately scaled devices, the number of scattering events during the transport decreases and carrier transport enters the quasi-ballistic regime. According to ref. 1, drain current in the quasi-ballistic transport regime is expressed using an injection velocity v_{inj} and a backscattering coefficient R, instead of conventional mobility and saturation velocity. On the other hand, SOI or DG MOSFETs with an intrinsic channel are considered to have an advantage to achieve ballistic transport, because impurity scattering is absent in the channel region [2]. However, such ultrathin channel devices suffer from an increased AP scattering and a new type of SR scattering caused by spatial fluctuation of quantized subbands [3]. Since realistic and atomistic treatment of scattering processes is required, an accurate calculation of parameters such as v_{inj} and R is generally a laborious task. In this study, we addressed the extraction of quasi-ballistic transport parameters using MC simulator considering AP, OP, ionized impurity, and SR scatterings for 2DEGs in inversion-layers, where channel thickness dependent D_{ac} in AP scattering, and contribution from spatial fluctuation of quantized subbands in SR scattering described in chapter 2 were considered.

3.1.2 Backscattering coefficient and injection velocity

Figure 3.1 shows a schematic diagram of quasi-ballistic transport in a MOSFET [4]. Averaged velocity of carriers passing through the bottleneck point is defined as an injection velocity v_{inj}. When scattering exists in the channel, averaged velocity of electrons coming back from inside the channel is defined as a backward channel velocity v_{back}, and averaged total carrier velocity at the bottleneck point is written as v_{s}, which decreases from v_{inj} due to electrons bounced backward by scattering. Backscattering coefficient R is defined as a ratio of backward and forward channel currents [5], as indicated in Fig. 3.1, where Q_f and Q_b are the forward and backward charge densityes at the bottlenech, respectively, and $Q = Q_f + Q_b$ represents the total charge density at the bottleneck point.

By taking advantage of MC techniques, we carefully monitored particle trajectories crossing over the

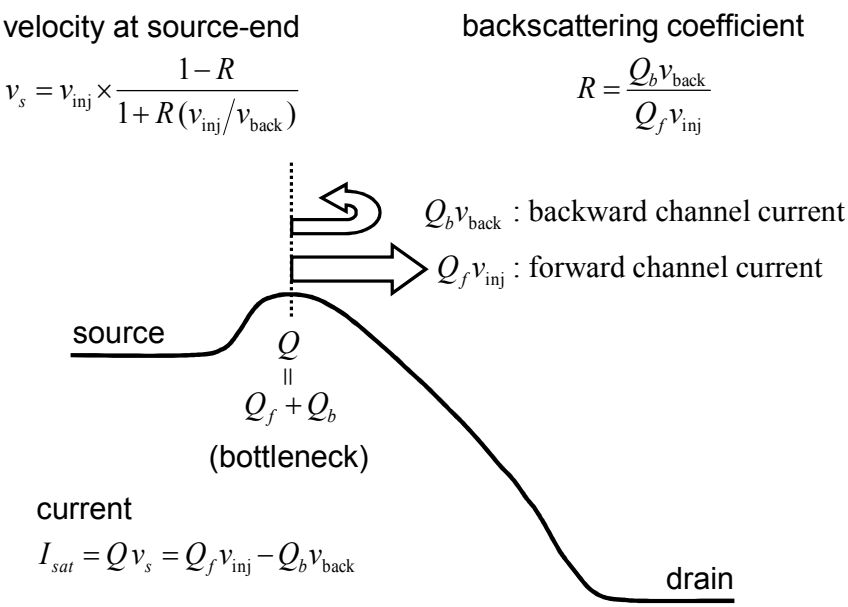

Fig. 3.1 Schematic diagram of quasi-ballistic transport and definitions of quasi-ballistic parameters in a MOSFET [4]. Backscattering coefficient R is defined as a ratio of backward and forward channel currents.

bottleneck point from source to channel and vice versa, and collected necessary information for evaluating the quasi-ballistic transport parameters. Obtained parameters are validated by comparisons with our previous approximative estimation [4] and with electron mobility calculated for ultrathin SOI MOSFETs.

3.2 Device structure

3.2.1 Double-gate Si MOSFET

Figure 3.2 shows the device structure of simulated DG MOSFET. As in the previous chapter, a (001) surface is assumed and transport direction is set as <110>. Note that the channel is undoped and thus carrier backscattering in the channel is caused by phonon and SR scatterings. Gate oxide is assumed to be SiO_2 and its thickness is given as 0.5 nm. Doping concentration of source and drain is set as $N_D = 1.0 \times 10^{20}$ cm^{-3}, and we also considered ionized impurity scattering in the source and drain regions.

As described in chapter 2, a DG MOSFET has two gate electrodes and gate control is doubled compared to SOI MOSFET. Furthermore, DG MOSFET is a good analogue of FinFET, since they have similar gate controlability if Fin height is much larger than Fin thickness.

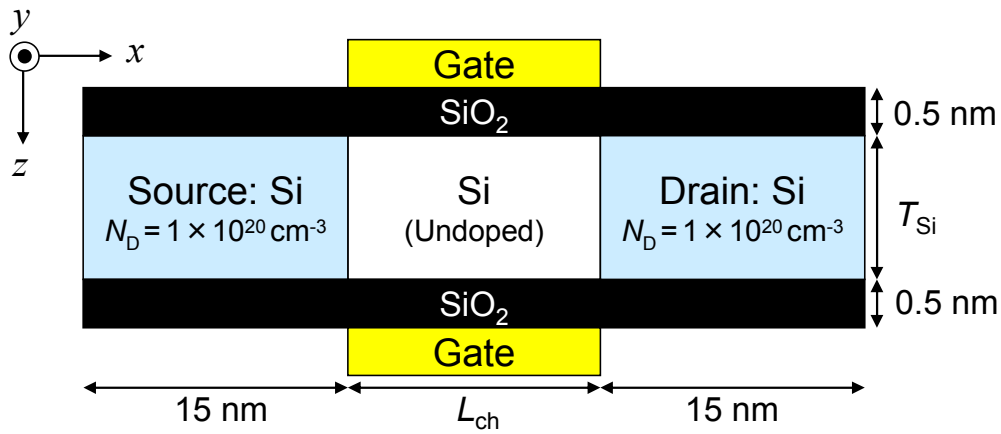

Fig. 3.2 Device structure of DG MOSFET used in the simulation. Note that channel length L_{ch} was varied from 30 to 6 nm, whereas channel thickness T_{Si} was chosen by following an empirical rule of $T_{Si} = L_{ch} / 3$, which is often used as a guideline to suppress short-channel effects. Gate oxide is assumed to be SiO_2 and its thickness is given as 0.5 nm. Doping concentration of source and drain is set as $N_D = 1.0 \times 10^{20}$ cm^{-3}. A (001) surface is assumed and transport direction is set as <110>.

3.2.2 Self-consistent multi-subband Monte Carlo (MSMC) method

In the previous chapter, electric field along the transport direction is considered uniform. In contrast, when MOSFETs with source and drain are simulated, electric field and electron distribution along the transport direction is time-dependent and not uniform. Therefore, device structure along the transport direction must be precisely given and reasonable simulation of MOSFETs requires self-consistent solution of Schrödinger-Poisson solver and MC method. This is called self-consistent MSMC method. A flowchart for the self-consistent MSMC simulation is shown in Fig. 3.3.

First, a device structure and bias voltages are given, and then profiles of initial potential, quantized subbands, and wave functions are guessed. Self-consistent MSMC simulation starts with the information. During Δt, MC particles move inside the device, changing the position and momentum according to its velocity and electric field around it. If an electron is scattered, its wave number, energy, and subbands are changed. Then charge density profile is calculated and according to the information, potential profile is renewed according to Poisson's equation. Using the potential, profiles of quantized subbands and wave functions are also renewed according to Schrödinger equation. After the calculation, electrons are injected or removed at the source and drain boundary of the simulation region to satisfy charge neutrality condition and thermal equilibrium. If necessary, physical quantities are calculated and averaged. Until simulation time satisfy a given condition, a series of calculations are repeated and time-averaged.

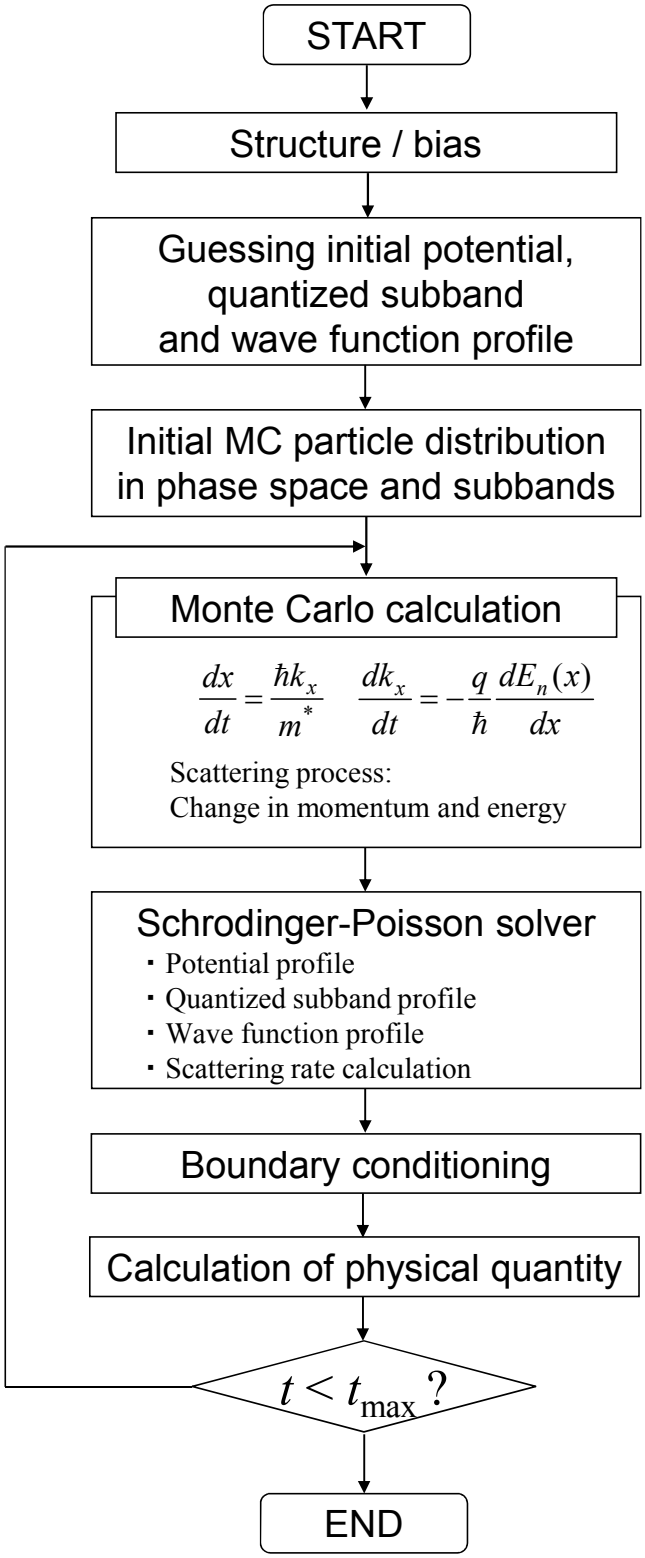

Fig. 3.3 A flowchart of self-consistent MSMC method.

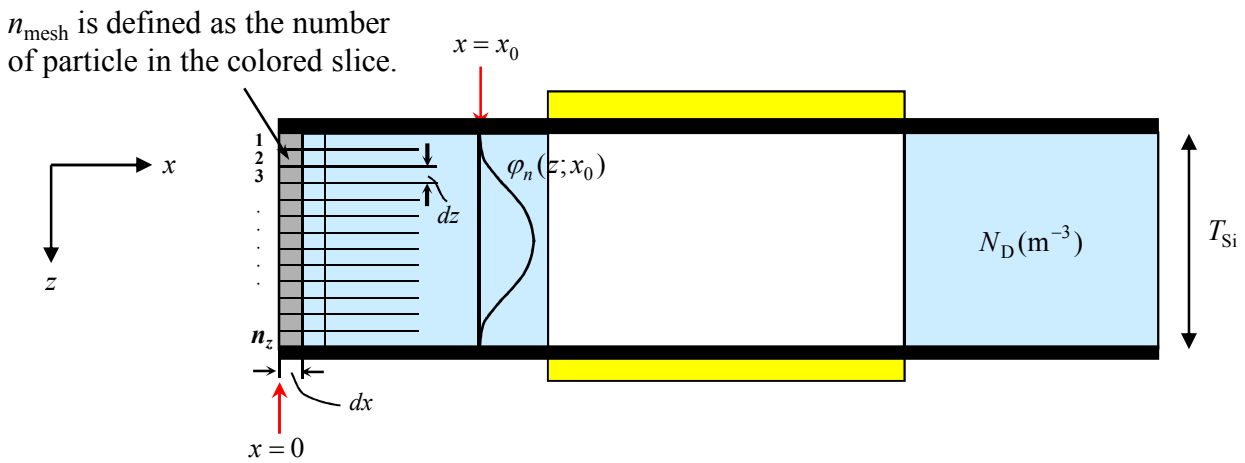

Fig. 3.4 Calculation of the amount of charge for a superparticle (e_{pp}).

Electron density distribution is obtained as follows. In MC method for MOSFETs, a concept of 'superparticle' is introduced for the calculation of sheet electron density, and number of super particles in a mesh dx in charge-neutral situation is defined as n_{mesh}. Schematic view is shown in Fig. 3.4. As a result, the amount of charge for a superparticle (e_{pp}) is obtained from the charge neutrality condition. If volume density is needed, e_{pp} is expressed as

$$e_{pp} = \frac{N_D \cdot T_{Si}}{n_{mesh}} \ (\mathrm{m}^{-2}) . \tag{3.1}$$

In a mesh $x = x_0$, charge density is obtained as the following equation.

$$n(i_z; x_0) = \sum_n N_n(z_i, x_0) \times e_{pp} \times |\psi_n(z; x_0)|^2 \ \ (\mathrm{m}^{-3}) , \tag{3.2}$$

and sheet electron density is obtained as

$$n_{2D}(x_0) = \int_0^{T_{Si}} \sum_n N_n(z_i, x_0) \times e_{pp} \times |\psi_n(z; x_0)|^2 dz \ \ (\mathrm{m}^{-2}) , \tag{3.3}$$

where n is a subband index, and $N_n(x_0)$ is a sum of the number of superparticles in a mesh $x = x_0$. Note that $\psi_n(z; x_0)$ has a dimension of $\mathrm{m}^{-1/2}$ because of the normalization.

It should be noted that electron's movement in real space x, and wave number k_x, k_y, kinetic energy E_x and E_y determined by E–k dispersion, and E_z determined by quantized subband energy, is simulated in the MC calculation for the devices with spatially non-uniform potential profile, while potential profile in y direction is considered uniform.

3.2.3 Boundary conditions

A schematic view of boundary conditions for Poisson's equation and MC approach is shown in Fig. 3.5. MC particles are removed and injected according to charge neutrality and thermal equilibrium condition at the source and drain boundary of the simulation region. As for Poisson's equation, on the gate, source and drain boundary, Dirichlet condition is applied, whereas at the other boundaries, Neumann condition is applied. As for confinement

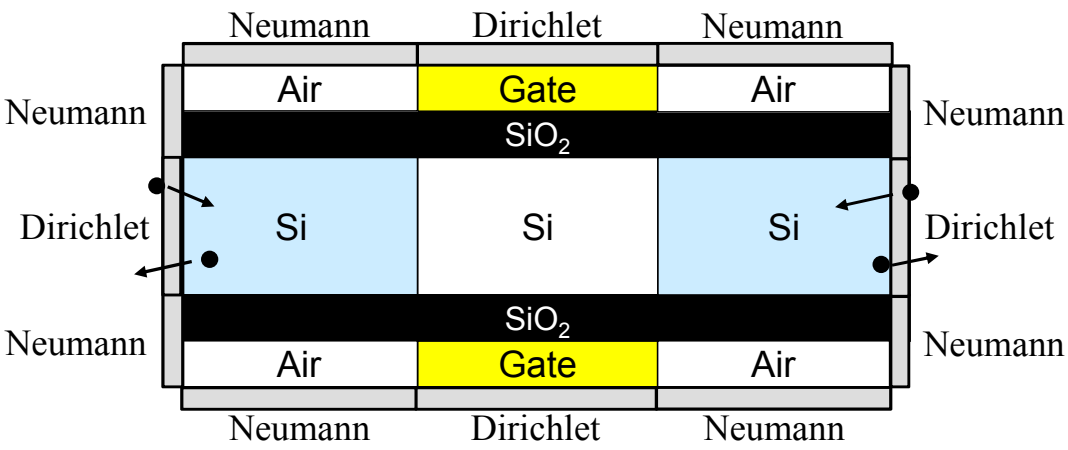

Fig. 3.5 Boundary conditions for each boundary in the device.

direction, electron distribution is calculated by Schrödinger equation, therefore specular reflection of the MC particles at the Si/SiO_2 interface, which was assigned in conventional MC method, need not be considered in MSMC method.

Note that simulation region of Schrödinger equation is limited in Silicon body and penetration of wave funciton into the oxides isn't considered in the following calculation.

3.2.4 Improved carrier injection scheme at source/drain boundaries

Particle injection and removal are conducted at the source and drain boundaries. Conventionally, electrons are randomly injected according to the Boltzmann distribution as

$$k = \frac{\sqrt{2m^* E}}{\hbar} = \frac{\sqrt{2m^*(3k_B T/2)\times \ln r_1}}{\hbar} \tag{3.4}$$

$$k_x = \begin{cases} k\sqrt{1-r_2^2} & \text{(Source)} \\ -k\sqrt{1-r_2^2} & \text{(Drain)} \end{cases} \tag{3.5}$$

$$k_y = \pm k\, r_2 \tag{3.6}$$

, where r_1 and r_2 is random numbers between 0 and 1, and sign of the k_y are determined randomly.

However, by this injection method, electrons with smaller velocities stay near the boundary meshes and charge neutrality condition isn't satisfied. As a result, in the worst case, potential distribution became higher at the boundary, which is physically incorrect.

In the present work, to make our simulator more reliable, I proposed new boundary treatment. First, if Boltzmann distribution is assumed, electron distribution function in k space is described as

$$f_w(k) \propto \exp\left(-\frac{\hbar^2 k^2}{2m^*}\right). \tag{3.7}$$

Therefore, I calculated equilibrium distribution function for each mesh in k space, and then they are summed up.

Dividing eq. (3.7) by the sum, distribution function can be normalized.

$$f_w(k) \propto \frac{\exp\left(-\frac{\hbar^2 k^2}{2m^*}\right)}{\int_{-\infty}^{\infty} \exp\left(-\frac{\hbar^2 k'^2}{2m^*}\right) dk'}. \tag{3.8}$$

Procedure for boundary conditioning is as follows. First, electrons at source end with $k_x < 0$ and ones at drain end with $k_x > 0$ are all removed regardless of the charge density at the mesh. At the same time, removed number of electrons (n_{rem}) are counted. Next, using this normalized distribution function, the number of particles for injection at each mesh is determined as

$$f_{w,inj}(k) = (n_{\mathrm{mesh}} - n_{\mathrm{rem}}) \times \frac{\exp\left(-\frac{\hbar^2 k^2}{2m^*}\right)}{\int_{-\infty}^{\infty} \exp\left(-\frac{\hbar^2 k'^2}{2m^*}\right) dk'}, \tag{3.9}$$

where n_{mesh} is the particle number that is needed to satisfy charge neutrality condition in a mesh. If $f_{w,inj}(k) < 1$, the value of $f_{w,inj}(k)$ is used as the injected electron's weighting. By conducting this boundary conditioning every loop, charge neutrality in the source and drain is perfectly achieved. When Fermi statistics is assumed, substituting eq. (3.7) with following equation, boundary condition is achieved.

$$\begin{aligned} f_w(x=0,k) &\propto \left[1 + \exp\left(E_n(x=0) + \frac{\hbar^2 k^2}{2m^*} - E_F\right) / k_B T\right]^{-1}, \text{ (Source)} \\ f_w(x=L,k) &\propto \left[1 + \exp\left(E_n(x=L) + \frac{\hbar^2 k^2}{2m^*} - E_F\right) / k_B T\right]^{-1}. \text{ (Drain)} \end{aligned} \tag{3.10}$$

This injection approach also has advantage of faster conversion of the simulation results because of the absence of randomness in the distribution. In fact, using this approach, even subthreshold slope can be calculated. This fact is surprising for MC simulation, in which errors are inherent to the simulation results.

3.3 Suppression of V_{th} lowering due to T_{Si} scaling

In this study, to suppress short-channel effects, the channel thickness T_{Si} was chosen by following an empirical rule of $T_{\mathrm{Si}} = L_{\mathrm{ch}} / 3$, with the channel length L_{ch} varied from 30 to 6 nm. In fact, we confirmed that threshold voltage (V_{th}) lowering due to L_{ch} scaling can be successfully suppressed by introducing this T_{Si} scaling as shown in Fig. 3.6, where the results obtained by using $T_{\mathrm{Si}} = L_{\mathrm{ch}} / 2$ scaling and fixed T_{Si} (= 3 nm) are also plotted for comparison. As clearly shown in this figure, the $T_{\mathrm{Si}} = L_{\mathrm{ch}} / 3$ scaling almost completely suppresses the V_{th} lowering until L_{ch} = 6 nm. In addition, the number of subbands considered in the simulation was chosen to be large enough, i.e., subbands with quantized energy less than 0.5 eV were all considered, because V_{D} = 0.5 V.

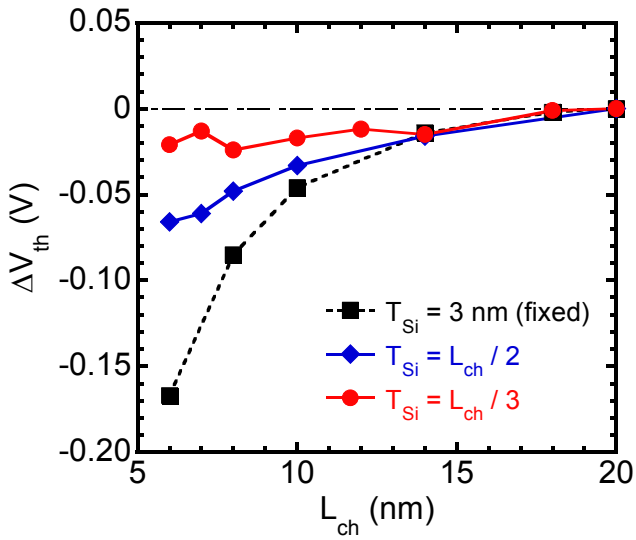

Fig. 3.6 Threshold voltage lowering ΔV_{th} computed as a function of L_{ch}, where the vertical axis represents variations in V_{th} measured from the values at L_{ch} = 20 nm, i.e., $\Delta V_{th} = V_{th}(L_{ch}) - V_{th}(20\,\text{nm})$. A black dashed line represents fixed T_{Si} (= 3 nm), a blue solid line $T_{Si} = L_{ch} / 2$, and a red solid line $T_{Si} = L_{ch} / 3$.

3.4 The influence of T_{SOI} dependent deformation potential on $I_D - V_G$ characteristics

First, $I_D - V_G$ characteristics are simulated and compared between cD_{ac} and vD_{ac} models as shown in Fig. 3.7, where (a) L_{ch} = 18 nm and T_{Si} = 6 nm, and (b) L_{ch} = 9 nm and T_{Si} = 3 nm. It is found that the drain current reduction due to vD_{ac} becomes clearer in Fig. 3.7 (b), and it can be understood by calculating spatially averaged vD_{ac} as a function of T_{Si} as shown in Fig. 3.8. Namely, due to the increased influence of D_{ac} coming from the back interface, the averaged vD_{ac} becomes larger than that of cD_{ac} (13 eV) and increases to about 17 eV for T_{Si} = 3 nm. However, the drain current reduction rate is only about 7% in Fig. 3.7 (b), which is because inelastic phonon scattering, SR scattering and impurity scattering in the source and drain also play an important role in the practical devices. Therefore, cD_{ac} model is considered to be applicable to drive current analysis of ultrasmall DG MOSFETs.

Incidentally, the dashed line in Fig. 3.8 represents an approximation formula reproducing the averaged vD_{ac} curve, which may be used as an analytical formula expressing T_{Si}-dependent D_{ac}.

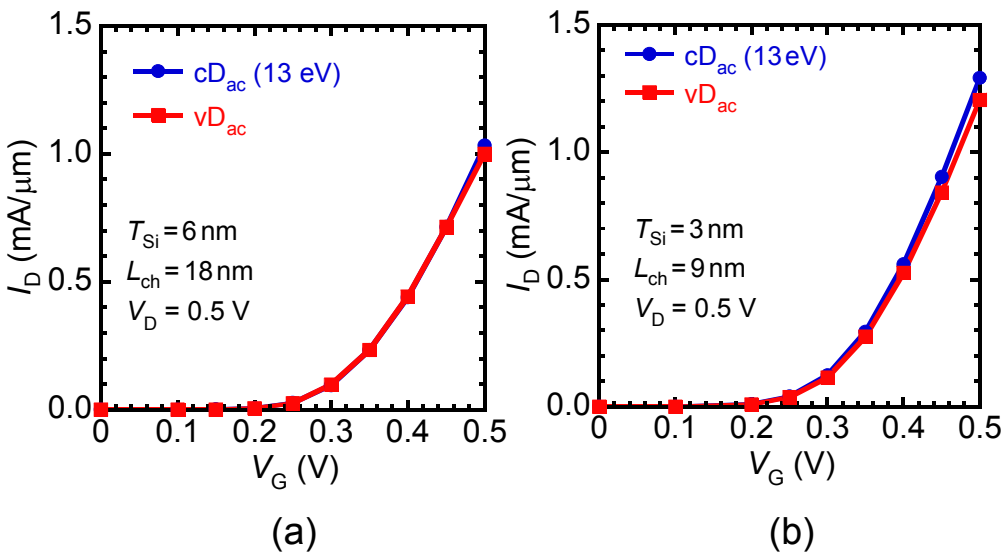

Fig. 3.7 $I_D - V_G$ characteristics computed at $V_D = 0.5$ V for DG MOSFETs with (a) $L_{ch} = 18$ nm and $T_{Si} = 6$ nm, and (b) $L_{ch} = 9$ nm and $T_{Si} = 3$ nm. The blue and red lines represent results of cD_{ac} (13 eV) and vD_{ac} models, respectively.

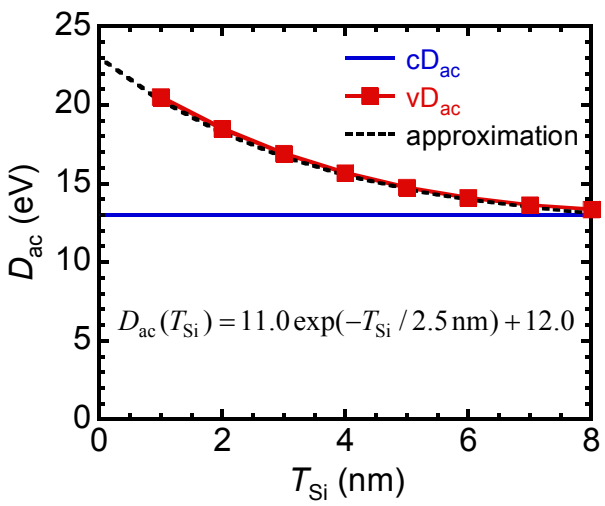

Fig. 3.8 T_{Si} dependency of spatially averaged vD_{ac} in z direction using the lowest subband wave function for the DG MOSFET, where $V_G = 0.5$ V and $V_D = 0$ V. A horizontal blue line is the value for cD_{ac} (13 eV), and a dashed line is obtained using approximation formula shown in the figure.

3.5 Extraction of quasi-ballistic transport parameters

3.5.1 Backscattering coefficient

Next, we extracted quasi-ballistic transport parameters in the DG MOSFET. We evaluated them by directly monitoring particle trajectories crossing over the bottleneck point from source to channel and from channel to source, so we believe that intrinsic values for R, v_{inj}, and v_{back} have been extracted by the present simulation. First, Fig. 3.9 shows the simulated R as a function of L_{ch} and T_{Si}, where the results simulated using cD_{ac} and vD_{ac} models, and also our previous results in ref. 4 are plotted. Note that the lower and upper horizontal axes represent L_{ch} and T_{Si}, respectively.

Comparing the cD_{ac} and vD_{ac} results, vD_{ac} model is found to predict a larger R, as expected. However, the difference between the two D_{ac} results is negligibly small when discussing L_{ch} dependency of R, which is consistent with the results of Fig. 3.7. Hence, we employed cD_{ac} model for subsequent simulations in this

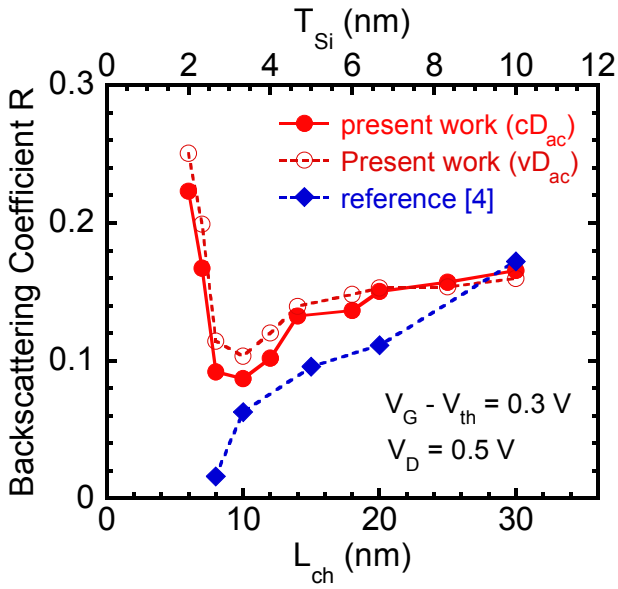

Fig. 3.9 Simulated R as a function of L_{ch} and T_{Si}, where results simulated using cD_{ac} (13 eV) and vD_{ac} models, and also our previous results in ref. 4 are plotted. The lower and upper horizontal axes represent L_{ch} and T_{Si}, respectively.

section.

As for L_{ch} dependency of R, R decreases with reducing L_{ch} until L_{ch} = 10 nm in both the present and previous results. This means that ballistic transport is enhanced due to the channel length scaling down to 10 nm. On the other hand, for L_{ch} < 10 nm, opposite results are obtained. In other words, the present results exhibit the drastic increase in R, whereas the previous results exhibit the monotonous decrease in R. Since our previous results ignored SR scattering, the discrepancy in the sub-10 nm regime is considered due to the influence of SR scattering.

To confirm it, scattering rates for AP and SR scatterings (because these elastic processes mainly cause backscattering to the source) are plotted in Fig. 3.10 for L_{ch} = (a) 10 and (b) 6 nm, where note that they are for the

lowest subband electrons in the 2-fold valleys, which most of electrons occupy. As can be seen in Fig. 3.10 (b), SR scattering, more precisely, SR scattering caused by spatial fluctuation of quantized subbands becomes dominant in the sub-10 nm channel length with T_{Si} < 3 nm. AP scattering rate also increases with reducing L_{ch}, because a form factor included in the AP scattering rate becomes larger for a smaller T_{Si} [5]. However, since the increase in SR scattering rate is much more significant, the increased R observed for L_{ch} < 10 nm is certainly caused by the intensified SR scattering.

Furthermore, by closely looking at the present works in Fig. 3.9, we notice that R starts to more steeply decrease for L_{ch} < 14 nm (T_{Si} < 4.67 nm), which is attributed to the mobility enhancement shown in Fig. 2.11. This means that R has a close relation with electron mobility defined in a diffusive transport regime, and thus, a higher mobility channel would lead to a higher ballistic efficiency of nanoscale MOSFETs.

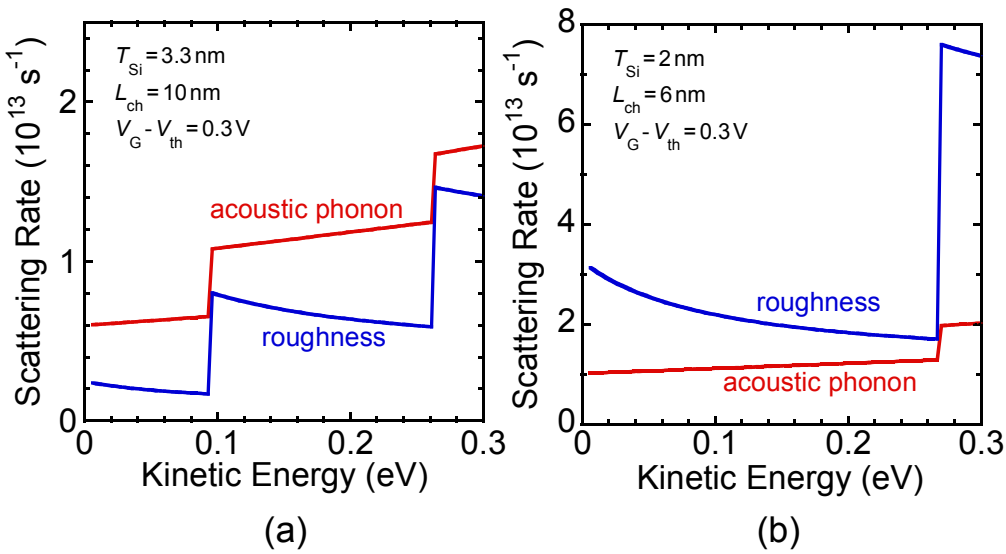

Fig. 3.10 AP (cD_{ac} (13 eV) model) and SR scattering rates for L_{ch} = (a) 10 and (b) 6 nm calculated in the lowest subband of the 2-fold valleys. Note that these elastic processes mainly cause backscattering of carriers to the source.

3.5.2 Injection velocity

The simulated v_{inj} and v_{back} as a function of L_{ch} and T_{Si} are presented in Fig. 3.11, where cD_{ac} (13 eV) model was employed. v_{inj} is almost constant, but it increases for L_{ch} < 10 nm, because electron occupancy of 2-fold valleys, in which electron effective mass is smaller than that of 4-fold valleys, increases when T_{Si} becomes less than 3 ~ 4 nm. As for v_{back}, although the data have fluctuation inherent to the MC particle method, they exhibit nearly constant value around 1.5×10^7 cm/s. From Fig. 3.11, we obtained v_{back} = 0.72 ~ 0.92 v_{inj}, and thus we can reconfirm that the assumption of $v_{back} = v_{inj}$ [1] is not correct in a precise sense [4].

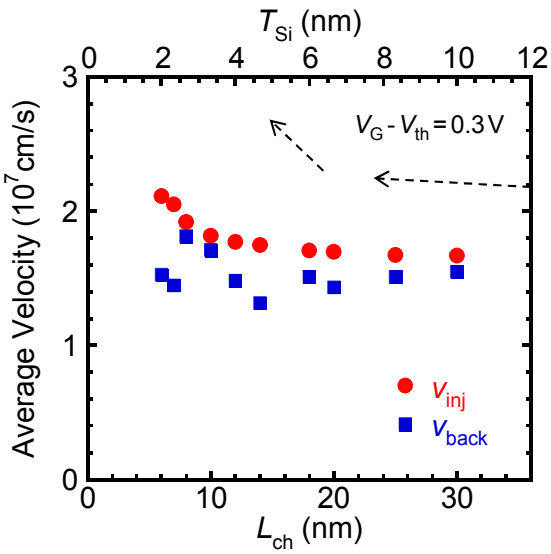

Fig. 3.11 Simulated v_{inj} and v_{back} as a function of L_{ch} and T_{Si}, where cD_{ac} (13 eV) model was employed. We obtained v_{back} = 0.72 ~ 0.92 v_{inj}, and thus the assumption of $v_{back} = v_{inj}$ [1] is not correct in a precise sense.[4)]

3.5.3 On current density

Finally, Figs. 3.12 and 3.13 show L_{ch} dependencies of I_{ON} and $I_D - V_G$ characteristics simulated using the MC simulator, respectively, where I_{ON} in Fig. 3.12 was calculated at $V_G - V_{th}$ = 0.3 V of Fig. 3.13. V_{th} is defined as the gate voltage which corresponds to I_D = 0.01 mA/μm. It is found that I_{ON} increases with reducing L_{ch} until L_{ch} = 10 nm, and then, it sharply decreases in the sub-10 nm regime.

You may already notice that I_{ON} in Fig. 3.12 varies almost inversely with R shown in Fig. 3.9, and therefore, on-current increase or decrease of ultra-scaled DG MOSFETs is found to be basically determined by a quasi-ballistic transport parameter R. Accordingly, the I_{ON} degradation in the sub-10 nm regime is confirmed due to the SR scattering intensified by the spatial fluctuation of quantized subbands. Hence, significant improvement in the quality of gate oxide interfaces is indispensable to receive the benefits of ballistic transport in the sub-10 nm DG/SOI MOSFETs.

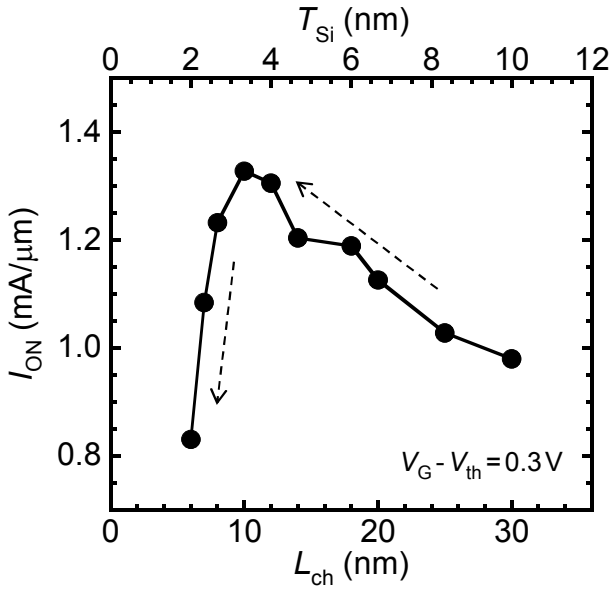

Fig. 3.12 L_{ch} dependency of I_{ON}, where I_{ON} was calculated at $V_G - V_{th}$ = 0.3V of Fig. 3.13. I_{ON} increases with reducing L_{ch} until L_{ch} = 10 nm, and then, it sharply decreases in the sub-10 nm regime. This tendency is coincident with that in an inverse of R shown in Fig. 3.9.

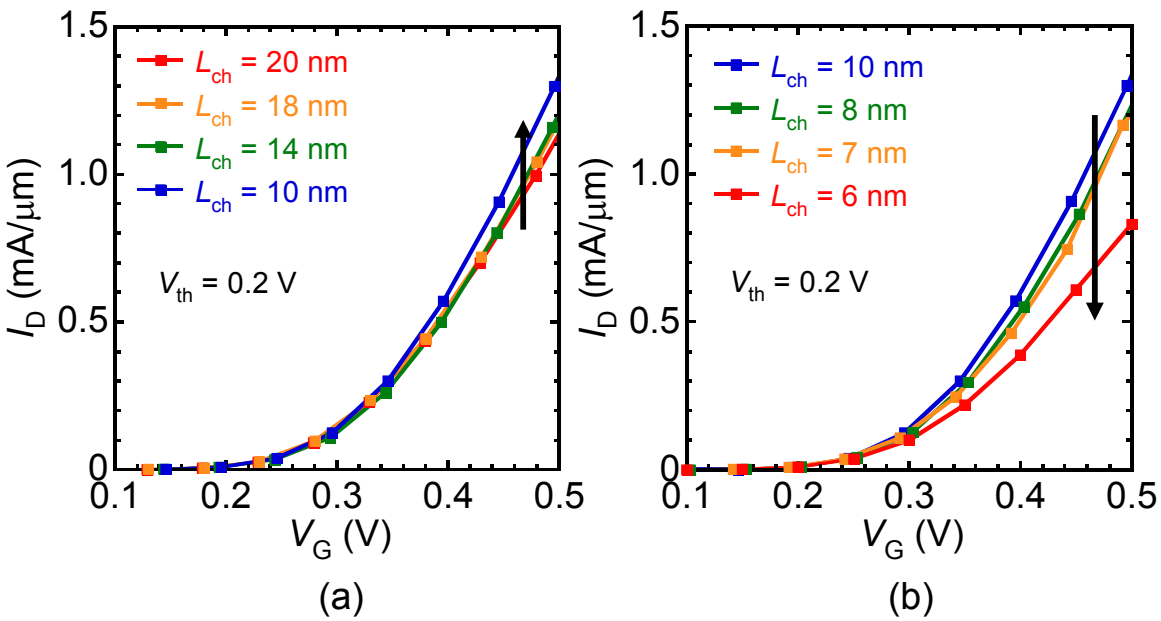

Fig. 3.13 L_{ch} dependency of $I_D - V_G$ characteristics simulated using the MC simulator, where cD_{ac} (13 eV) model was employed. V_{th} was set as 0.2 V, at which I_D = 0.01 mA/μm. L_{ch} is changed (a) from 20 to 10 nm, and (b) from 10 to 6 nm.

3.6 Summary

In this chapter, by using self-consistent multi-subband MC simulator and directly monitoring particle trajectories at the bottleneck point, the quasi-ballistic transport parameters for ultrasmall DG MOSFETs have been evaluated. As a result, it is shown that the consideration of T_{Si}-dependent D_{ac} increases backscattering coefficient R, but its influence on L_{ch} dependency of R is found to be less important. Furthermore, we have demonstrated that ballistic transport in DG MOSFETs is enhanced due to L_{ch} scaling until L_{ch} = 10 nm, but when L_{ch} is further scaled to less than 10 nm according to the $T_{Si} = L_{ch} / 3$ scaling rule to suppress short-channel effects, SR scattering intensified by spatial fluctuation of quantized subbands drastically degrades ballistic transport. In addition, since R has been demonstrated to have a close relation with electron mobility, a higher mobility channel will still lead to a higher ballistic efficiency of nanoscale MOSFETs. On-current behavior of ultra-scaled DG MOSFETs has been confirmed to be basically determined by R, and the quality of gate oxide interfaces must be improved to avoid the drastic increase of R due to SR scattering, and then to improve the device performance in the sub-10 nm regime.

References

[1] M. Lundstrom, IEEE Electron Device Lett. **18**, 361 (1997).

[2] K. Natori, J. Appl. Phys. **76**, 4879 (1994).

[3] K. Uchida, H. Watanabe, A. Kinoshita, J. Koga, T. Numata, and S. Takagi, IEDM Tech. Dig. 2002, p. 47.

[4] H. Tsuchiya, K. Fujii, T. Mori, and T. Miyoshi, IEEE Trans. Electron Devices **53**, 2965 (2006).

[5] K. Natori, IEICE Trans. Electron. **E84-C**, 1029 (2001).

[6] K. Uchida, J. Koga, and S, Takagi, J. Appl. Phys. **102**, 074510 (2007).

4. Quantum transport simulation of nanoscale Si MOSFETs with Wigner Monte Carlo method

As the gate length of the MOSFETs has reduced down to 10 nm scale, not only well-known quantum confinement effect and ballistic transport discussed in the previous chapter but also quantum transport effects along the channel direction such as SD direct tunneling, quantum reflection inside the channel, and quantum repulsion in the source and drain regions have become more and more important [1-3]. Therefore, to analyze the device performances of future MOSFETs precisely, a device simulation considering not only scattering and quantum confinement effects but also quantum transport effects is indispensable.

In this chapter, a quantum transport simulator based on a Wigner Monte-Carlo (WMC) approach, which can fully incorporate quantum transport effects, has been developed. By using the simulator, the influences of quantum transport effects on electrical characteristics of ultra-short channel Si MOSFETs are investigated. The ability of WMC method to describe quantum-classical transition of carrier transport in a diffusive transport regime is also demonstrated.

4.1 Wigner function theory

4.1.1 Derivation of Wigner transport equation (WTE)

Wigner function was derived by E. Wigner [4] and extended for analyzing quantum transport phenomena in resonant-tunneling diodes by W. Frensley [5]. The Wigner function has strong connection with density-matrix operator and the classical Boltzmann equation.

An one-electron Hamiltonian and time-dependent Schrödinger equation is expressed respectively,

$$H(\mathbf{r},\, t) = -\frac{\hbar^2}{2m^*}\frac{\partial}{\partial \mathbf{r}^2} + U(\mathbf{r},\, t)\,, \tag{4.1}$$

$$i\hbar\frac{\partial \varphi_j(\mathbf{r},\, t)}{\partial t} = H(\mathbf{r},\, t)\varphi_j(\mathbf{r},\, t)\,. \tag{4.2}$$

Here, density matrix is introduced as

$$\rho(\mathbf{r},\mathbf{r}',t) = \sum_j P_j \varphi_j(\mathbf{r},t)\varphi_j^*(\mathbf{r}',t)\,. \tag{4.3}$$

This is called the coordinate-displayed density matrix, which describes the non-local correlation of wave function. P_j stands for the occupation probability of a state j, and $\varphi_j(\mathbf{r},t)$ is a wave function for the state j, satisfying Schrödinger equation (4.2). Time evolution of density matrix is obtained by differentiating eq. (4.3) and utilizing (4.2) (and also its complex conjugate) as

$$\begin{aligned}\frac{\partial\rho(\mathbf{r},\mathbf{r}',t)}{\partial t} &= \sum_j P_j\left[\frac{\partial\varphi_j(\mathbf{r},t)}{\partial t}\varphi_j^*(\mathbf{r}',t)+\varphi_j(\mathbf{r},t)\frac{\partial\varphi_j^*(\mathbf{r}',t)}{\partial t}\right]\\ &= \sum_j P_j\left[\frac{1}{i\hbar}H(\mathbf{r},\,t)\varphi_j(\mathbf{r},\,t)\varphi_j^*(\mathbf{r}',t)+\varphi_j(\mathbf{r},t)\left(\frac{1}{-i\hbar}\right)H^*(\mathbf{r}',\,t)\varphi_j^*(\mathbf{r}',\,t)\right]\\ &= \sum_j P_j\left[\frac{1}{i\hbar}H(\mathbf{r},\,t)-\frac{1}{i\hbar}H^*(\mathbf{r}',\,t)\right]\varphi_j(\mathbf{r},\,t)\varphi_j^*(\mathbf{r}',t)\\ &= \frac{1}{i\hbar}[H(\mathbf{r},\,t)-H^*(\mathbf{r}',\,t)]\,\rho(\mathbf{r},\mathbf{r}',t)\end{aligned} \tag{4.4}$$

multiplying $i\hbar$, the dynamical evolution of the density matrix, i.e., quantum Liouville equation is obtained as

$$\begin{aligned}i\hbar\frac{\partial\rho(\mathbf{r},\mathbf{r}',t)}{\partial t} &= [H(\mathbf{r},\,t)-H^*(\mathbf{r}',\,t)]\,\rho(\mathbf{r},\mathbf{r}',t)\\ &= \left[-\frac{\hbar^2}{2m^*}\left(\Delta_{\mathbf{r}}-\Delta_{\mathbf{r}'}\right)+U(\mathbf{r},\,t)-U(\mathbf{r}',\,t)\right]\rho(\mathbf{r},\mathbf{r}',t)\end{aligned} \tag{4.5}$$

We introduce the center of mass coordinate $\mathbf{R}=(\mathbf{r}+\mathbf{r}')/2$ and relative coordinate vectors $\mathbf{u}=\mathbf{r}-\mathbf{r}'$. The coordinate transform is written as

$$\begin{aligned}&\nabla_{\mathbf{r}}=\frac{1}{2}\nabla_{\mathbf{R}}+\nabla_{\mathbf{u}},\ \ \Delta_{\mathbf{r}}=\frac{1}{4}\Delta_{\mathbf{R}}+\nabla_{\mathbf{R}}\cdot\nabla_{\mathbf{u}}+\Delta_{\mathbf{u}},\\ &\nabla_{\mathbf{r}'}=\frac{1}{2}\nabla_{\mathbf{R}}-\nabla_{\mathbf{u}},\ \ \Delta_{\mathbf{r}'}=\frac{1}{4}\Delta_{\mathbf{R}}-\nabla_{\mathbf{R}}\cdot\nabla_{\mathbf{u}}+\Delta_{\mathbf{u}}.\end{aligned} \tag{4.6}$$

By substituting Eq. (4.6) into Eq. (4.5), we obtain

$$i\hbar\frac{\partial\rho(\mathbf{r},\mathbf{r}',t)}{\partial t}=-\frac{\hbar^2}{m^*}\nabla_{\mathbf{R}}\cdot\nabla_{\mathbf{u}}\rho(\mathbf{r},\mathbf{r}',t)+[U(\mathbf{r},\,t)-U(\mathbf{r}',\,t)]\rho(\mathbf{r},\mathbf{r}',t) \tag{4.7}$$

Since the quantum Liouville equation and the WTE are linked by the Wigner-Weyl transform, the Wigner function is defined by the density matrix in mixed representation, which is actually given by the Fourier transform of the density matrix as

$$\begin{aligned}f_w(\mathbf{R},\mathbf{k},t) &= \int_{-\infty}^{\infty}d\mathbf{u}\,\rho\left(\mathbf{R}+\frac{\mathbf{u}}{2},\mathbf{R}-\frac{\mathbf{u}}{2},t\right)e^{-i\mathbf{k}\cdot\mathbf{u}}\\ \rho\left(\mathbf{R}+\frac{\mathbf{u}}{2},\mathbf{R}-\frac{\mathbf{u}}{2},t\right) &= \int_{-\infty}^{\infty}\frac{d\mathbf{k}}{(2\pi)^3}f_w(\mathbf{R},\mathbf{k},t)\,e^{i\mathbf{k}\cdot\mathbf{u}}\end{aligned} \tag{4.8}$$

Wigner function is real-valued, but not always takes positive value. Therefore, negative-valued Wigner function represents the quantum effect including tunneling and interference. The value of the Wigner distribution function (WDF) occasionally becomes negative. Strictly speaking, 'distribution function' never takes negative value in the classical picture, and therefore, this negative value is interpreted as the signature of the system being quantum state. As WDF takes negative value, it can't be interpreted as the probability profile in the phase space. Therefore, correctly, WDF should be called Wigner quasi-distribution function, or simply Wigner function, but here, we use WDF for simplicity.

We find the WTE by taking the Fourier transform of eq. (4.7) with relative coordinate **u**,

$$\frac{\partial f_w}{\partial t} + \mathbf{v} \cdot \nabla_{\mathbf{R}} f_w + \frac{1}{\hbar} \int_{-\infty}^{\infty} \frac{d\mathbf{k}'}{(2\pi)^3} V(\mathbf{R}, \mathbf{k} - \mathbf{k}', t) f_w(\mathbf{R}, \mathbf{k}', t) = 0 \,, \tag{4.9}$$

where

$$-\frac{1}{\hbar} \int_{-\infty}^{\infty} \frac{d\mathbf{k}'}{(2\pi)^3} V(\mathbf{R}, \mathbf{k} - \mathbf{k}', t) f_w(\mathbf{R}, \mathbf{k}', t) \equiv Q f_w$$

is called quantum evolution term, and $V(\mathbf{R}, \mathbf{k} - \mathbf{k}', t)$ is called non-local potential term, which is given by

$$\begin{aligned} V(\mathbf{R}, \mathbf{k} - \mathbf{k}', t) &= i \int_{-\infty}^{\infty} d\mathbf{u}\, e^{-i(\mathbf{k}-\mathbf{k}')\cdot\mathbf{u}} \left[U\left(\mathbf{R} + \frac{\mathbf{u}}{2}\right) - U\left(\mathbf{R} - \frac{\mathbf{u}}{2}\right) \right] \\ &= 2 \int_{0}^{\infty} d\mathbf{u} \sin[(\mathbf{k} - \mathbf{k}') \cdot \mathbf{u}] \left[U\left(\mathbf{R} + \frac{\mathbf{u}}{2}\right) - U\left(\mathbf{R} - \frac{\mathbf{u}}{2}\right) \right] \end{aligned} . \tag{4.10}$$

The transformation of equation (4.10) utilized the odd function nature of the term $[U(\mathbf{R} + \mathbf{u}/2) - U(\mathbf{R} - \mathbf{u}/2)]$. The term means that effects of potential working on the carriers is determined not only by the local potential, but also spatially remote potential also affects the effective potential. This term (4.10) is an extraordinarily significant term to describe quantum mechanical effects such as tunneling.

4.1.2 Relation with other simulation methods

A. Relation with NEGF method

Although WTE is derived from Schrödinger equation in the above discussion, WTE can also be obtained from Dyson's equation used in NEGF method, and in that case, explicit expression of collision term can be obtained [6]. NEGF method and Wigner function method have close relationship, i.e., Wigner function is also defined as an integral of the Fourier-transformed correlation Green's function $-iG^{<}(\mathbf{R}, \mathbf{k}, t, E)$ which is originated from $-iG^{<}(\mathbf{R}, \mathbf{u}, t, E)$ [6].

$$f(\mathbf{R}, \mathbf{k}, t) = -i \int G^{<}(\mathbf{R}, \mathbf{u}, t, E)\, dE \quad . \tag{4.11}$$

The above equation enables us to obtain Wigner transport equation from NEGF with carrier scattering effect. Detailed discussion is found in ref. 6.

Therefore, NEGF and WMC method should give consistent results in the quasi-ballistic limit. To confirm this, a GaAs / AlGaAs double-barrier resonant tunneling diode is simulated using both NEGF method and WMC method. Device structure and the computed current-voltage characteristics by WMC method and NEGF method are shown in Fig. 4.1 (a) and (b), where regardless of materials, only Γ valley are considered, and m^* is assumed to be 0.67 m_0, which is a value of GaAs, and nonparabolicity is not taken into account. The temperature is 300K, and the scattering mechanisms considered are polar optical phonons, elastic acoustic phonons and impurities.

Figure 4.1 (b) shows quite good agreement between the results by WMC and NEGF method. This result shows that NEFT method and WMC method is equivalent in the ballistic limit. Furthermore, In Fig. 4.2, three kinds of current-voltage characteristics computed for no scattering inside the double-barrier region, standard scattering rate and scattering rates multiplied by 5 are shown. As expected, the peak current density decreases and the valley current density increases with scattering rates, and thus the peak-to-valley current ratio reduces by scattering.

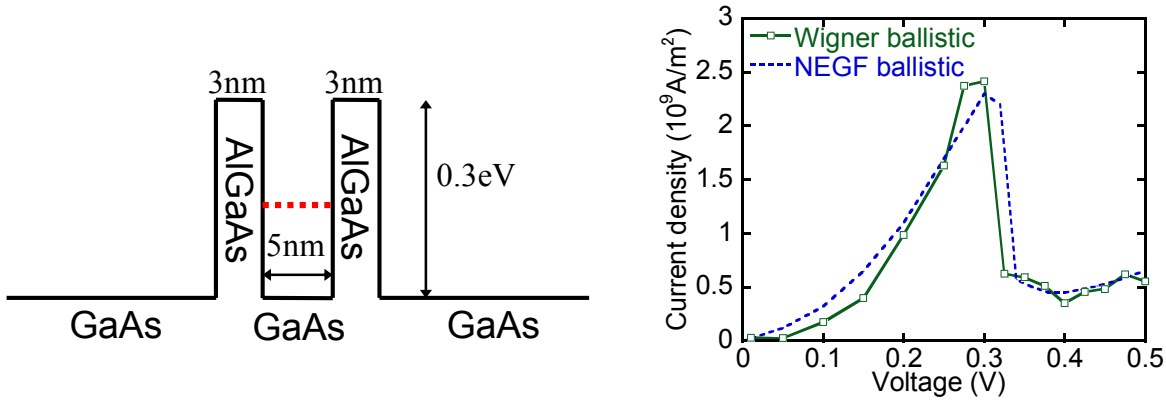

(a) (b)

Fig. 4.1 (a) Device structure of simulated RTD and (b) current-voltage characteristics computed for the RTD. Blue dashed line represents results by NEGF method, and green solid line by WMC method with scattering in intrinsic region excluded.

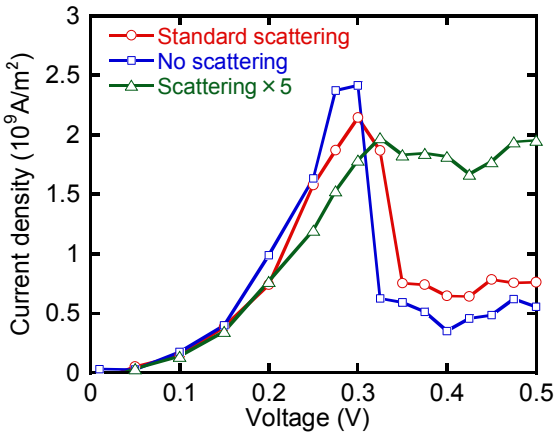

Fig. 4.2 Current-voltage characteristics. Blue line is computed with no scattering inside the double-barrier region, red line with standard scattering rate and green line with scattering rates multiplied by 5.

Such decoherence effects due to scattering can also be verified by rendering the Wigner distribution function in the phase-space at resonant state as shown in Fig. 4.3, where Wigner functions are obtained with (a) no scattering inside the double-barrier region, (b) standard scattering rate and (c) scattering rates multiplied by 5. The signature of electron waves tunneling through the double-barrier and the quantum interference pattern inside the central quantum well we can see in Fig. 4.3 (a) and (b) almost disappear when the scattering rates are increased by 5 times as shown in Fig. 4.3 (c). This scattering-induced decoherence tends to degrade the resonant tunneling property as shown in Fig.4.2, by increasing the valley current to a current level such that the negative resistance becomes almost unobservable.

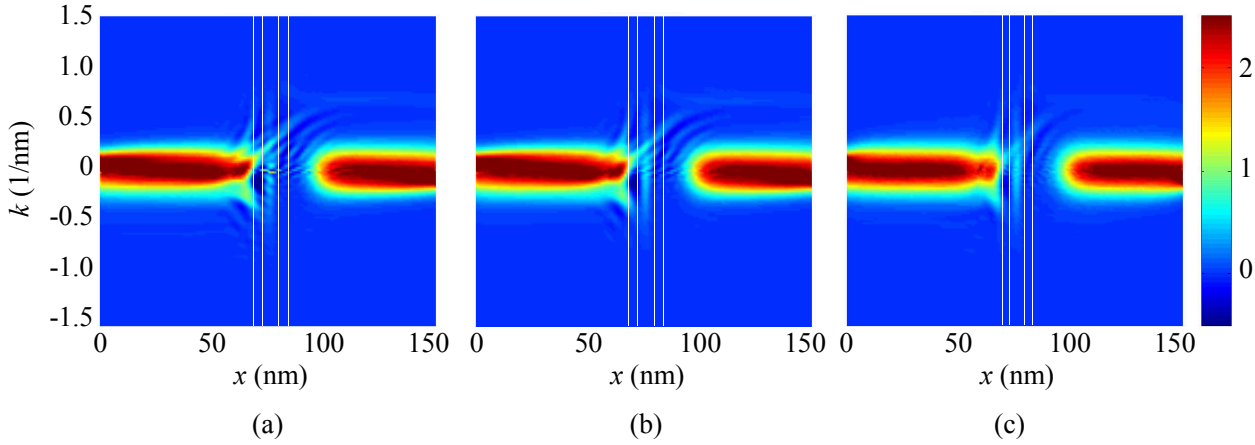

Fig. 4.3 Wigner distribution functions of RTD in the phase-space computed for (a) no scattering inside the double-barrier region, (b) standard scattering rate and (c) scattering rates multiplied by 5. The bias voltage is all set at $V = 0.3$ V.

B. Relation with classical MC method

By using Taylor expansion in the non-local potential term, WTE can be rewritten as

$$\frac{\partial f_w}{\partial t} + \mathbf{v} \cdot \nabla_{\mathbf{r}} f_w + \sum_{\alpha=0}^{\infty} \frac{(-1)^{\alpha+1}}{4^{\alpha} \hbar (2\alpha+1)!} (\nabla_{\mathbf{r}} \cdot \nabla_{\mathbf{k}})^{2\alpha+1} U f_w = C f_w . \tag{4.12}$$

Dividing the third term of the left hand into 0-th order term and higher order terms ($\alpha \geq 1$) yields

$$\frac{\partial f_w}{\partial t} + \mathbf{v} \cdot \nabla_{\mathbf{r}} f_w - \frac{1}{\hbar} \nabla_{\mathbf{r}} U \cdot \nabla_{\mathbf{k}} f_w + \sum_{\alpha=1}^{\infty} \frac{(-1)^{\alpha+1}}{4^{\alpha} \hbar (2\alpha+1)!} (\nabla_{\mathbf{r}} \cdot \nabla_{\mathbf{k}})^{2\alpha+1} U f_w = C f_w , \tag{4.13}$$

where the third term of the left hand corresponds to the classical drift term in BTE. The fourth term is called quantum correction term, which describes non local quantum mechanical effects. This is why WTE is called quantum mechanical BTE. Here, by using relation $\mathbf{p} = \hbar \mathbf{k}$, eq. (4.13) yields

$$\frac{\partial f_w}{\partial t} + \frac{1}{m^*} \mathbf{p} \cdot \nabla_{\mathbf{r}} f_w - \nabla_{\mathbf{r}} U \cdot \nabla_{\mathbf{p}} f_w + \sum_{\alpha=1}^{\infty} \frac{(-1)^{\alpha+1} h^{2\alpha}}{4^{\alpha} (2\alpha+1)!} (\nabla_{\mathbf{r}} \cdot \nabla \mathbf{p})^{2\alpha+1} U f_w = C f_w . \tag{4.14}$$

In the classical limit ($\hbar \to 0$) of this equation, the fourth term of the left hand vanishes as

$$\frac{\partial f_w}{\partial t} + \frac{1}{m^*} \mathbf{p} \cdot \nabla_{\mathbf{r}} f_w - \nabla_{\mathbf{r}} U \cdot \nabla_{\mathbf{p}} f_w = C f_w , \tag{4.15}$$

which is Boltzmann transport equation. Therefore, WTE can be assumed as a direct expansion of classical Boltzmann transport equation into the quantum mechanics. Therefore, WTE has close relation with BTE. Also, as you can see from eq. (4.14), for slowly varying potential, BTE and WTE are expected to give similar results, as fourth term of eq. (4.13) quickly vanishes when spatial variation of potential profile $U(\mathbf{r})$ is slow enough. In particular, when potential is unvaried or linear proportional to x, i.e., uniform electric field is applied, the fourth term completely vanishes. Quantum corrected MC method mentioned in chapter 1 can be also derived from above expression of eq. (4.13), which will be discussed later.

To demonstrate that WMC method is consistent with BMC method in the long-channel devices, a GaAs

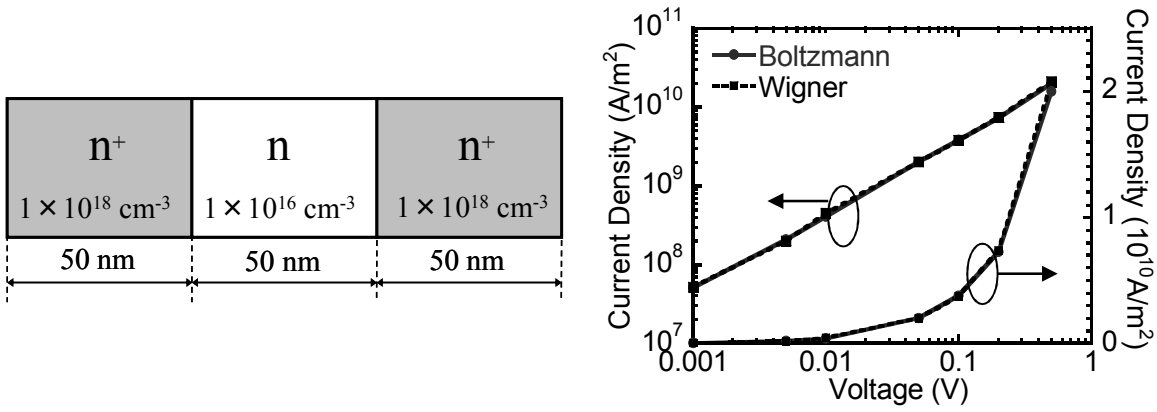

(a) (b)

Fig. 4.4 (a) Device structure of simulated GaAs n^+–n–n^+ diode with 50nm contact region and 50nm intrinsic region, and (b) current-voltage characteristics computed for the device. Solid lines represent results by BMC method, and dashed lines by WMC method.

n^+–n–n^+ diode with 50nm contact region and 50nm intrinsic region as shown in Fig. 4.4 (a) is simulated [1]. Here, as in simulation of RTD, only Γ valley are considered, m^* is assumed to be 0.67 m_0, and nonparabolicity is not taken into account. As a result, as shown in the current voltage characteristics in Fig. 4.4 (b), it is shown that for the devices with slowly varying potential profile or ones without any quantum structures, WMC method is equivalent to the BMC method.

This result also justifies the direct comparison of results by BMC and WMC, i.e., difference in BMC and WMC results is shown to directly indicate the difference in classical mechanics based results and quantum mechanics based results.

C. Relation with quantum corrected MC method

As for comparison with quantum corrected (QC) MC method, QCMC obeys following transport equation [7]

$$\frac{\partial f}{\partial t} + \frac{1}{m^*}\mathbf{p}\cdot\nabla_{\mathbf{r}} f - \nabla_{\mathbf{r}}(U + U^{\mathrm{QC}})\cdot\nabla_{\mathbf{p}} f = Cf\,, \tag{4.16}$$

which is derived from eq. (4.13) considering the lowest quantum correction term $(\alpha = 1)$, where U^{QC} is called quantum correction potential, defined as

$$U^{\mathrm{QC}} = -\frac{\hbar^2}{12}\left(\frac{1}{m_x^*}\frac{\partial^2 \ln(n)}{\partial x^2} + \frac{1}{m_y^*}\frac{\partial^2 \ln(n)}{\partial y^2} + \frac{1}{m_z^*}\frac{\partial^2 \ln(n)}{\partial z^2}\right). \tag{4.17}$$

The QC potential (4.17) is derived from the lowest quantum correction term in eq. (4.16) As is clear from the derivation of eq. (4.17), QCMC method is also based on WTE as in WMC method, and the advantage of QCMC is that the method can be assumed the same equation as BTE with identifying $U + U^{\mathrm{QC}}$ as a potential profile. With a little modification of the simulator, conventional BMC simulator can be expanded to QCMC simulator. As is illustrated in Fig. 4.5 (a) and (b), quantum tunneling effect can be described through potential lowering, and quantum confinement effect can be described with smoothed potential. However, as mentioned, QCMC method is derived from the lowest quantum correction term $(\alpha = 1)$, and thus, QCMC can't express all the quantum effects.

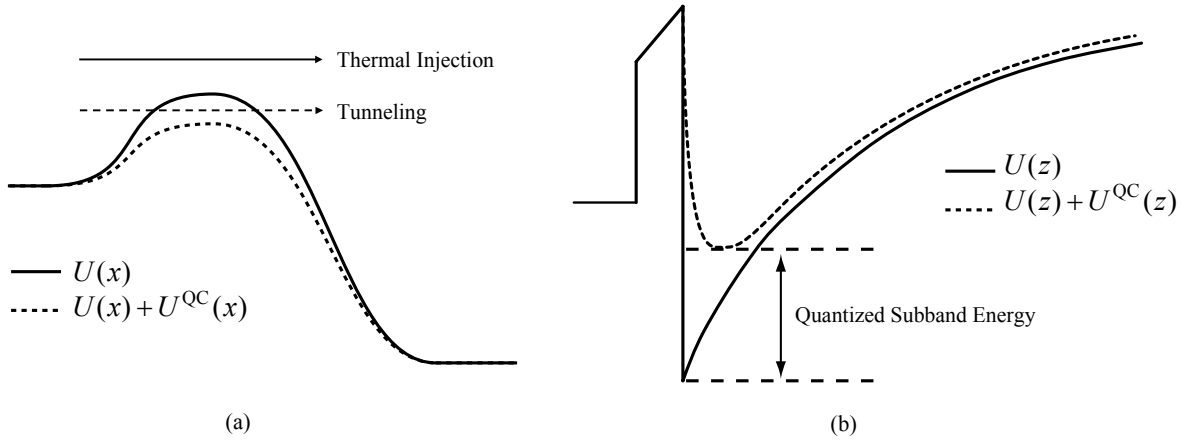

Fig. 4.5 Schematic view of U^{QC} for MOSFETs along (a) transport direction and (b) confinement direction.

For instance, resonant tunneling, quantum reflection, and higher quantized subbands can't be described in QCMC method. In contrast, NEGF, direct solution of WTE, and WMC method proposed in this dissertation can rigorously incorporate quantum transport effect.

4.1.3 Direct solution approach of WTE and its problems

As well as NEGF method, direct solution of WTE has been one of the options to solve quantum transport problem before WMC method was developed. Since 1980s, there have been many studies on the direct solution of WTE using matrix expression [8–10]. In addition, application results on realistic MOSFETs have been reported recently [11–13].

There are some differences between direct solution of WTE and WMC method in terms of treatment in diffusion term and collision term. The difference is discussed here.

A. Problem in treatment of diffusion term

WTE is shown again.

$$\frac{\partial f_w}{\partial t} + \mathbf{v}\cdot\nabla_{\mathbf{R}} f_w + \frac{1}{\hbar}\int_{-\infty}^{\infty}\frac{d\mathbf{k}'}{(2\pi)^3} V(\mathbf{R},\mathbf{k}-\mathbf{k}',t)\, f_w(\mathbf{R},\mathbf{k}',t) = 0\,. \tag{4.18}$$

In direct solution of WTE, discretization of a diffusion term, which is the second term of this equation, is necessary. Although many discretization methods have been proposed, it is shown that introduction of third differential scheme (TDS) can make significant improvement in simulation accuracy so that subthreshold slope of the MOSFET can be estimated [11–13]. On the other hand, as shown in ref. 10, new discretization method has been proposed until now, and consensus is yet to be reached.

WMC method has an advantage in this point, i.e., WMC method doesn't require discretization of diffusion term because diffusion term is directly described by the equations-of-motion of MC particles.

B. Problem in treatment of collision term

Another difference is the treatment of collision term Cf_w. In direct solution of WTE, relaxation-time approximation [11,13] or the same collision term as in BTE [13] is used. Relaxation time approximation (RTA) doesn't describe energy dependency of scattering rate, nor scattering angle treatment. On the other hand, collision term of BTE is a better approach to include scattering compared to RTA. However, in direct solution of WTE, inelastic scattering and inter-valley scattering, is incredibly difficult to include. As far as I know, there is no successful report on the inclusion of such scattering mechanism into the direct solution of WTE.

WMC method has an advantage in this point, again. Although advanced topics such as collisional broadening [6] and intra-collisional field effect [14] have not been studied on WMC method yet, if the same collision term as in BTE is used in the WMC method, many scattering process, including inelastic, inter-valley, and inter-subband scattering can be easily taken into account. The validity of this approximation will be discussed in subsection 4.3.6 and ref. 1.

4.2 Discretization of phase space and quantum evolution term

In this section, procedure needed for solving WTE by MC method is considered. Hereafter, I consider one-dimensional (1D) WTE, i.e., transport direction is set as x and potential profile along the y and z direction, which is vertical to the transport direction, is assumed to be uniform or slowly varying. k_y- and k_z-depencency of the WDF function can be neglected by integrating eq. (4.9) in the k_z–k_y plane. Also hereafter, Boltzmann distribution function is referred as $f(x,k,t)$ and WDF is referred with subscript 'w' as $f_w(x,k,t)$, as these two distribution function are compared so many times in the thesis.

As a result, 1D WTE is expressed as

$$\frac{\partial f_w}{\partial t} + \frac{\hbar k}{m_x^*}\frac{\partial f_w}{\partial x} + \frac{1}{\hbar}\int_{-\infty}^{\infty}\frac{dk'}{2\pi}V(x,k-k')f_w(x,k',t) = Cf_w, \tag{4.19}$$

where Cf_w is a collision term which is added formally. Non-local potential term is also expressed as

$$V(x,k-k') = 2\int_0^{\infty} du \sin[(k-k')u]\left[U\left(x+\frac{u}{2}\right) - U\left(x-\frac{u}{2}\right)\right]. \tag{4.20}$$

Distribution function in eq. (4.19) is integrated in k_z–k_y plane. Thus this is different from the one in (4.9).

Discretization of real space mesh is also required in BMC in order to solve Poisson's equation. In contrast, to solve the WTE with WMC method, quantum evolution term, non-local potential term, and distribution function must be obtained. For the sake, not only real space but also wave number along the transport direction must be discretized. Non-local potential term also can't be treated as continuous, so the term is also discretized.

4.2.1 Discretization of phase space

A. Conventional discretization

We consider discretized phase space as in Fig. 4.6. Horizontal and vertical axes stand for position and wave number. Upper half of the phase space means positive wave number $k > 0$, i.e., particles in the upper half move rightward. Similarly, particles in the lower half of the phase space move leftward. Simulation region is assumed to be $0 \le x \le L$.

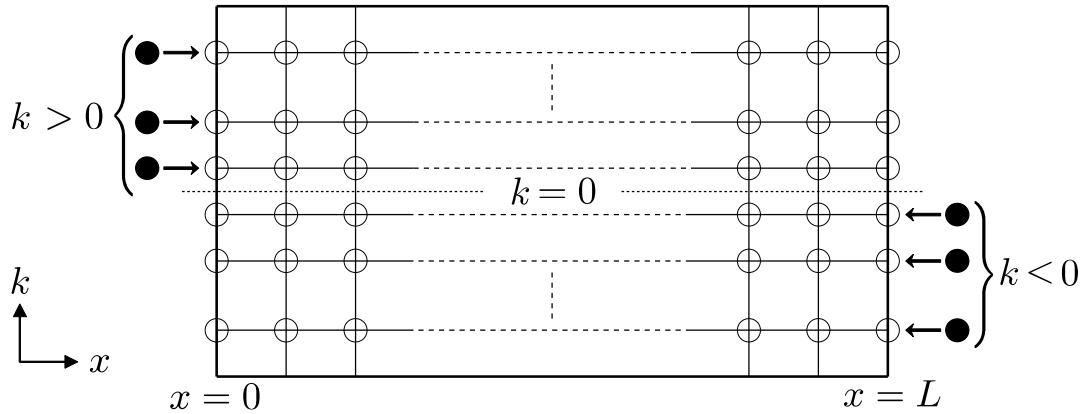

Fig. 4.6 Schematic view of discretized phase space.

In the solution of WMC, a uniform meshing is required, at least for the non-local potential term, because discrete Fourier transform is used in the solution of WTE. If meshing for non-local potential term is separated to that for Poisson's equation and MC method with a careful mathematical and physical consideration, the use of non-uniform mesh in the solution of Poisson's equation of MC method could be allowed.

First, as for position, device region is meshed into a uniform interval as

$$x \in \{0,\ \Delta_x,\ 2\Delta_x, \ldots,\ L\}, \tag{4.21}$$

where the total number of mesh points is determined uniquely as $N_x = L/\Delta_x + 1$. Discretiation of relative coordinate u is treated dependently on discretization of position x as

$$u \in \{0,\ 2\Delta_x,\ 4\Delta_x, \ldots,\ 2N_u\Delta_x\}, \tag{4.22}$$

where N_u represents the total mesh point number of the coordinate u, and determination of N_u will be described later. Non-local potential term is expressed as a Fourier transform of $[U(x+u/2) - U(x-u/2)]$ regarding the coordinate u, thus it has a period of

$$\frac{2\pi}{2\Delta_x} = \frac{\pi}{\Delta_x} \tag{4.23}$$

in k space. Therefore, as for k space, domain $-\pi/2\Delta_x \le k \le \pi/2\Delta_x$ is discretized into mesh number N_k as

$$k \in \left\{ -\frac{\pi}{2\Delta_x} + \frac{\pi}{\Delta_x N_k}\left(j - \frac{1}{2}\right) \right\} = \left\{ \frac{\pi}{\Delta_x}\left(\frac{j - 1/2}{N_k} - \frac{1}{2} \right) \right\}, \tag{4.24}$$

which means $\Delta k = \pi / N_k \Delta_x$.

B. Discretization method used in this thesis

Within conventional discretization method, simulation domain of k space is dependent on the x mesh discretization Δ_x as $-\pi/2\Delta_x \le k \le \pi/2\Delta_x$, which is inconveniency of Wigner function method because uniform real space meshing is required. This constraint is a nuisance for the simulation of long channel devices. Also, for the simulation of materials with heavier transport mass, which usually have large wave number, it is likely that wave number exceeds upper limit of the k domain. To prevent this from occurring, a small Δ_x is required, which means larger number of real space meshes, and therefore, computational time.

Here, note that Δ_k depends not on Δ_x, but on Δ_u. Therefore, interpolation of $U(x)$ enables us to configure Δ_x and period of k space independently. In that case, quantization method is modified as follows. Discretization of relative coordinate u is treated *independently* on discretization of position x as

$$u \in \{0,\ \Delta_u,\ 2\Delta_u, ...,\ N_u\Delta_u\}. \tag{4.25}$$

In that case, k space has a period of

$$\frac{2\pi}{\Delta_u} \tag{4.26}$$

Limitation of the wave space simulation domain can be avoided like this. Using this condition, k space domain $-\pi/\Delta_u \le k \le \pi/\Delta_u$ is discretized into mesh number N_k as

$$k \in \left\{ -\frac{\pi}{\Delta_u} + \frac{2\pi}{\Delta_u N_k}\left(j - \frac{1}{2}\right)\right\} = \left\{ \frac{2\pi}{\Delta_u}\left(\frac{j-1/2}{N_k} - \frac{1}{2}\right)\right\}, \tag{4.27}$$

which means $\Delta_k = 2\pi/N_k\Delta_u$. As is clear from eq. (4.26), wide wave space domain requires small Δ_u. Potential at the meshpoint of relative coordinate $u \in \{0,\ \Delta_u,\ 2\Delta_u, ...,\ N_u\Delta_u\}$ must be obtained in some way.

4.2.2 Discretization of quantum evolution term

Next, quantum evolution term Qf_w is discretized. mesh point indices of x, k, k', and u are introduced as n, j, j', and i. Therefore, $V(x, k-k')$ corresponds with $V_{n,j-j'}$ in the discretized space.

Equation (4.20) yields

$$\begin{aligned} V(x,k-k') &= 2\int_0^\infty du \sin[(k-k')u]\left[U\left(x+\frac{u}{2}\right) - U\left(x-\frac{u}{2}\right)\right] \\ \Rightarrow V_{n,j-j'} &= 2\Delta_u \sum_{i=0}^{N_u} \sin[i(j-j')\Delta_k\Delta_u]\cdot\left[U\left(n\Delta_x + \frac{i\Delta_u}{2}\right) - U\left(n\Delta_x - \frac{i\Delta_u}{2}\right)\right] \end{aligned}. \tag{4.28}$$

The term is assigned to Qf_w, yielding

$$\begin{aligned} Qf_w(x,k,t) &= -\frac{1}{\hbar}\int_{-\infty}^{\infty}\frac{dk'}{2\pi}V(x,k-k')f_w(x,k',t) \\ &\Rightarrow \frac{1}{\hbar}\sum_{j'=1}^{N_k}\frac{\Delta_k}{2\pi}V_{n,j-j'}f_{n,j'} \\ &\Rightarrow \frac{1}{\hbar}\sum_{j'=1}^{N_k}\frac{2}{N_k}\sum_{i=0}^{N_u}\sin[i(j-j')\Delta_k\Delta_u]\cdot\left[U\left(n\Delta_x + \frac{i\Delta_u}{2}\right) - U\left(n\Delta_x - \frac{i\Delta_u}{2}\right)\right]f_{j',n}, \end{aligned} \tag{4.29}$$

where $\Delta_k = 2\pi/N_k\Delta_u$ is utilized. If $\Delta_u = 2\Delta_x$ is assigned, *Qfw* is rewritten as

$$Qf_w(x,k,t) = \frac{1}{\hbar}\sum_{j'=1}^{N_k}\frac{2}{N_k}\sum_{i=0}^{N_u}\sin[2i(j-j')\Delta_k\Delta_x]\cdot\{U[(n+i)\Delta_x]-U[(n-i)\Delta_x]\}f_{j',n}, \tag{4.30}$$

which is based on conventional discretization approach.

As for the relation between N_u and N_k, there are many arguments and consensus is not reached. However, in this study, relation between N_u and N_k is derived from the mathematical requirement.

The term

$$\sum_{i=0}^{N_u}\sin[i(j-j')\Delta_k\Delta_u]\cdot\left[U\left(n\Delta_x+\frac{i\Delta_u}{2}\right)-U\left(n\Delta_x-\frac{i\Delta_u}{2}\right)\right] \tag{4.31}$$

in Equation (4.29) represents discrete sin transform (DST), which requires

$$N_u = \frac{1}{2}N_k\,. \tag{4.32}$$

Therefore, the most accurate result is obtained when simulation is conducted under this relation. However, note that this relation is not mandatory, though strongly desirable. If mesh is set as $N_u = N_k/2\ell$ $(\ell = 1, 2, ...)$, that means that resolution of Wigner function along k axis is reduced. Nevertheless, calculation result is reliable unless the resolution is too coarse or N_u is too small.

If integration range of relative coordinate u is outside the device region,

$$\begin{aligned} U(x) &= U(0)\ (x<0) \\ U(x) &= U(L)\ (x>L) \end{aligned} \tag{4.33}$$

is used. Also, to include non-local effect of whole simulation region,

$$N_u\Delta_u \geq L(=N_x\Delta_x) \tag{4.34}$$

is required. For example, if mesh spacing is set as $\Delta_u = 2\Delta_x$, requirement from eq. (4.34) is $N_u \geq N_x/2$. Therefore, $N_k = 2N_u \geq N_x$ is the ideal relation. On the other hand, since wave number is a physical quantity, N_k must be set enough finely so as not for simulation result to be changed.

Also, it is pointed out in Querlioz et al [1] that any N_u that satisfies

$$N_u < \frac{1}{2}N_k \tag{4.35}$$

is acceptable, and they set N_u position-dependently so that the integrated meshes are all included in the device region, which means that N_u is changed by the position x. In fact, the author confirmed that relation between N_u and N_k has little to do WMC simulation result unless N_u is too small and Δ_k is too coarse. However, this setting of N_u is not recommendable, as it doesn't satisfy the requirements from the DST, and I also confirmed that Wigner distribution function obtained by their approach is distorted at the source or drain end, in particular drain end, compared to the ideal one obtained with $N_u = N_k/2$. Therefore, in this thesis, $N_u = N_k/2$ or $N_u = N_k/4$ is consistently used.

One might notice that if the odd function nature of nonlocal potential term is neglected, eq. (4.31) is changed into discrete Fourier transform (DFT), resulting in relation $N_u = N_k$. However, in that case, integration range is also changed to $-N_u/2 \leq i \leq N_u/2$, hence $N_u = N_k$ in DFT and $N_u = N_k/2$ in the discrete sine transform indicate the same transform.

4.3 Multi-subband Wigner Monte Carlo (MSWMC) method

Self consistent MSMC method is already discussed in chapter 3. Here, treatment of WTE in the MC method is mainly discussed.

4.3.1 Wigner transport equation on the quantized subband profile

In simulation of DG MOSFETs, 3D Wigner transport equation is integrated along the depth (y) direction and coordinate y, k_y is removed, resulting in 2D WTE. Then 2D WTE is decoupled into the 1D WTE along the transport (x) direction and 1D Schrödinger equation along the confinement direction z. Then, Wigner distribution function is defined for each quantized subband n for 2-fold and 4-fold valleys. As a result, 1D WTE is expressed as

$$\frac{\partial f_w^{n,\nu}}{\partial t} + \frac{\hbar k}{m_{\nu,x}^*}\frac{\partial f_w^{n,\nu}}{\partial x} + \frac{1}{\hbar}\int_{-\infty}^{\infty}\frac{dk'}{2\pi}V^{n,\nu}(x,k-k')f_w^{n,\nu}(x,k',t) = Cf_w^{n,\nu}, \tag{4.36}$$

where n represents the subband index, and ν valley index. Although eq. (4.36) seems the same expression as eq. (4.19), $f_w^{n,\nu}$ is integrated only along k_y direction and defined for each valley and subband. Thus, eq. (4.36) is intrinsically different from eq. (4.19). Non-local potential term is expressed as

$$V^{n,\nu}(x,k-k') = 2\int_0^{\infty} du \sin[(k-k')u]\left[E_n^{\nu}\left(x+\frac{u}{2}\right) - E_n^{\nu}\left(x-\frac{u}{2}\right)\right], \tag{4.37}$$

where $E_n^{\nu}(x)$ represents n–th quantized subband energy profile of a valley ν at position x, and therefore treatment of quantized subbands is taken into account.

In the following subsections, valley and subband index are not explicitly shown for simplicity of the discussion, but all the procedures discussed below are done with each valley and subband, respectively.

4.3.2 Introduction of quasi-particles weighted by 'affinity'

Classical distribution function for each mesh is usually expressed as the sum of the number of particles which exists in the mesh as

$$f(x,\ k,\ t) = \sum_{i\in M(x,k)} 1 \quad \left(= \sum_i \delta_{x,x_i(t)}\delta_{k,k_i(t)}\right), \tag{4.38}$$

where i is the index of particles (therefore, $x_i(t)$ and $k_i(t)$ stands for i-th particle's position and wave number), $M(x,k)$ is each simulation mesh in the phase space, and $\delta_{i,j}$ is Kronecker's delta. The expression means that a distribution function always takes non-negative value. In contrast, as already mentioned, Wigner function is known to take negative value. Thus, eq. (4.38) can't be used as the expression of Wigner distribution function. That means that WTE can't be solved in conventional MC method.

Therefore, to resolve this problem, a new quantity called 'affinity' is introduced. An affinity for i-th particle at a certain time t is expressed as $A_i(t)$. Then, distribution function is expressed as

$$f_w(x,\ k,\ t) = \sum_{i \in M(x,k)} A_i(t) \quad \left(= \sum_i \delta_{x,x_i(t)} \delta_{k,k_i(t)} A_i(t) \right). \tag{4.39}$$

Here, if $A_i(t)$ is 1, eq. (4.39) is coincident with eq. (4.38). A distribution function can take negative value if affinities are allowed to have negative values.

Next, this affinity approach is validated from mathematical and physical viewpoints. WTE is rewritten as

$$\frac{\partial f_w}{\partial t} = -\frac{\hbar k}{m_x^*} \frac{\partial f_w}{\partial x} + Qf_w + Cf_w, \tag{4.40}$$

where

$$Qf_w(x,k,t) = -\frac{1}{\hbar} \int_{-\infty}^{\infty} \frac{dk'}{2\pi} V(x, k-k') f_w(x,k',t). \tag{4.41}$$

In this representation of eq. (4.40), WTE's physical meaning becomes clear, i.e., time change of Wigner function is described by three term: diffusion term, quantum evolution term, and collision term.

Here, differentiation of eq. (4.39) yields

$$\frac{\partial f_w(x,\ k,\ t)}{\partial t} = \sum_{i \in M(x,k)} \frac{dA_i(t)}{dt}. \tag{4.42}$$

Comparing the right hand of eq. (4.40) and (4.42),

$$\sum_{i \in M(x,k)} \frac{dA_i(t)}{dt} = -\frac{\hbar k}{m_x^*} \frac{\partial f_w}{\partial x} + Qf_w + Cf_w \tag{4.43}$$

is obtained. On the other hand, since the first term, or diffusion term, is the same one as in BTE, this term is treated similarly as BMC method. Also, collision term Cf_w can be also treated similarly as BMC, as shown in ref. 1. In that case, the last remainder in right hand of eq. (4.43) is Qf_w. Therefore,

$$\sum_{i \in M(x,k)} \frac{dA_i(t)}{dt} = Qf_w. \tag{4.44}$$

In this case, sum of the change in each particle's affinity means time change of the distribution function due to quantum evolution term. However, as shown in above discussion, particles in WMC method isn't affected by drift term, because drift term is absent. Therefore, MC particles in the WMC method are not representatives of real particles but merely a mathematical tool for simulation. Therefore, the particles to which the affinity is introduced is called 'quasi'-particles.

4.3.3 Equations-of-motion for quasi-particles

The discussion above is summerized here. For BMC and WMC, transport equation solved, equations-of-motion used, and expression of distribution function used are listed in Table 4.1. Note that wave number k_i is constant with time, because the classical drift term is already incorporated in the affinity change via the quantum evolution term of Eq. (4.42). In other words, quantum transport of carriers is described by the temporal change in the weight of particles moving at a constant velocity. Therefore, wave number of MC particles is changed only by scattering event.

TABLE 4.1: Comparisons of transport equation, equations-of-motion, and expression of distribution function used in BMC and WMC method.

	BMC	WMC
Transport equation	$\frac{\partial f}{\partial t} = -\frac{\hbar k}{m_x^*}\frac{\partial f}{\partial x} + \frac{1}{\hbar}\frac{\partial U}{\partial x}\frac{\partial f}{\partial k} + Cf$	$\frac{\partial f_w}{\partial t} = -\frac{\hbar k}{m_x^*}\frac{\partial f_w}{\partial x} + Qf_w + Cf_w$
Equations-of-motion	$\begin{cases} \frac{dx_i}{dt} = v \\ \frac{dk_i}{dt} = -\frac{1}{\hbar}\frac{\partial U(x)}{\partial x} \end{cases}$	$\begin{cases} \frac{dx_i}{dt} = v \\ \frac{dk_i}{dt} = 0 \\ \sum_{i \in M(x,k)} \frac{dA_i(t)}{dt} = Qf_w \end{cases}$
Expression of distribution function	$f(x,\ k,\ t) = \sum_i \delta_{x,x_i(t)}\delta_{k,k_i(t)}$	$f_w(x,\ k,\ t) = \sum_i \delta_{x,x_i(t)}\delta_{k,k_i(t)}A_i(t)$

From an intuitive viewpoint, BMC method regards MC particles as a real carrier and carrier transport is simulated by monitoring them. On the other hand, WMC method regards MC particles as a mathematical tool as discussed above, and affinity change of the particles moving in a fixed speed express transport of carrier.

4.3.4 Injection scheme of quasi-particles into phase space

In our WMC approach, the effect of quantum evolution term Qf_w is taken into account by the concept of affinity. However, quasi-particles are distributed in a quite limited portion of meshes in the phase space, in spite of Qf_w's presence in all meshpoints. This fact may result in failure to describe time evolution of Wigner distribution function in empty meshes.

Therefore, to avoid this contradiction, each mesh in phase space must have at least one quasi particle. However, injection of quasi particles into every empty mesh is a burden in terms of simulation efficiency. One solution to the problem is as follows: the number of quasi particles are counted for every mesh in the phase space and if an empty mesh has a significant value of $|Qf_w|$, quasi particles with zero affinity are injected as in Fig. 4.7. This particle doesn't exist in reality. However, as previously mentioned, a quasi-particle is a mathematical tool in WMC method not an real electron. Thus, injection of particle with zero affinity makes no problem, because there is no inconsistency in terms of the mathematical consideration. Rather, this injection is a requirement of exact calculation.

However, in fact, $Qf_w(x,k,t)$ in each mesh is generally non-zero. If quasi-particles are injected into every mesh that satisfies $|Qf_w| \neq 0$, a tremendous number of particles are needed to the calculation, and WMC method becomes inefficient. Therefore, threshold value α for injecting quasiparticle is introduced.

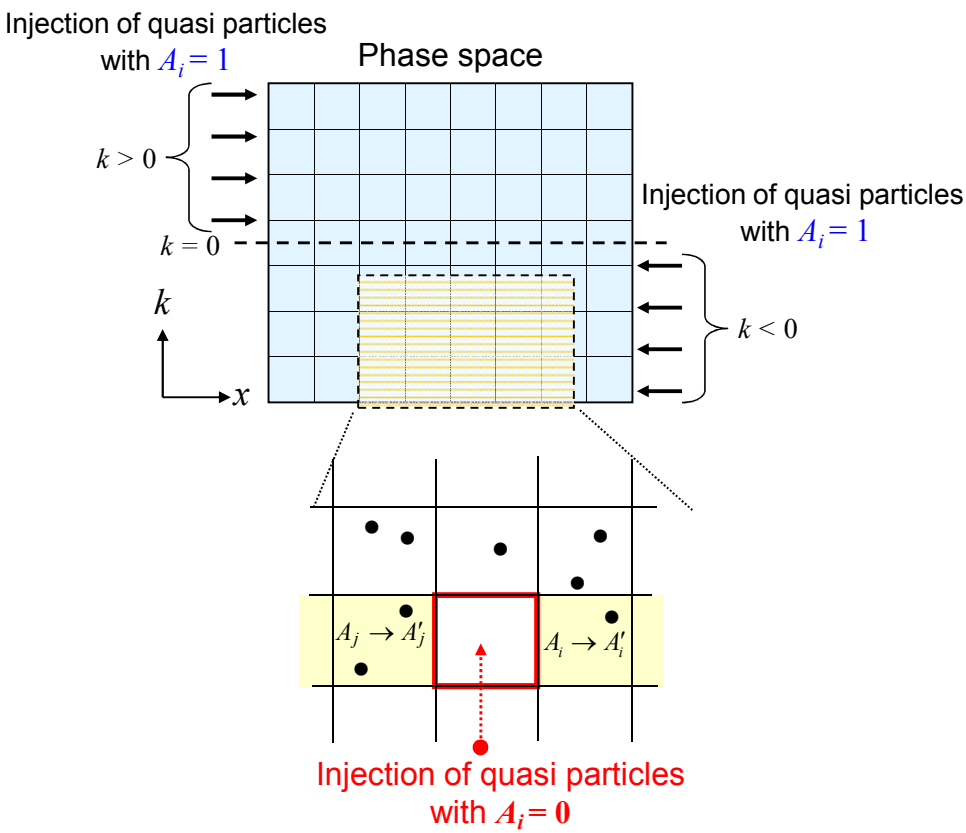

Fig. 4.7 Schematic view of quasi particle injection into the empty mesh.

The threshold value α is set as following concept. If equation of affinity evolution, which is described as

$$\sum_{i \in M(x,k)} \frac{dA_i(t)}{dt} = Qf_w(x,k,t) \tag{4.45}$$

is discretized, resulting equation is as follows:

$$A_i(t+\Delta_t) = A_i(t) + \frac{\Delta_t}{\sum_{i \in M(x,k)} 1} \times Qf_w(x,k,t+\Delta_t)\,. \tag{4.46}$$

On the other hand, the value of affinity given to classical particles is 1, and thus, if $\Delta_t \times Qf_w(x,k,t+\Delta_t)$ is sufficiently smaller than 1, time evolution of affinity in the mesh is considered negligible. Therefore, the acceptable error $\%_{\mathrm{err}}$ is set as

$$\alpha = \frac{\%_{\mathrm{err}}}{\Delta_t}\,. \tag{4.47}$$

For example, if error of less than 1% is assumed negligible, then $\alpha \le 0.01/\Delta t$ is the requirement. As $\Delta t = 0.5 \times 10^{-16}$ s is typically used in the simulations in this thesis, $\alpha \le 2.0 \times 10^{14}\ \mathrm{s}^{-1}$ is the requirement. The value derived from $\alpha \le 0.01/\Delta t$ perfectly corresponds to the value we empirically used for stable simulation. Therefore we consider this relation to be valid. In reality, α is set to the value smaller enough than $0.01/\Delta t$.

4.3.5 Calculation of physical quantities

Physical quantities such as charge density n, current density J, and averaged velocity v_{avg} can be obtained by WMC method as follows.

$$n(x,t)=\sum_{k}\sum_{i\in M(x,k)}A_i(t)\,. \tag{4.48}$$

$$J(x,t)=q\sum_{k}\sum_{i\in M(x,k)}\frac{\hbar k_i(t)}{m}A_i(t)\,. \tag{4.49}$$

$$v_{\mathrm{avg}}(x,t)=\sum_{k}\sum_{i\in M(x,k)}\frac{\hbar k_i(t)}{m}A_i(t)\Big/\sum_{k}\sum_{i\in M(x,k)}A_i(t)\,. \tag{4.50}$$

These are an expansion of conventional definition used in the BMC method into WMC method, i.e., affinity is added to the calculation of the physical quantities. The validity of the calculation is discussed in ref. 1.

4.3.6 Treatment of collision term

If explicitly written, Collision term in BTE is as follows:

$$Cf(\mathbf{r},\mathbf{k},t)=\sum_{i}\int d\mathbf{k}'[s_i(\mathbf{k}',\mathbf{k})f(\mathbf{r},\mathbf{k}',t)-s_i(\mathbf{k},\mathbf{k}')f(\mathbf{r},\mathbf{k},t)]\,. \tag{4.51}$$

On the other hand, collision term for WTE is too complicated to simulte in the present computer. However, making use of the nature that WTE is quantum mechanical expansion of BTE, the same collision term as BTE is shown to be safely used [1].

Therefore, in WMC method, collision term is treated in the same way as BMC method.

$$Cf_w(\mathbf{r},\mathbf{k},t)=\sum_{i}\int d\mathbf{k}'[s_i(\mathbf{k}',\mathbf{k})f_w(\mathbf{r},\mathbf{k}',t)-s_i(\mathbf{k},\mathbf{k}')f_w(\mathbf{r},\mathbf{k},t)]\,. \tag{4.52}$$

It is, at least, acceptable approximation, as shown in ref. 1, though this approximation is not trival and we must keep that point in mind. This assumption is also useful to make a clear comparison between classical and quantum transport properties in MOSFETs.

4.4 Quantum transport simulation of Si double-gate (DG) MOSFETs with sub-10nm channel lengths

In this section, DG MOSFETs are simulated using MSWMC simulator developed according to above theory. The effect of quantum transport effects on the device performance in 10 and 6 nm channel DG MOSFET is discussed. In this section, the same device structure shown in Fig. 3.2 is used, but in this chapter, channel thickness T_{Si} is fixed as 3nm and channel length is set as 10 nm or 6 nm. As for scattering processes, to focus the discussion on quantum transport effect, we assumed scattering rate for 3DEG and AP, OP, and impurity scatterings are considered. Due to the strong quantization effect in the ultra-thin body channel as T_{ch} = 3nm, most electrons are distributed in the lowest subbands of each valley, and therefore the lowest and first-higher subbands in each valley are considered in the present simulation.

4.4.1 DG MOSFET with L_{ch} = 10 nm

Fig. 4.8 shows the $I_D - V_G$ characteristics computed for 10 nm channel DG MOSFET. V_D is set as 0.5 V. First, it is found that drain current at high gate voltage is reduced in the quantum approach by about 8% for the present device with L_{ch} = 10 nm, which is mainly due to quantum reflection in the channel as will be discussed later. On the other hand, the subthreshold current is likely to slightly increase in the quantum approach, since the SD direct

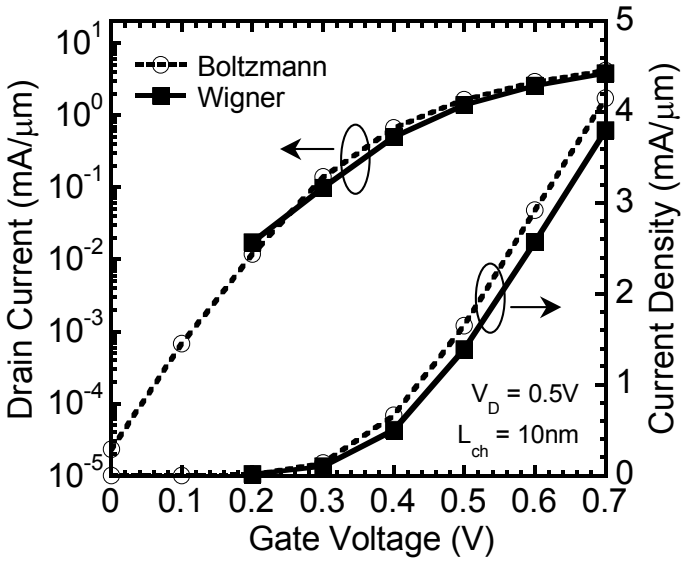

Fig. 4.8 I_D–V_G characteristics computed for DG MOSFET with L_{ch} = 10 nm. The solid and the dashed lines represent the WMC and the classical MC results, respectively. V_D = 0.5 V.

tunneling is included.

Fig. 4.9 shows (a) the lowest subband energy, (b) sheet carrier density and (c) averaged electron velocity profiles computed at V_G = 0.5 V. As shown in Fig. 4.9 (b), electron density in the channel exhibits no significant difference between the quantum and classical approaches because of the on-state. However, carrier depletion region in the source and drain is expanded due to non-local quantum repulsive force from the channel potential [3] as seen in the inset of Fig. 4.9 (b). Here, note that the averaged electron velocity decreases around the source-end bottleneck barrier by including quantum transport effects as shown in Fig. 4.9 (c). This is considered due to quantum reflection caused by the steep potential drop inside the channel as shown in Fig. 4.9 (a).

To confirm that the quantum reflection actually happens, we plot distribution functions in phase-space computed by using the classical MC and the WMC methods in Figs. 4.10 (a) and (b), respectively, where contrast represents the number of electrons present in a cell of the phase space. Distinct oscillations in the Wigner distribution function are observed, while they are not present in the Boltzmann distribution function. In particular, oscillations are visible not only in $k > 0$ region but also in $k < 0$ region of the channel, which is the signature of quantum reflection [1]. They occur in the region where the potential abruptly drops between the barrier top and the drain-end of the channel. Accordingly, the quantum reflection indeed decreases the source-end electron velocity and the drain current at on-state compared to the classical one, as shown in Fig. 4.8.

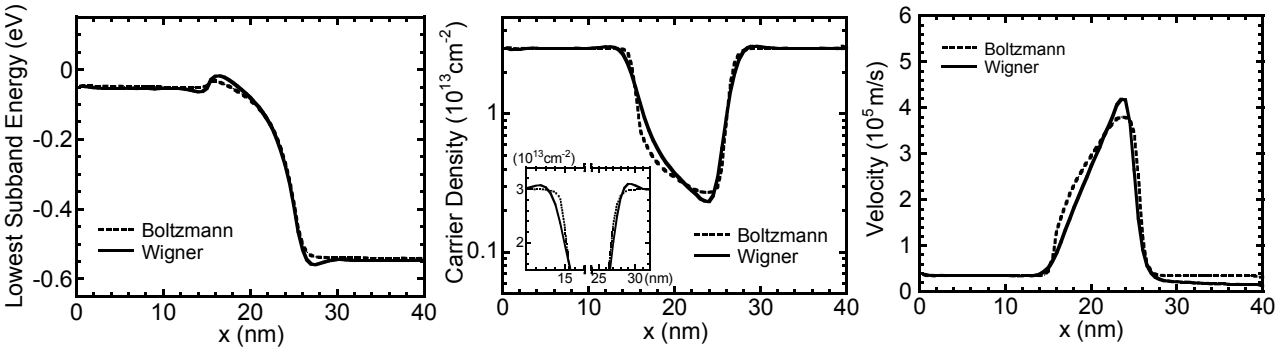

Fig. 4.9 (a) Lowest subband energy, (b) sheet carrier density and (c) averaged electron velocity profiles for L_{ch} = 10 nm. V_G = 0.5 V and V_D = 0.5 V.

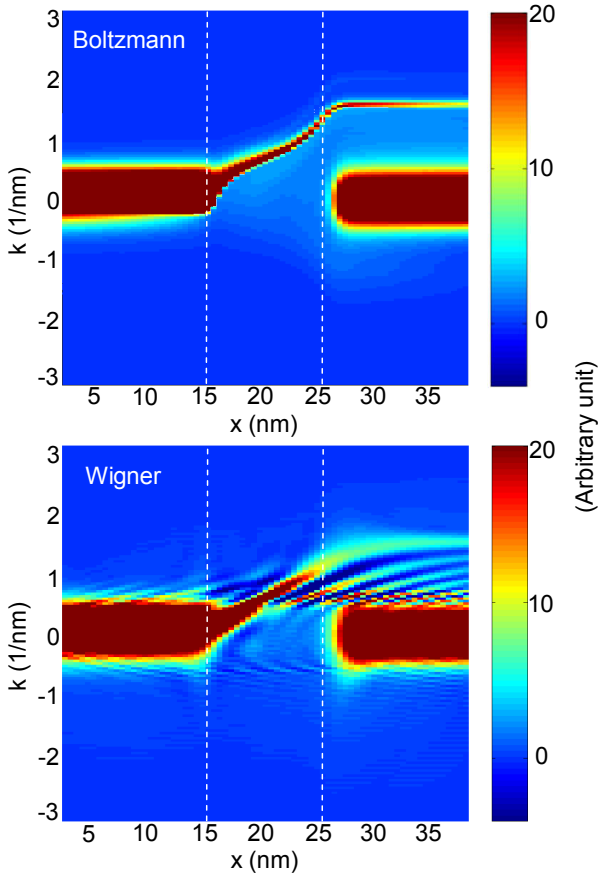

Fig. 4.10 Boltzmann (upper) and Wigner (lower) distribution funcitons for L_{ch} = 10 nm. V_G = 0.5 V and V_D = 0.5 V.

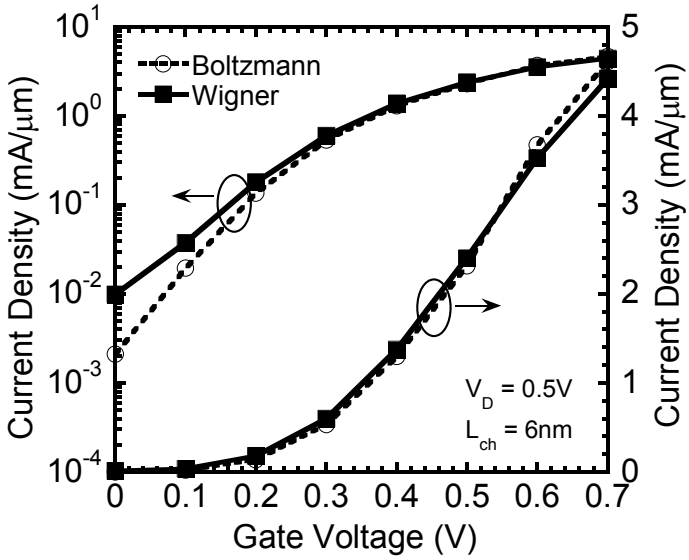

Fig. 4.11 I_D–V_G characteristics computed for DG MOSFET with L_{ch} = 6 nm. The solid and the dashed lines represent the WMC and the classical MC results, respectively. V_D = 0.5 V.

4.4.2 DG MOSFET with L_{ch} = 6 nm

We further simulated an ultimately scaled device with L_{ch} = 6 nm. Fig. 4.11 shows the I_D– V_G characteristics, where the subthreshold property is successfully calculated until V_G = 0 V with the WMC method. First, the SS value obviously increases in the quantum approach, since SD direct tunneling is included. On the other hand, the quantum current at high gate voltage has more or less the same value as the classical one. To understand this behavior, the distribution functions at V_G = 0.5 V are calculated as shown in Fig. 4.12. It is found that quantum interference pattern caused by the quantum reflection is less observable in Fig. 4.12 (b). This implies that quantum

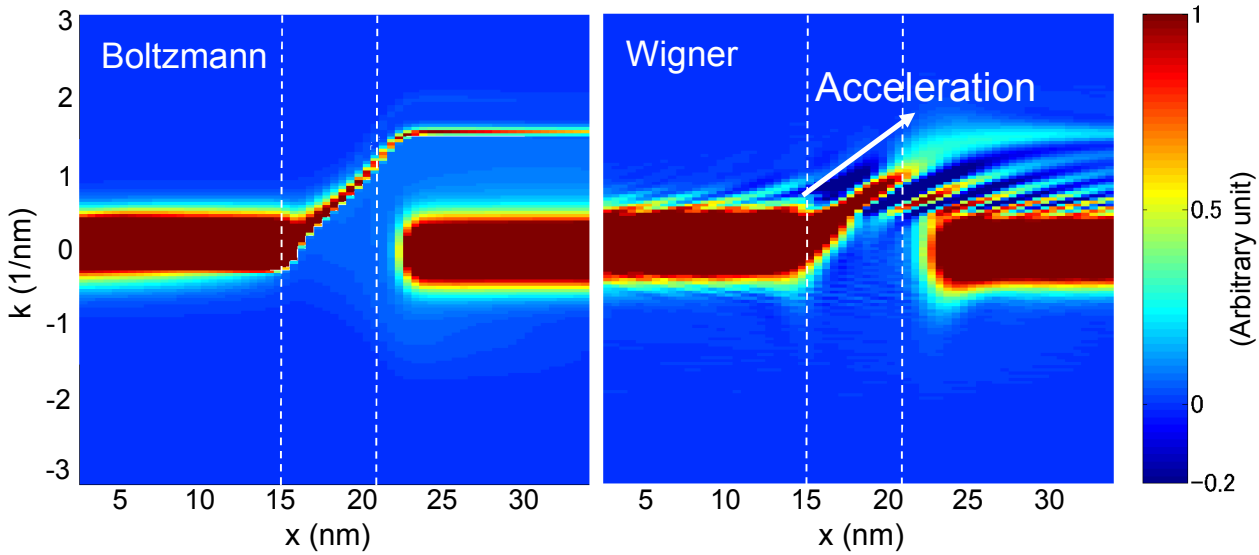

Fig. 4.12 Boltzmann (left) and Wigner (right) distribution funcitons computed for DG MOSFET with L_{ch} = 6 nm. V_D = 0.5 V. V_G = 0.5 V and V_D = 0.5 V.

reflection is suppressed in such ultimately scaled device as L_{ch} = 6 nm.

Then, we present the transport properties at off-state. Fig. 4.13 shows (a) the lowest subband energy, (b) sheet

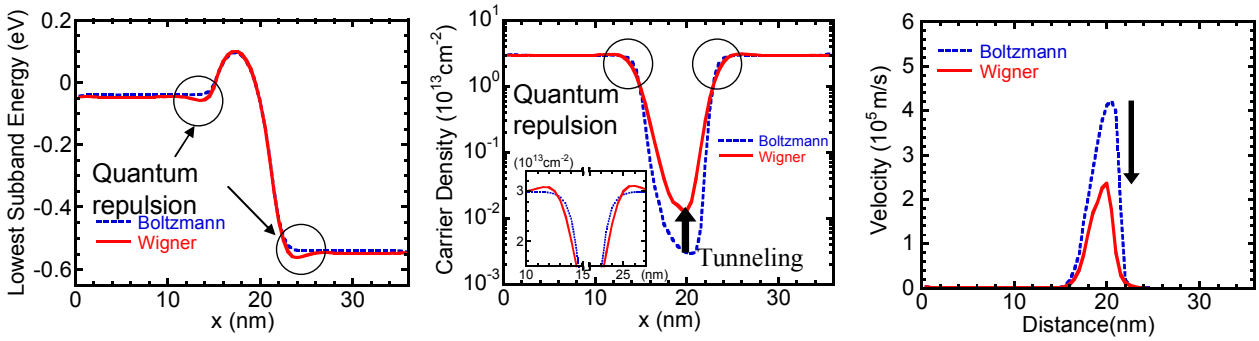

Fig. 4.13 (a) Lowest subband energy, (b) sheet carrier density and (c) averaged electron velocity profiles for L_{ch} = 10 nm. V_G = 0.1 V and V_D = 0.5 V.

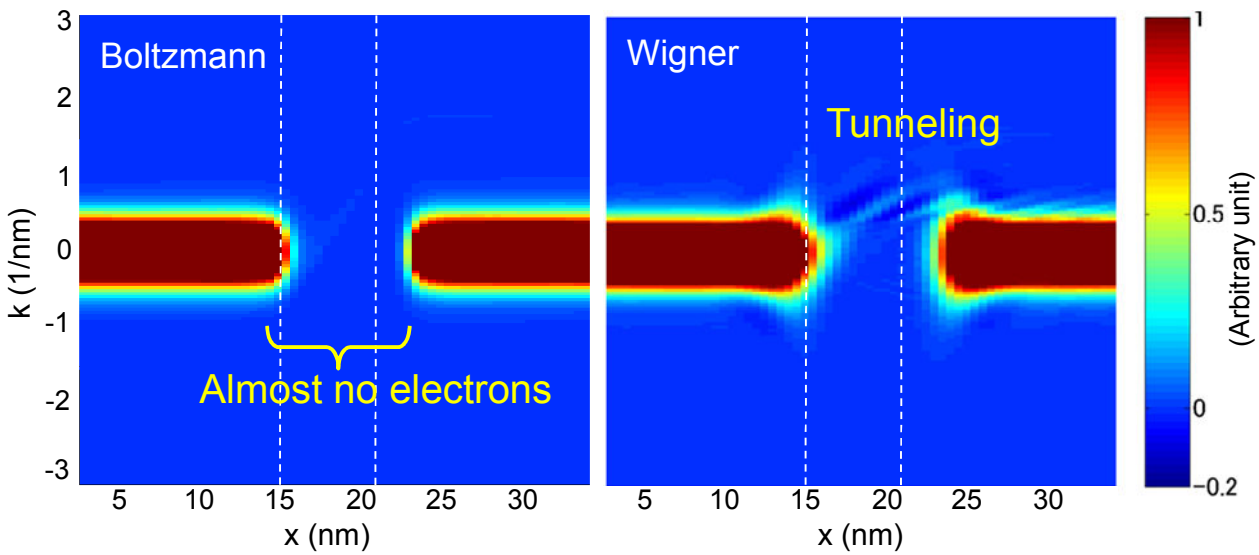

Fig. 4.14 Boltzmann (left) and Wigner (right) distribution funcitons computed for DG MOSFET with L_{ch} = 6 nm. V_D = 0.5 V. V_G = 0.1 V and V_D = 0.5 V.

carrier density and (c) averaged electron velocity profiles computed at V_G = 0.1 V, and Fig. 4.14 the corresponding distribution functions. From Fig. 4.13 (b), the electron density in the channel obviously increases due to the SD tunneling effect, and as a result the averaged electron velocity significantly decreases as in Fig. 4.13 (c), because tunneling electrons are not accelerated during the tunneling process. Such tunneling electron trajectory appears in the Wigner distribution function as shown in Fig. 4.14 (b). Although weak interference pattern is visible in the channel region, an electron trajectory flowing into the drain with acceleration, which is visible in 4.12 (b), is not observed.

4.4.3 Quantum reflection and its channel length dependence

Then, we actually calculated the corresponding transmission probabilities for L_{ch} = 6 nm and 10 nm by using a transfer-matrix method as shown in Fig.4.15, where the lowest subband profile resulting from the WMC simulation is substituted into Schrödinger equation. Transfer matrix method is described in appendix A. In Fig.

4.15, the energy reference (E = 0) corresponds to the bottom of the bottleneck barrier as indicated in the inset. It is found that even if the kinetic energy becomes larger than energy top of the bottleneck barrier, the transmission probabilities exhibit less than one, and several 10% of electrons are reflected toward the source for both channel lengths. This is termed quantum reflection. Here, it should be noted that the transmission probability above the energy top of the barrier increases with decreasing the channel length, which indicates that the quantum reflection is receded in the 6 nm device as expected above. Consequently, the reduction in the drain current due to quantum reflection is less pronounced in the present 6 nm device.

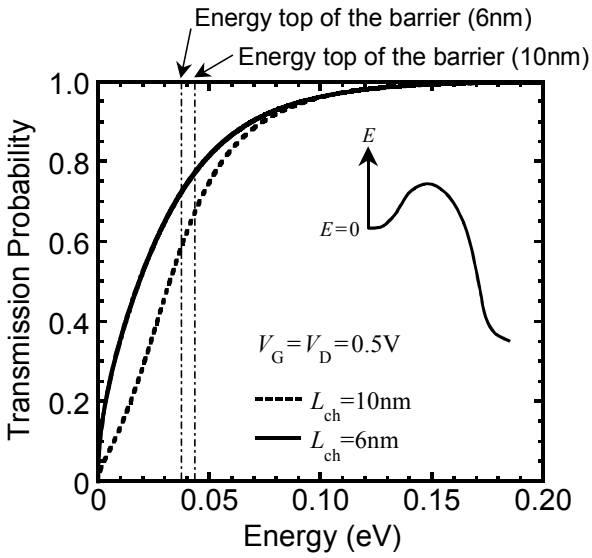

Fig. 4.15 Transmission probability computed for DG MOSFETs with channel length of 10 nm and 6 nm.

4.4.4 Temperature dependence of I_D-V_G characteristics

Next, temperature dependence of I_D-V_G characteristics is discussed. As thermal equilibrium distribution of electrons become wider, subthreshold slope is anticipated to be degraded, whereas phonon scattering has strong temperature dependence, thus on current are also anticipated to be worsen.

Figure 4.16 shows the temperature dependence of I_D-V_G characteristics for 10nm channel. As is anticipated, increase in temperature results in the drastic degradation of subthreshold slope. On the other hand, on current are also degraded because of increased phonon scattering.

It is worth noting that on-current density decrease due to temperature increase (by comparing Boltzmann-300K with Boltzmann 400K) is smaller than that due to quantum reflection (by comparing Boltzmann-300K with Wigner 300K). Therefore, impact of quantum reflection on the on-state current reduction is more significant than 100 K increase in temperature.

4.4.5 Demonstration of quantum-classical transition due to scatterings

Here, we examine how the carrier scattering influences quantum reflection. To this end, we increased the scattering rate by ten times, which emulates a diffusive transport such as in longer channel devices, etc. Fig. 4.17

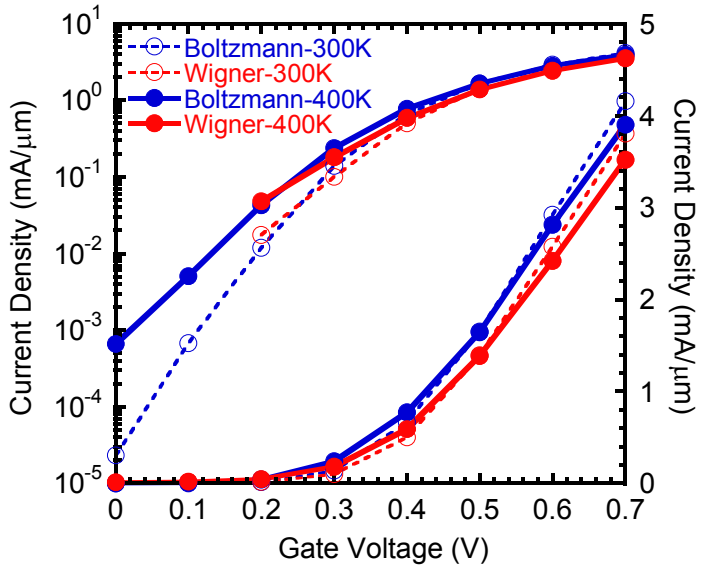

Fig. 4.16 Temperature dependence of I_D–V_G characteristics computed for DG MOSFET with L_{ch} = 10 nm. The solid and the dashed lines represent the results for T = 400 K and 300 K, respectively. V_D = 0.5 V.

shows the I_D – V_G characteristics computed using increased scattering rate (scattering × 10), where the previous results with standard scattering rate are also plotted for comparison.

It is found that current reduction at high gate voltage becomes less significant by increasing the scattering rate, and hence the quantum I_D – V_G curve approaches the classical one. This means that quantum reflection vanishes and carrier transport is varied from quantum to classical behaviors under the diffusive transport. Such

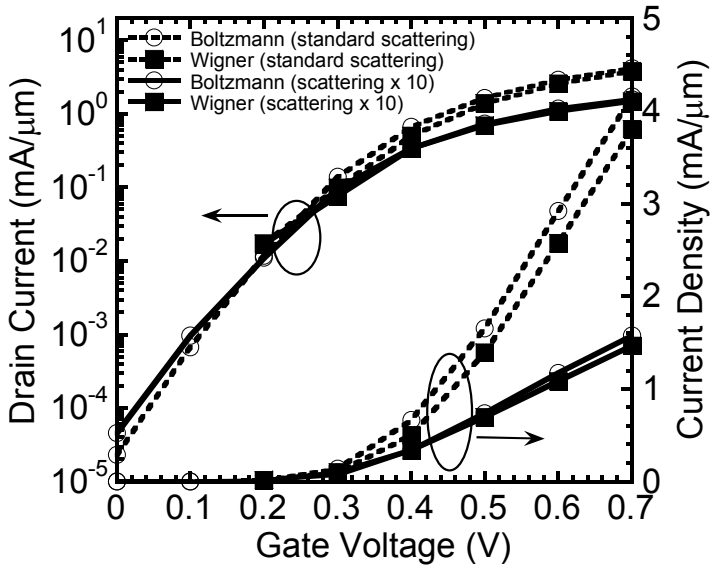

Fig. 4.17 Variations in I_D–V_G characteristics due to scattering rates computed for DG MOSFET with L_{ch} = 10 nm. The solid and the dashed lines represent the results for scattering rates increased by 10 times and standard scattering rates, respectively. V_D = 0.5 V. Scattering rates are intentionally increased by 10 times.

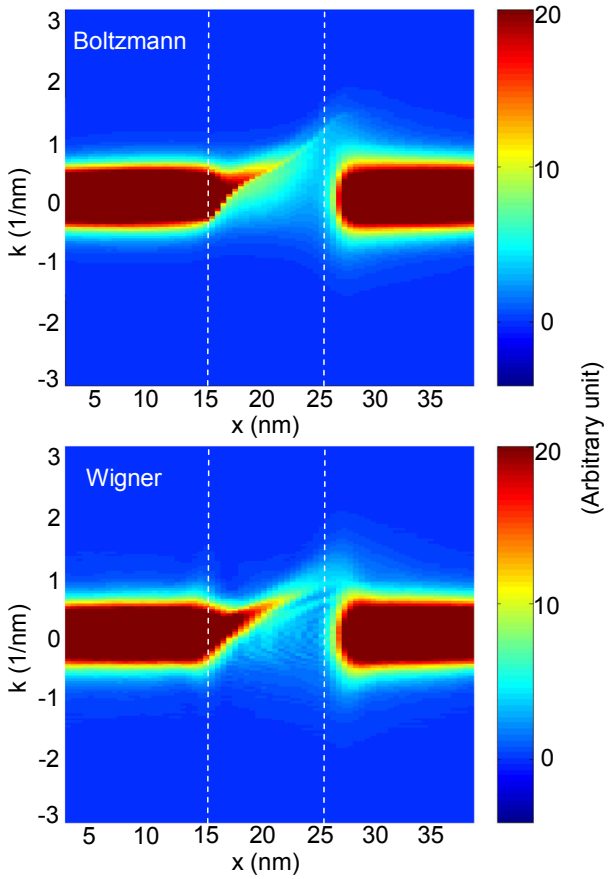

Fig. 4.18 Boltzmann (left) and Wigner (right) distribution funcitons computed for DG MOSFET with L_{ch} = 10 nm. V_D = 0.5 V. V_G = 0.5 V and V_D = 0.5 V. Scattering rates are intentionally increased by 10 times.

quantum-classical transition is more clearly observed in the distribution functions as shown in Fig. 4.18. It is shown that quantum interference pattern in the Wigner distribution function completely disappears and classical distribution function is reproduced.

As presented above, the WMC method can describe quantum-classical transition of carrier transport. Furthermore, by limiting our discussion to the classical simulation, the subthreshold slope (SS) is hardly changed with scattering rate as shown in Fig. 4.17. This is because the subthreshold current is governed by thermally diffusive injection of carriers from the source in the classical limit [11].

4.4.6 Comparison between NEGF and MSWMC

As in the case in subsection 4.1.2, NEGF method and WMC method are compared and it is shown that these methods are consistent within the effective mass approximation.

Fig. 4.19 shows relation of coordinate in NEGF and WTE. Also, Fig. 4.20 shows that there are some differences between MC solution and NEGF method, such as boundary condition.

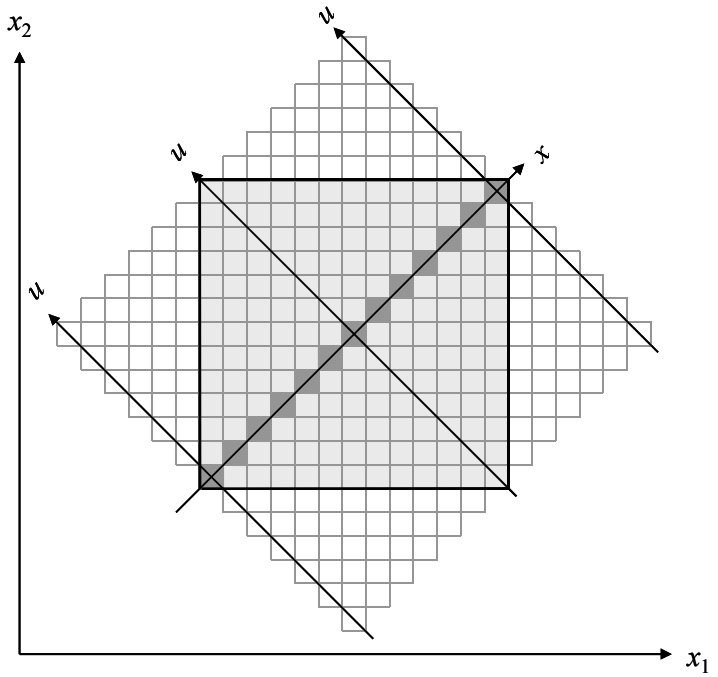

$$\rho(x_1, x_2) \Leftrightarrow f_w(x, k, t)$$

$$f_w(x,k) = \frac{1}{2\pi}\int du\, e^{-iku}\rho\left(x+\frac{u}{2}, x-\frac{u}{2}\right)$$

$$\begin{cases} x = \dfrac{x_1+x_2}{2} \\ u = x_1 - x_2 \end{cases} \quad \begin{cases} x_1 = x + \dfrac{u}{2} \\ x_2 = x - \dfrac{u}{2} \end{cases}$$

Fig. 4.19 Schematic view of the relation of the coordinates x_1, x_2, x, u. Relation between Wigner function and density matrix are also shown.

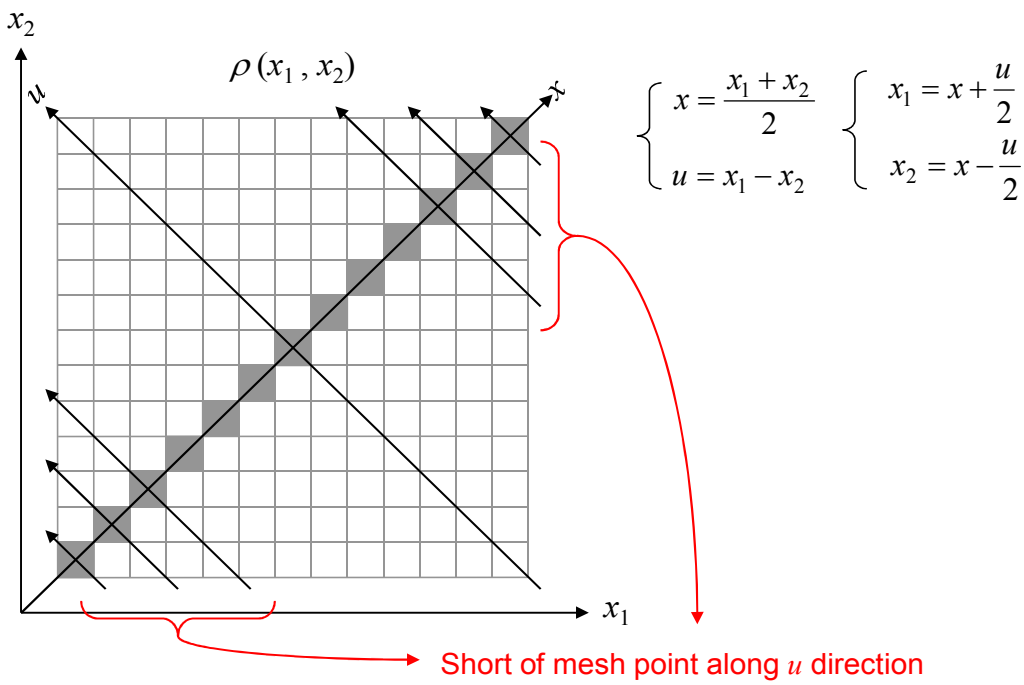

$$\begin{cases} x = \dfrac{x_1+x_2}{2} \\ u = x_1 - x_2 \end{cases} \quad \begin{cases} x_1 = x + \dfrac{u}{2} \\ x_2 = x - \dfrac{u}{2} \end{cases}$$

Fig. 4.20 Schematic view of density matrix if $G^<$ is obtained from density function ρ. Sampling mesh point along u direction is insufficient except for the center of the device.

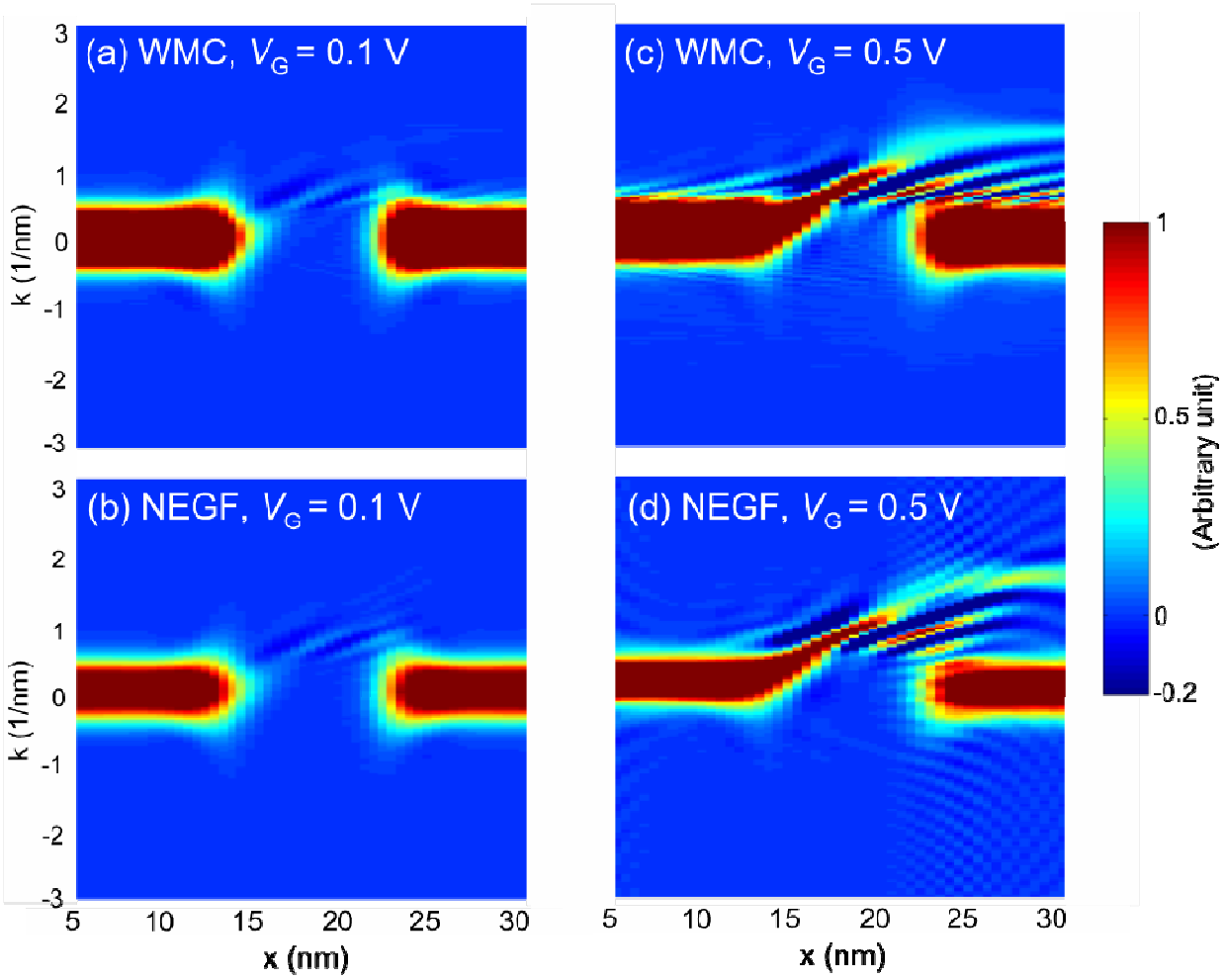

Fig. 4.21 Comparison of Wigner distribution functions calculated by (a), (c) WMC method and (b), (d) NEGF method.

As in Fig. 4.19, WDF is defined as the Fourier transform of the density matrix by the relative coordinate, where density matrix is the quantity which describes the non-local correlation of the wave functions. Diagonal terms describe probability density distribution along the x direction. Density matrix can also be obtained by the correlation Green's function $G^<$, but in that case, mesh point of coefficient u is insufficient as in Fig. 4.20, and therefore WDF is distorted near the source or drain boundary because of the insufficient mesh number.

Here, direct comparison of I_D–V_G characteristics is not conducted, since such a study is already found in ref. [1]. Instead, WDF obtained by NEGF by integration of $G^<$ and that obtained directly by WMC method are compared as in Fig. 4.21, which well coincides in the channel region.

4.5 Summary

A quantum-mechanics-based WMC simulator is developed for rigorously incorporating quantum transport effect along the source-to-drain direction. WMC method solves WTE using MC algorithm and incorporates not only scattering effects but also quantum transport effects more precisely. Thus, the method has the ability suitable

for the simulation of integrated nanoscale devices. This study is the first successful attempt of WMC simulation in Asia.

The WMC quantum simulation method is extended to multi-subband (MS) simulation and effects of quantum transport effects in silicon DG MOSFETs with channel length of less than 10 nm are investigated. As a result, we have demonstrated that the quantum reflection makes significant differences in the microscopic features of electron transport and can even reduce the drain current at on-state, but it does not necessarily produce drastic change in the macroscopic properties including the drain current. On the other hand, SD tunneling is shown to play a crucial role in the subthreshold properties of scaled MOSFETs with channel lengths of less than 6 nm. We have also shown that the WMC approach has the ability to describe quantum-classical transition of carrier transport in the diffusive transport regime dominated by scattering.

References

[1] D. Querlioz and P. Dollfus, *The Wigner Monte Carlo Method for Nanoelectronic Devices* (Wiley, New York, 2010.)

[2] H.-N. Nguyen, D. Querlioz, S. G.-Retailleau, and P. Dollfus, IEEE Trans. Electron Devices **58**, 798 (2011).

[3] S. Koba, R. Aoyagi, and H. Tsuchiya, J. Appl. Phys. **108**, 064504 (2010).

[4] E. Wigner, Phys. Rev. **40**, 749, (1932).

[5] W. R. Frensley, Phys. Rev. B. **36**, 1570 (1987).

[6] H. Tsuchiya and T. Miyoshi, J. App. Phys. **83**, 2574 (1998).

[7] H. Tsuchiya and U. Ravaioli, J. Appl. Phys. **89**, 4023 (2001).

[8] R. K. Mains and G. I. Haddad, J. Appl. Phys. **64**, 5041, (1988).

[9] H. Tsuchiya, M. Ogawa, and T. Miyoshi, IEEE Trans. Electron Devices **38**, 1246 (1991).

[10] P. D. Yoder, M. Grupen, and R. K. Smith, IEEE Trans. Electron Devices **57**, 3265 (2010).

[11] Y. Yamada, H. Tsuchiya, and M. Ogawa, IEEE Trans. Electron Devices **56**,1396 (2009).

[12] S. Barraud, J. Appl. Phys. **106**, 063714 (2009).

[13] S. Barraud, J. Appl. Phys. **110**, 093710 (2011).

[14] J. R. Barker and D. K. Ferry, Phys. Rev. Lett. **42**, 1779 (1979).

5. Performance prediction of III-V channel DG MOSFETs with Wigner Monte Carlo simulator

In this chapter, the features of III–V materials and expectations for them are discussed, and the impact of SD direct tunneling on $In_{0.53}Ga_{0.47}As$ and InP MOSFETs is investigated using a quantum Wigner Monte Carlo simulation. The difference in the impact in $In_{0.53}Ga_{0.47}As$ and InP are discussed and also compared with Si. As a result, it was found that subthreshold current increase due to SD direct tunneling becomes more remarkable in $In_{0.53}Ga_{0.47}As$ MOSFETs owing to its lower effective mass. In addition, the critical channel length for which a drastic increase in subthreshold current occurs due to SD direct tunneling was found to be about 20 nm for both $In_{0.53}Ga_{0.47}As$ and InP MOSFETs. Since this value is significantly larger than that for Si MOSFET, SD direct tunneling can be a major obstacle to downscale III-V MOSFETs into $L_{ch} < 20$ nm. Hence, to go beyond the end of the roadmap, we will need a material selection for suppressing SD direct tunneling.

5.1 Features of III-V materials and its application to the MOSFETs

As discussed in chapter 1, III-V compound semiconductors are expected to replace Si as the channel material in n-channel MOSFETs, and the high performance of MOSFETs with InGaAs [1–5] and InP [6] channels has already been experimentally demonstrated. However, due to the lower effective mass and enhanced quasi-ballistic transport associated with III-V semiconductors, their use in MOSFETs may lead to more serious quantum transport effects along the channel direction, such as quantum reflection and tunneling. According to previous studies on Si MOSFETs, they are considered to suffer from SD direct tunneling for channel lengths smaller than 6–8 nm [7–11]. Furthermore, quantum reflection due to a steep potential variation inside the channel will lead to a reduction in the on-state drain current [12–15]. Since III-V compound semiconductors have a lower transport effective mass than Si, subthreshold current properties of III-V MOSFETs may be more crucially degraded by SD direct tunneling because of increased tunneling probability.

As shown in Table I, $In_{0.53}Ga_{0.47}As$ has a substantially lower effective mass in the Γ valley than that for InP, whereas it has a larger nonparabolicity in the Γ valley. A lower transport mass leads to an increased SD direct tunneling, and can lead to further degraded subthreshold current properties. Accordingly, $In_{0.53}Ga_{0.47}As$, which is actively researched as a post-Si channel material [16–19], might suffer from SD direct tunneling more significantly than InP. In this paper, we investigate the influence of SD direct tunneling in $In_{0.53}Ga_{0.47}As$ MOSFETs by making a comparison with InP MOSFETs and also with Si MOSFETs, based on WMC simulation [12–15,20], in which both quantum transport and carrier scattering effects can be fully incorporated. We also discuss the role of channel potential profile in suppressing SD direct tunneling by changing gate oxide thickness.

TABLE 5.1: Band structure parameters used in the simulation of InGaAs and InP MOSFETs, where we used bulk band parameters for both channel materials. The values for Si are also included for comparison.

		Si	$In_{0.53}Ga_{0.47}As$	InP
Mass (Γ)		–	0.046	0.082
Mass (X)	m_t	0.19	0.251	0.273
	m_l	0.92	2.852	1.321
Mass (L)	m_t	0.126	0.125	0.153
	m_l	1.634	1.552	1.878
Nonparabolicity α (eV^{-1})		0.5 (X) 0.3 (L)	1.18 (Γ) 0.43 (L) 0.33 (X)	0.61 (Γ) 0.49 (L) 0.12 (X)
ΔE_{XL}		1.049	–	–
$\Delta E_{\Gamma L}$ / $\Delta E_{\Gamma X}$		–	0.723/1.062	0.832/1.492
Band gap (eV)		1.12	0.86	1.34
Permittivity ε_r		11.9	14.1	12.6

Fig. 5.1 shows conduction band structures of bulk Si and bulk III–V materials. Si have six equivalent conduction bottoms near X points, and also have four L valleys at 1.049 eV above X valleys. Note that L valleys exist in the edge of the Brillouin zone, hence, two collinear ellipsoidal hemispheres correspond to one L valley. The actual number of L valleys is 4. On the other hand, III–V materials have one conduction bottom at Γ point, and four L valleys and six X valleys exist above the Γ valley. X valleys are higher than L valleys.

In Si, ΔE_{XL}, i.e., energy gap between X valleys and L valleys, is sufficiently larger than the supply voltage considered in this study, as shown in Table 5.1. That's why only X valleys are considered in chapter 2 and 3. In the same manner, in III–V channel MOSFETs, electrons are never distributed in the X valleys with sufficiently larger

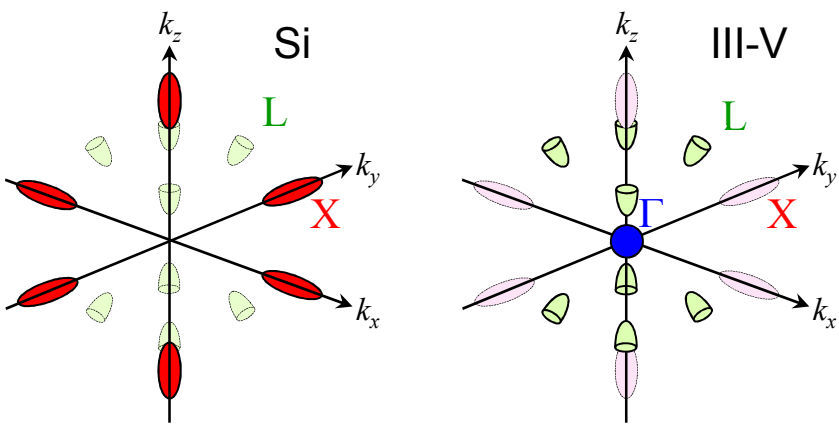

Fig. 5.1 Conduction band structures of bulk Si and bulk III–V materials.

energy gap $\Delta E_{\Gamma X}$. Therefore, in the following simulations of III–V channel MOSFETs, Γ and L valleys are considered.

5.2 Device structures and simulation methods

5.2.1 Device structures

Figure 5.2 shows the device structure used in the simulation, where a DG structure was employed with a channel thickness of 5 nm. A SiO_2 gate oxide thickness (T_{OX}) used was 0.5 nm, unless otherwise stated. The channel, source and drain materials were $In_{0.53}Ga_{0.47}As$ or InP, and the band parameters used in the simulation are shown in Table 5.1, where we used bulk band parameters for both materials. Therefore, the present simulation might overestimate the influence of SD direct tunneling in ultrathin-body III-V MOSFETs, because actual effective mass increases owing to quantum confinement [21–27]. Here, the values of Si are also included for comparison. The source and drain donor concentrations used were 2×10^{19} cm^{-3} [28–31], and the channel was undoped, where we assumed that the donor distribution abruptly changes at source-channel and drain-channel junctions. L_{ch} was varied from 5 to 40 nm. The electrical characteristics were calculated using the WMC device simulator and also using the Boltzmann MC (BMC) simulator [32], in both of which electron transport is simulated along the channel direction x for each valley and each quantized subband obtained with the Schrödinger-Poisson solver. Hence, we can assess quantum transport effects including SD direct tunneling by comparing the two MC results. Scattering processes considered in this study are acoustic phonon, non-polar and polar optical phonon, and impurity scatterings [28,30,31].

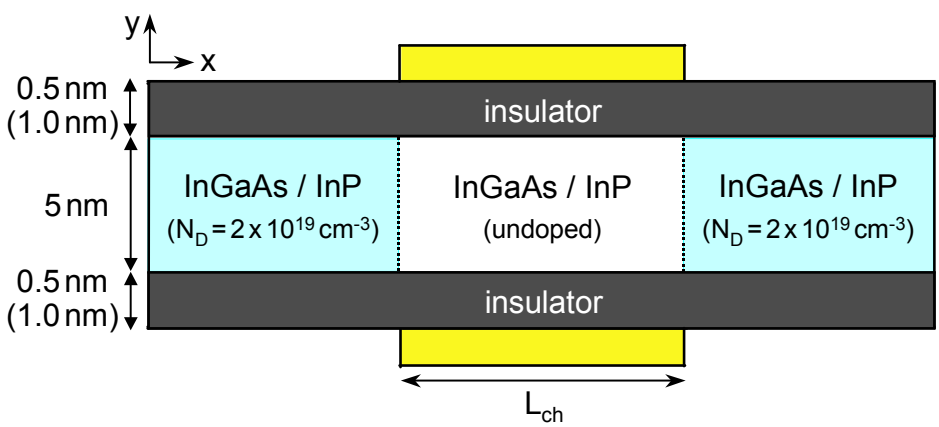

Fig. 5.2 Device structure used in the simulation, where a double-gate structure was employed with a channel thickness of 5 nm. The SiO_2 gate oxide thickness (T_{ox}) was given as 0.5 nm, unless otherwise stated. The channel, source and drain materials were $In_{0.53}Ga_{0.47}As$ or InP.

TABLE 5.2: Scattering parameters for InP and $In_{0.53}Ga_{0.47}As$.

		InP	$In_{0.53}Ga_{0.47}As$
Crystal density ρ (kg/m^3)		4810.0	5522.7
Sound velociy v (m/s)		5130.0	4731.2
Optical permittivity ε_∞ (ε_0)		9.61	11.89
Acoustic phonon deformation potential (eV)		5.0/5.0 (Γ/L)	5.4/5.4 (Γ/L)
Polar optical phonon energy (meV)		42.4	32.56
Nonpolar ineleastic phonon deformation potential (eV/cm)	Γ – L	5.06×10^8	5.43×10^8
	L – L	5.75×10^8	6.15×10^8
Nonpolar ineleastic phonon energy (meV)	Γ – L	22.15	19.9
	L – L	24.27	21.9

5.2.2 Scattering treatment for III-V MOSFETs

In the compound semiconductors, longitudinal lattice vibration arises polarization wave due to ion bonding, and the polarization wave interact with carriers, resulting in polar phonon scatterings. Polar phonon scattering consists of piezoelectric scattering and polar optical phonon (POP) scatterings, and POP scattering significantly affects device performance of III-V MOSFETs. Therefore, treatment of POP scattering is essential.

In this chapter, to focus on the impact of quantum transport effects, 3D treatment of scattering rate is utilized since scattering treatment hardly affects sub-threshold characteristics.

5.2.3 Polar optical phonon scatterings

Scattering rate of POP scattering is expressed as

$$W(E)=\frac{e^2\omega_0}{8\pi\varepsilon_\mathrm{p}}\frac{k}{E_\mathbf{k}}\left(n(\omega_0)+\frac{1}{2}\mp\frac{1}{2}\right)\ln\left(\frac{q_\mathrm{max}}{q_\mathrm{min}}\right), \tag{5.1}$$

where q_max and q_min are given as

$$q_\mathrm{min}=k\left|1-\sqrt{1\pm\frac{\hbar\omega_0}{E_\mathbf{k}}}\right|, \tag{5.2}$$

$$q_\mathrm{max}=k\left(1+\sqrt{1\pm\frac{\hbar\omega_0}{E_\mathbf{k}}}\right). \tag{5.3}$$

In non-polar phonon scatterings such as AP and non-polar OP, scattering rate is proportional to the density-of-states (DOS). In contrast, POP scattering rate isn't proportional to the DOS and scattering rate decreases as electron kinetic energy becomes higher. Also, POP scattering is an anisotropic process, and its scattering angle is given as

$$\cos\theta = \frac{1+f-(1+2f)^r}{f}, \tag{5.4}$$

where f is dependent on the energy before and after the scattering $E_{\mathbf{k}}$ and $E'_{\mathbf{k}}$ and expressed as

$$f = \frac{2\sqrt{E_{\mathbf{k}}E'_{\mathbf{k}}}}{(\sqrt{E_{\mathbf{k}}}-\sqrt{E'_{\mathbf{k}}})^2}. \tag{5.5}$$

r stands for random number valued from 0 to 1.

Also, scattering parameters for InGaAs and InP are shown in Table 5.2. Intervalley POP scattering has negligible effect, so POP scattering is treated as intravalley scattering process.

5.3 Electrical Characteristics

5.3.1 Characteristics for InP MOSFETs

Figure 5.3 shows the drain current versus gate voltage (I_D-V_G) characteristics of InP MOSFET computed at V_D = 0.5 V for L_{ch} = (a) 30, (b) 15, and (c) 10 nm, where the WMC and BMC results are plotted as solid and dashed lines, respectively. It can be seen that both sets of MC results are almost identical for L_{ch} = 30 nm. However, as the channel length becomes shorter than 15 nm, the subthreshold current determined by the WMC simulation rapidly becomes larger than that determined by BMC simulation. This is due to the increased effect of SD direct tunneling, as will be shown later based on phase-space distribution functions. It should also be noted that the drain current at high gate voltages is almost the same for both simulations, regardless of channel length, indicating that quantum reflection has a negligible effect on the on-state drive current.

To further elucidate the effects of SD direct tunneling and quantum reflection, the distribution functions in phase space were computed using both the WMC and BMC approaches. Figures 5.4 and 5.5 show the computed distribution functions for a gate voltage corresponding to a threshold voltage V_{th} and an on-state voltage V_{on},

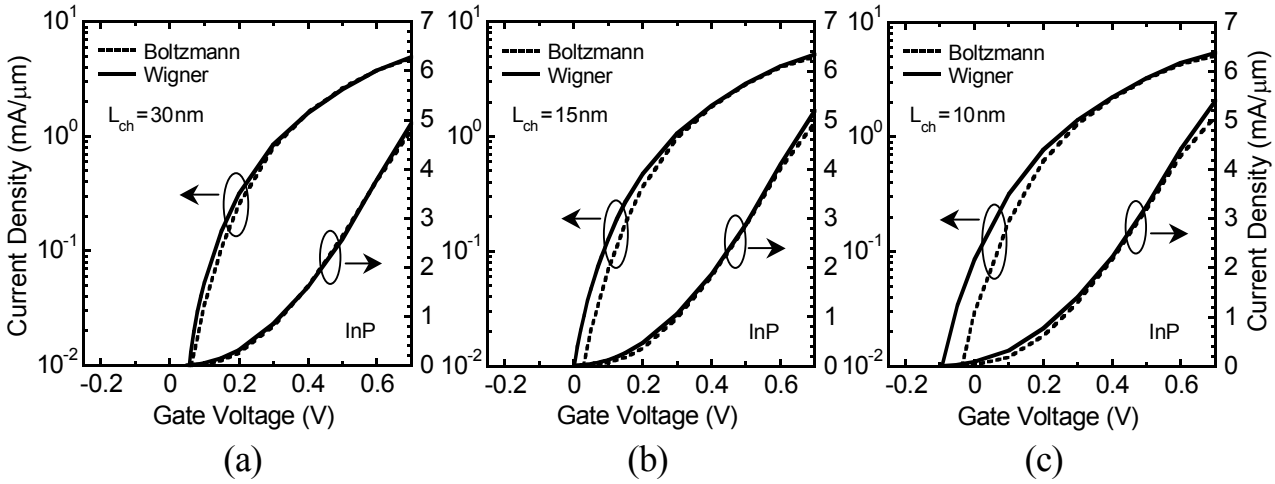

Fig. 5.3 I_D - V_G characteristics of InP MOSFETs computed at V_D = 0.5 V for L_{ch} = (a) 30, (b) 15, and (c) 10 nm, where the WMC and BMC results are plotted as solid and dashed lines, respectively.

respectively, for L_{ch} = (a) 30 and (b) 10 nm. Here, V_{th} and V_{on} are defined as the gate voltages corresponding to I_D = 0.03 mA/μm and 3 mA/μm, respectively, as determined by the BMC simulation. Specifically, V_{th} = 0.1 V for L_{ch} = 30 nm and 0 V for L_{ch} = 10 nm, whereas V_{on} = 0.5 V for both channel lengths. The contrast in the lower panels of the figures indicates the number of electrons present in each cell the in phase space. The upper panels show the spatial distributions of the lowest subband energy in the Γ valley and the total sheet electron density. From Fig. 5.4 (a), it is found that the two distribution functions are markedly similar not only in the source and drain regions but also in the channel region, indicating that SD direct tunneling is nearly negligible for L_{ch} = 30 nm. This is also confirmed by the sheet electron density distributions, i.e., both MC simulations indicate almost the same electron densities inside the channel. On the other hand, for the shorter channel device with L_{ch} = 10 nm, an interference pattern is observed in the Wigner distribution function inside the channel region, as shown in Fig. 5.4(b). Since this is known to be a signature of tunneling, it indicates that SD direct tunneling actually occurs in this short channel device. This is also confirmed by the significant increase in the channel sheet density observed in the WMC results, even though the lowest-subband energy profiles are identical for both MC simulations.

As seen in Fig. 5.5, for a gate voltage of V_{on}, there are only slight differences between the WMC and BMC distribution functions for either channel length. In particular, in Fig. 5.5 (a), the two distribution functions are almost identical. In addition, the sheet electron density distributions calculated using the two MC methods are also almost identical, regardless of the channel length. This is because the main current is governed by thermal electron emission at the source-channel junction, which is a classical mechanism, and thus the drain current for a gate voltage of V_{on} is basically determined by classical transport. In other words, SD direct tunneling is insignificant in this case. In the Wigner distribution function shown in Fig. 5.5 (b), an interference pattern appears inside the channel, and this is mainly associated with quantum reflection. However, unlike the case for Si MOSFETs, the intensity of this pattern is almost negligible compared to that for the main electron flow path. This indicates that quantum reflection is weak and leads to almost no reduction in the on-state drain current in the simulated InP MOSFET. One possible reason for the weak quantum reflection effect may be that there is a gradual potential variation at the drain end of the channel, originating from the low donor concentration in the drain region. Quantum reflection occurs most effectively for a high potential barrier with a steep gradient. As a result, almost the same on-current was obtained even for L_{ch} = 10 nm using the WMC and BMC approaches, as seen in Fig. 5.3(c).

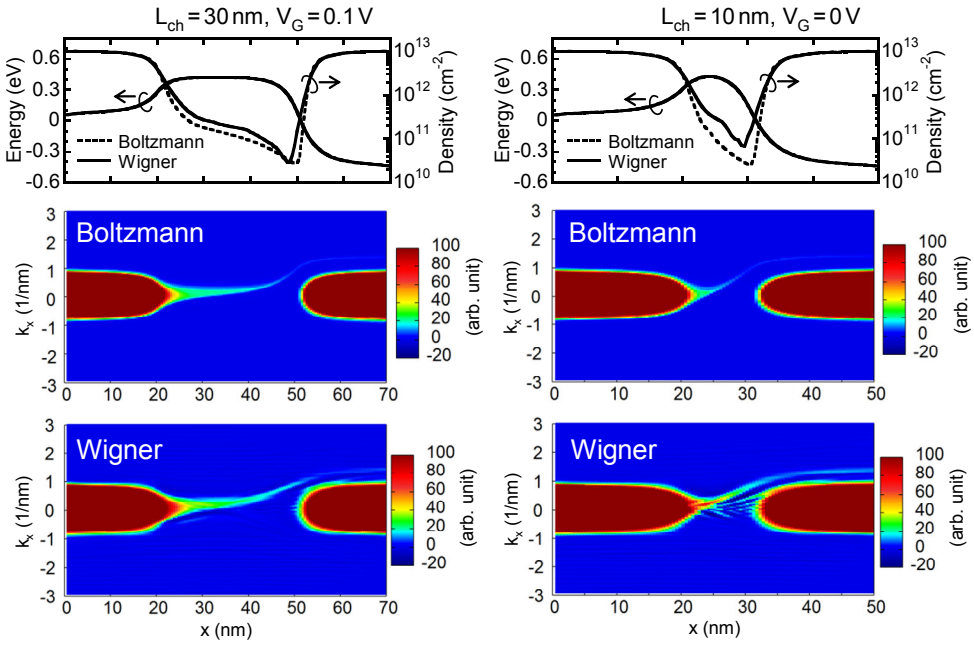

(a) (b)

Fig. 5.4 Computed phase-space distribution functions of InP MOSFETs for L_{ch} = (a) 30 and (b) 10 nm at a threshold gate voltage V_{th}, defined as the gate voltage corresponding to I_D = 0.03 mA/μm from the BMC simulations. The upper panels show the spatial distributions of the lowest-subband energy in the Γ valley and the total sheet electron density.

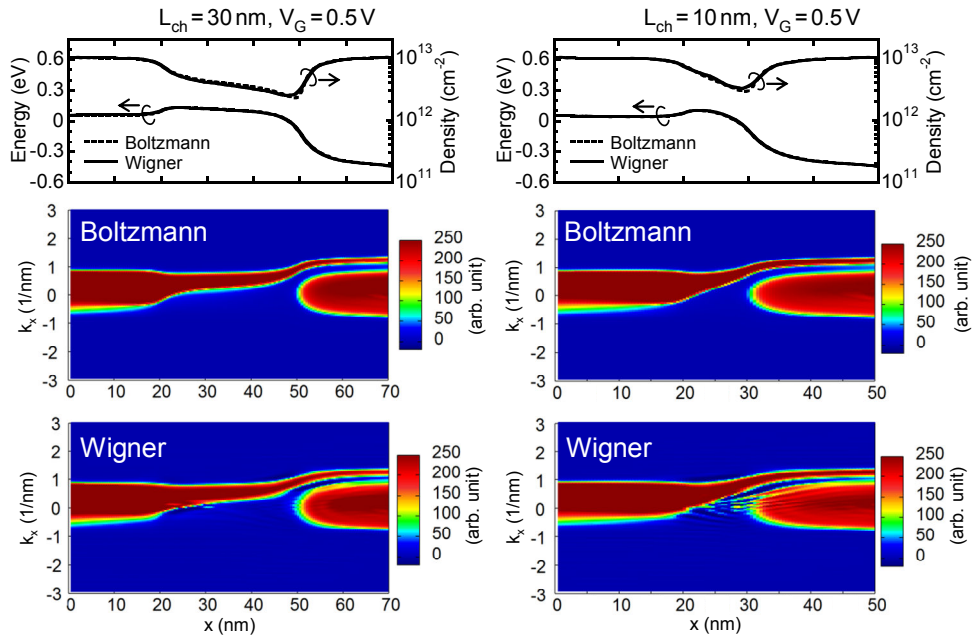

(a) (b)

Fig. 5.5 Computed phase-space distribution functions of InP MOSFETs for L_{ch} = (a) 30 and (b) 10 nm at an on-state gate voltage V_{on}, defined as the gate voltage corresponding to I_D = 3 mA/μm from the BMC simulations. The upper panels show the spatial distributions of the lowest-subband energy in the Γ valley and the total sheet electron density.

5.3.2 Characteristics for InGaAs MOSFETs

Figure 5.6 shows the I_D - V_G characteristics of $In_{0.53}Ga_{0.47}As$ MOSFETs computed at V_D = 0.5 V for L_{ch} = (a) 30, (b) 15, and (c) 10 nm. Note that the results in Fig. 5.6 are similar to those of InP MOSFETs. Namely, as L_{ch} becomes shorter than 15 nm, the subthreshold current determined by WMC simulation rapidly becomes larger than that by BMC simulation. This is due to the increased effect of SD direct tunneling. It is also found that the drain current at high gate voltages is almost the same for both simulations, regardless of L_{ch}, indicating that quantum reflection has a negligible influence on the on-state drive current, as already pointed out. However, there is an important difference between $In_{0.53}Ga_{0.47}As$ and InP MOSFETs as described below.

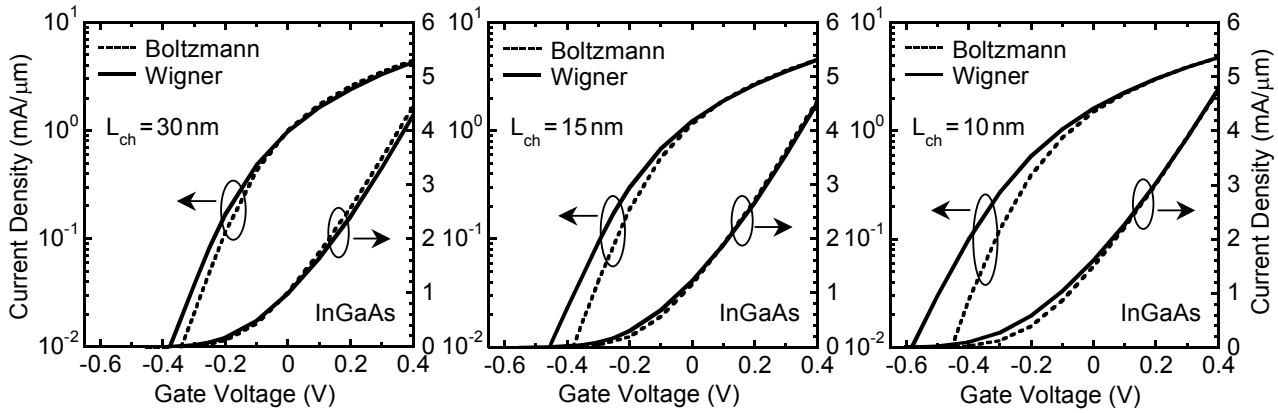

(a) (b) (c)

Fig. 5.6 I_D - V_G characteristics of $In_{0.53}Ga_{0.47}As$ MOSFETs computed at V_D = 0.5 V for L_{ch} = (a) 30, (b) 15, and (c) 10 nm, where the WMC and BMC results are plotted as solid and dashed lines, respectively.

Figure 5.7 shows the computed Boltzmann and Wigner distribution functions of $In_{0.53}Ga_{0.47}As$ MOSFETs with L_{ch} = (a) 30 and (b) 10 nm for a gate voltage corresponding to a threshold voltage V_{th}, where V_{th} was defined in the same manner as in the case of InP. Specifically, V_{th} = –0.3 V for L_{ch} = 30 nm and –0.4 V for L_{ch} = 10 nm. From Fig. 5.7(a), it is found that the Boltzmann and Wigner distribution functions are markedly similar not only in the source and drain regions but also in the channel region, as is the case with InP MOSFET. The result indicates that SD direct tunneling is nearly negligible for L_{ch} = 30 nm. On the other hand, for the shorter channel device with L_{ch} = 10 nm, an interference pattern is observed in the Wigner distribution function inside the channel region, as shown in Fig. 5.7 (b). Here, it should be pointed out that the interference pattern is more evident in the present $In_{0.53}Ga_{0.47}As$ MOSFET than in the InP MOSFET, indicating that SD direct tunneling becomes more notable in $In_{0.53}Ga_{0.47}As$ MOSFET with the lower effective mass. This is also confirmed in the upper panel for L_{ch} = 10 nm, i.e., the channel sheet density increases more drastically in the present WMC result for $In_{0.53}Ga_{0.47}As$ MOSFET.

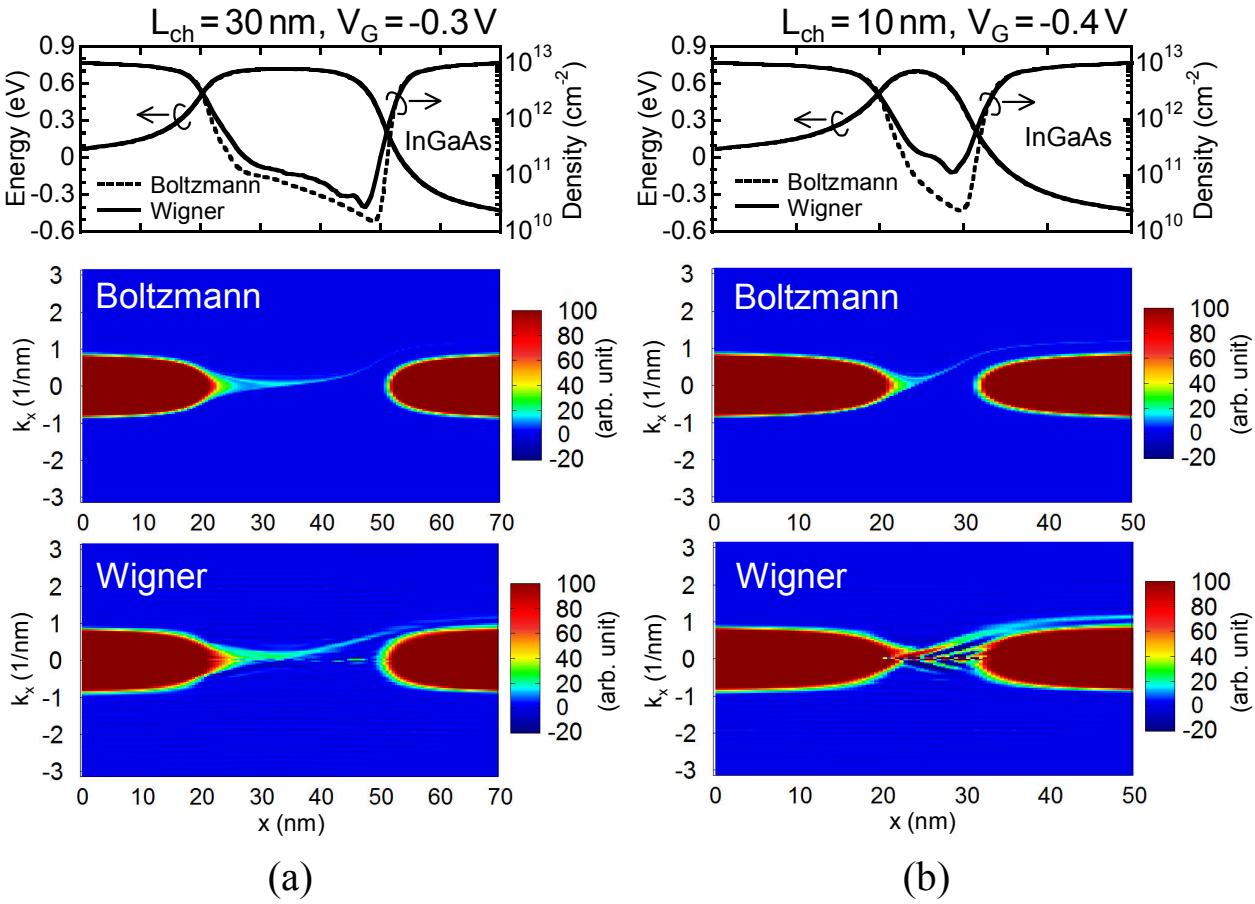

Fig. 5.7 Computed phase-space distribution functions of $In_{0.53}Ga_{0.47}As$ MOSFETs with L_{ch} = (a) 30 and (b) 10 nm at a threshold gate voltage V_{th}, defined as the gate voltage corresponding to I_D = 0.03 mA/μm obtained by BMC simulations. Here, Boltzmann and Wigner distribution functions are obtained by BMC and WMC simulations, respectively.

For an on-state gate voltage, there were only slight differences between the WMC and BMC distribution functions for either channel length (not shown here), as is the case in InP MOSFETs. This is because the main current is governed by thermal electron emission at the source-channel junction, which is a classical mechanism. This again indicates that quantum reflection is weak and leads to almost no reduction in the on-state drain current in III-V MOSFETs. Consequently, almost the same on-current was obtained using the WMC and BMC approaches, as show in Fig. 5.6.

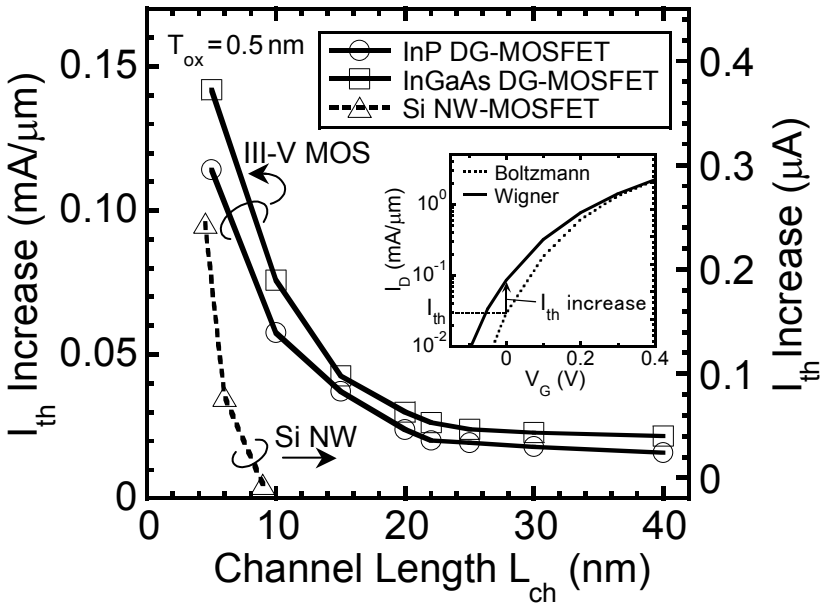

Fig. 5.8 Channel length dependence of the I_{th} increase. The I_{th} increase is calculated as the difference between the drain currents obtained by WMC and BMC simulations at $V_G = V_{th}$, as indicated in the inset. Here, V_{th} is defined as the gate voltage corresponding to $I_D = 0.03$ mA/μm obtained by the BMC simulations. The results for Si nanowire (NW) MOSFETs [9] are also plotted for comparison.

5.4 Discussion on Onset of SD Direct Tunneling

5.4.1 Comparison between InP, InGaAs, and Si

The difference in the significance of SD direct tunneling between $In_{0.53}Ga_{0.47}As$ and InP MOSFETs can be quantitatively evaluated by calculating the threshold current (I_{th}) increase as a function of L_{ch} as shown in Fig. 5.8. The method for calculating I_{th} increase is indicated in the inset of Fig. 5.8. It is found that the effect of SD direct tunneling is evident for $L_{ch} < 20$ nm for both III-V materials. Furthermore, as expected, $In_{0.53}Ga_{0.47}As$ MOSFETs indicate a larger I_{th} increase, but their difference in I_{th} increase from the InP counterparts is smaller than that expected from their significant difference in effective masses. We considered it due to the difference in channel potential profile at $V_G = V_{th}$ between the two channel materials.

Then, we compared the lowest subband energy profiles in the Γ valley for the $In_{0.53}Ga_{0.47}As$ and InP MOSFETs with $L_{ch} = 10$ nm as shown in Fig. 5.9, where the source Fermi energies, E_F^{InGaAs} and E_F^{InP}, are also indicated for reference. Since $In_{0.53}Ga_{0.47}As$ has the lower effective mass, or, lower DOS, the source Fermi energy of $In_{0.53}Ga_{0.47}As$ MOSFET is higher than that of InP MOSFETs. Here, it can be seen in Fig. 5.9 that $In_{0.53}Ga_{0.47}As$ MOSFET exhibits a higher potential barrier than in InP MOSFET at $V_G = V_{th}$. This is because of the higher source Fermi energy as mentioned above and the larger nonparabolicity in the Γ valley for $In_{0.53}Ga_{0.47}As$. That is, the larger nonparabolicity leads to a larger DOS with increasing energy, and, accordingly, makes the potential barrier required to remove electrons substantially higher, as compared with those for InP MOSFETs. As the potential barrier is higher as in $In_{0.53}Ga_{0.47}As$ MOSFETs, the number of electrons that can tunnel through it decreases,

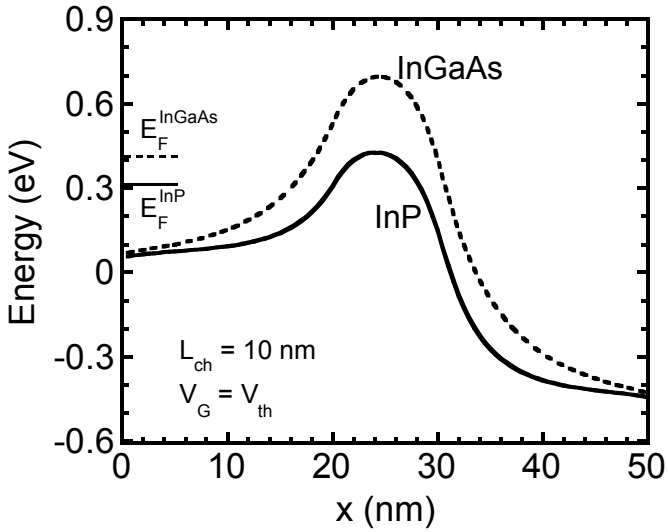

Fig. 5.9 Comparison of the lowest subband energy profiles in the Γ valley for $In_{0.53}Ga_{0.47}As$ and InP MOSFETs with L_{ch} = 10 nm at $V_G = V_{th}$. The source Fermi energies, E_F^{InGaAs} and E_F^{InP}, are also indicated for reference.

because the quasi-equilibrium distribution function in the source exponentially decays with increasing energy. Consequently, current due to SD direct tunneling is rather suppressed and drastic increase in the subthreshold leakage current is avoided.

The I_{th} increase due to SD direct tunneling for Si nanowire MOSFETs is also plotted as a dashed line in Fig. 5.8, which was calculated using a direct solution approach of the Wigner transport equation [9]. As described in chapter 4, SD direct tunneling has an impact on Si MOSFETs with channel lengths of smaller than 6–8 nm. As a result, the critical channel length for both $In_{0.53}Ga_{0.47}As$ and InP MOSFETs becomes approximately three times larger than that for Si MOSFETs, suggesting that SD direct tunneling can be a major obstacle in downscaling III-V MOSFETs into L_{ch} < 20 nm. Here, one can still observe in Fig. 5.8 the I_{th} increase in III-V MOSFETs with channel lengths longer than 20 nm, for which reason is described in subsection 5.4.2.

As we have pointed out in Fig. 5.9, the channel potential profile affects SD direct tunneling, and hence gate electrostatics enhanced by reducing the gate oxide thickness may suppress the current due to SD direct tunneling. To examine the role of the channel potential profile, we further simulated devices with T_{ox} = 1.0 nm, and compared their I_{th} increase with that for T_{ox} = 0.5 nm, as shown in Fig. 5.10. Since devices with T_{ox} = 1.0 nm are less immune to short-channel effects, the channel length must be larger than 10 nm to turn the devices off. As a result, the data point starts from L_{ch} = 10 nm for T_{ox} = 1.0 nm in Fig. 5.10. Predictably, the I_{th} increase is smaller for T_{ox} = 0.5 nm, indicating that the gate electrostatics enhanced by reducing the gate oxide thickness can indeed suppress SD direct tunneling current. To further examine such a role of the channel potential profile in the tunneling process, we practically depicted the variations due to T_{ox} in the potential barrier profiles as shown in Fig. 5.11, where L_{ch} = 20 nm and $V_G = V_{th}$. As can be seen in the figure, the potential barrier profiles become wider for T_{ox} = 0.5 nm owing to the enhanced gate electrostatics, and therefore, the tunneling probability decreases, which leads to the reduction in the I_{th} increase, as shown in Fig. 5.10.

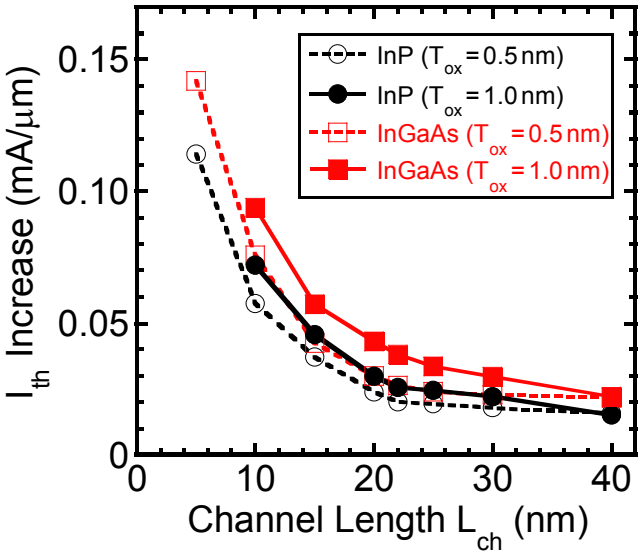

Fig. 5.10 Comparison of channel length dependences of I_{th} increase between T_{ox} = 1.0 and 0.5 nm. Both results for $In_{0.53}Ga_{0.47}As$ and InP MOSFETs are plotted.

5.4.2 Material choice to go beyond the end of the roadmap

Reducing the gate oxide thickness is effective in controlling SD direct tunneling as demonstrated above. However, it fails to suppress SD direct tunneling in III-V MOSFETs deeply scaled down to the channel length of 10 nm or below, as seen in Fig. 5.10. As discussed in refs. 15, 33 and 34, the introduction of a material with a heavier transport mass should be considered to drastically reduce SD direct tunneling. However, since the increase in transport mass decreases carrier mobility, on-state device performance will be degraded using materials with heavier transport mass. On the other hand, the increase in effective mass would help to reduce the DOS bottleneck

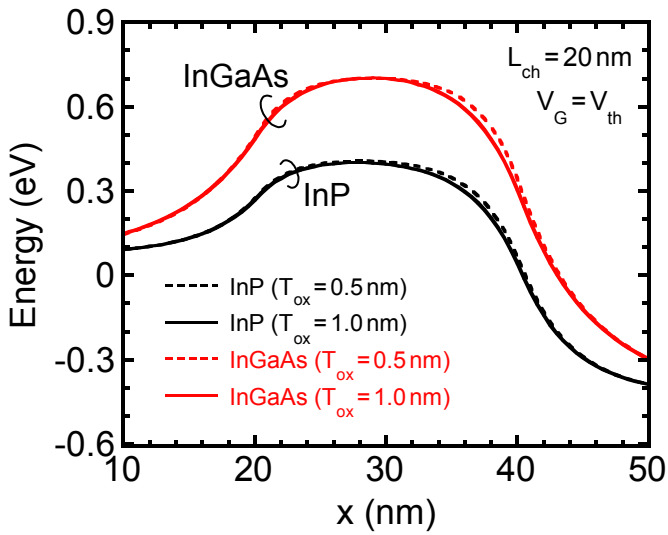

Fig. 5.11 Comparison of potential barrier profiles between T_{ox} = 1.0 and 0.5 nm, where L_{ch} = 20 nm and $V_G = V_{th}$. Both results for $In_{0.53}Ga_{0.47}As$ and InP MOSFETs are plotted.

problem in quantum capacitance limit, and thus, depending on the device structure and operating condition, the use of a material with a heavier transport mass could even lead to better on-state device performance [25,27]. Therefore, there may exist the optimum effective mass, or, the optimum band structure for both reducing SD direct tunneling and achieving the required on-state performance. In any case, the use of a material with a heavier transport mass might be one option to go beyond the end of the roadmap [34].

5.4.3 Explanation for the I_{th} increase in longer channel III–V MOSFETs

In this subsection, we describe the reason for I_{th} increase observed in III–V MOSFETs with channel lengths longer than 20 nm as shown in Fig. 5.3 (a), 5.6(a) and 5.8. These results are unusual in the common viewpoint. Therefore, the reason of the I_{th} increase for the longer channel length is investigated. First, as shown in Fig. 5.3 (a) and 5.6 (a), I_{th} increase for L_{ch} > 20 nm doesn't degrade subthreshold slope. Furthermore, Fig. 5.8 shows that the impact of I_{th} increase is almost constant for both InP and $In_{0.53}Ga_{0.47}As$ with L_{ch} > 20 nm, both of which indicates that I_{th} increase for L_{ch} > 20 nm may not be due to SD tunneling, since SD tunneling drastically degrades subthreshold slope and has strong dependency on the channel length. Also, it is shown in Fig. 5.4 (a) and 5.7 (a) that the gradient of the exponential decrease in electron density at source/channel or channel/drain junction is small in the WMC simulation compared to BMC simulation. At the same time, electron density in the channel region is slightly increased. These phenomena can be considered to be due to the electrons' penetration form source or drain into the channel region, which is one of the fundamental quantum phenomena as well as SD tunneling. Therefore, I_{th} increase in Fig. 5.8 may be separated into straight-line-approximation part, which corresponds to the electrons' penetration into the channel, and the remainder part, which corresponds to the SD

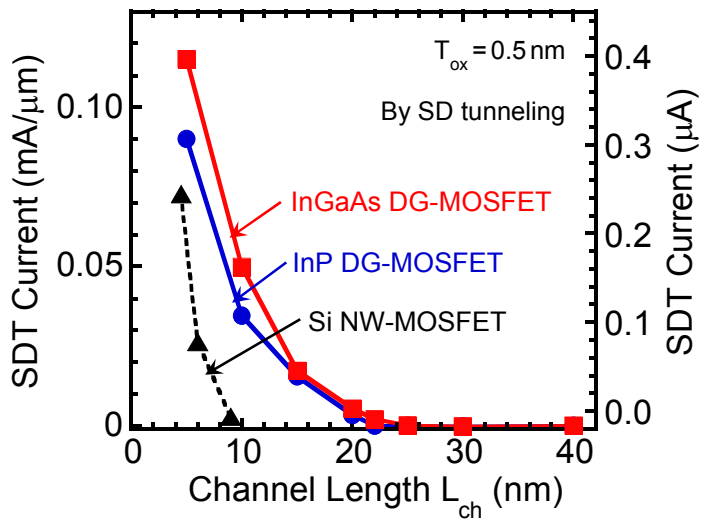

Fig. 5.12 Channel length dependence of SD direct tunneling calculated from I_{th} increase by subtracting straight-line-approximation part. It is found that the impact of the electrons' penetration into the channel is successfully removed. Here, V_{th} is defined as the gate voltage corresponding to I_D = 0.03 mA/μm obtained by the BMC simulations. The results for Si nanowire (NW) MOSFETs [9] are also plotted for comparison.

tunneling component. As a result, I_{th} increase for L_{ch} > 20 nm is well described with a straight line with almost no gradient and the remainder part which drastically increase for L_{ch} < 20 nm. The latter part corresponding to SD tunneling is shown in Fig. 5.12, which shows that the impact of SD tunneling is successfully separated from the impact of penetration.

Finally, it should be noted that the penetration of electrons into the channel doesn't lead to any degradation in the performance of the MOSFET, because it causes only a slight V_{th} shift to the lower-voltage side, as shown in Fig. 5.3 (a) and 5.6 (a). Also, since Si has larger transport mass compared to InP and $In_{0.53}Ga_{0.47}As$, Si MOSFET doesn't show the visible I_{th} increase due to the penetration.

5.5 Summary

The impact of SD direct tunneling in III-V MOSFETs was investigated using the WMC device simulator. The present results indicate that SD direct tunneling can be a major obstacle in downscaling III-V MOSFETs into L_{ch} < 20 nm. The gate electrostatics enhanced by reducing the gate oxide thickness was found to be effective for controlling SD direct tunneling. However, it failed to suppress SD direct tunneling in III-V MOSFETs deeply scaled down to the channel length of 10 nm or below. To go beyond the end of the roadmap, we will need selection of materials to suppress SD direct tunneling. It is suggested that the use of a material with a heavier transport mass might be one option.

References

[1] M. Radosavljevic, B. Chu-Kung, S. Corcoran, G. Dewey, M. K. Hudait, J. M. Fastenau, J. Kavalieros, W. K. Liu, D. Lubyshev, M. Metz, K. Millard, N. Mukherjee, W. Rachmady, U. Shah, and R. Chau, IEDM Tech. Dig. 2009, p. 319.

[2] J. A. del Alamo, Nature **479**, 317 (2011).

[3] Y. Yonai, T. Kanazawa, S. Ikeda, and Y. Miyamoto, IEDM Tech. Dig. 2011, p. 307.

[4] X. Zhou, Q. Li, C. W. Tang, and K. M. Lau, Appl. Phys. Express **5**, 104201 (2012).

[5] S. H. Kim, M. Yokoyama, N. Taoka, R. Iida, S. Lee, R. Nakane, Y. Urabe, N. Miyata, T. Yasuda, H. Yamada, N. Fukuhara, M. Hata, M. Takenaka, and S. Takagi, Appl. Phys. Express **5**, 014201 (2012).

[6] S. H. Kim, M. Yokoyama, N. Taoka, R. Iida, S. Lee, R. Nakane, Y. Urabe, N. Miyata, T. Yasuda, H. Yamada, N. Fukuhara, M. Hata, M. Takenaka, and S. Takagi, Appl. Phys. Lett. **98**, 243501 (2011).

[7] H. Kawaura, T. Sakamoto, and T. Baba, Appl. Phys. Lett. **76**, 3810 (2000).

[8] J. Wang and M. Lundstrom, IEDM Tech. Dig. 2002, p. 707.

[9] Y. Yamada, H. Tsuchiya, and M. Ogawa, IEEE Trans. Electron Devices, **56** 1396 (2009).

[10] M. Luisier, M. Lundstrom, D. Antoniadis, and J. Bokor, IEDM Tech. Dig. 2011, p. 251.

[11] H. Wakabayashi, T. Ezaki, M. Hane, T. Ikezawa, T. Sakamoto, H. Kawaura, S. Yamagami, N. Ikarashi, K. Takeuchi, T. Yamamoto, and T. Mogami,, IEDM Tech. Dig. 2004, p. 429.

[12] D. Querlioz, J. Saint-Martin, K. Huet, A. Bournel, V. Aubry-Fortuna, C. Chassat, S. Galdin-Retailleau, and P. Dollfus, IEEE Trans. Electron Devices **54**, 2232 (2007).

[13] D. Querlioz and P. Dollfus, *The Wigner Monte Carlo Method for Nanoelectronic Devices*., (New York, Wiley, 2010).

[14] D. Querlioz, H.-N. Nguyen, J. S.-Martin, A. Bournel, S. G.-Retailleau, P. Dollfus, J. Comput. Electron. **8**, 324 (2009).

[15] S. Koba, H. Tsuchiya, and M. Ogawa, Ext. Abs. of SISPAD 2011, 2011, p. 79.

[16] Y. Yonai, T. Kanazawa, S. Ikeda, and Y. Miyamoto, IEDM Tech. Dig. 2011, p. 307.

[17] X. Zhou, Q. Li, C. W. Tang, and K. M. Lau, Appl. Phys. Express **5**,104201 (2012).

[18] J. J. Gu, X. Wang, H. Wu, R. G. Gordon, P. D. Ye, IEEE Electron Device Lett. **34**, 608 (2013).

[19] S. Kim, M. Yokoyama, N. Taoka, R. Nakane, T. Yasuda, O. Ichikawa, N. Fukuhara, M. Hata, M. Takenaka, and S. Takagi, IEEE Trans. Electron Devices **60**, 2512 (2013).

[20] S. Koba, R. Aoyagi, and H. Tsuchiya, J. Appl. Phys. **108**, 064504 (2010).

[21] M. A. Khayer and R. K. Lake, IEEE Trans. Electron Devices **55**, 2939 (2008).

[22] E. Lind, M. P. Persson, Y.-M. Niquet, and L.-E. Wernersson, IEEE Trans. Electron Devices **56**, 201 (2009).

[23] N. Neophytou, T. Rakshit, and M. S. Lundstrom, IEEE Trans. Electron Devices **56**, 1377 (2009).

[24] K. Alam and R. N. Sajjad, IEEE Trans. Electron Devices **57**, 2880, (2010).

[25] N. Takiguchi, S. Koba, H. Tsuchiya, and M. Ogawa, IEEE Trans. Electron Devices **59** 206 (2012).

[26] Y. Lee, K. Kakushima, K. Natori, and H. Iwai, IEEE Trans. Electron Devices **59**,1037 (2012).

[27] K. Shimoida, Y. Yamada, H. Tsuchiya, and M. Ogawa, IEEE Trans. Electron Devices **60**, 117 (2013).

[28] M. V. Fischetti and S. E. Laux, IEEE Trans. Electron Devices **38**, 634 (1991).

[29] S. E. Laux, IEEE Trans. Electron Devices **54**, 2304 (2007).

[30] T. Mori, Y. Azuma, H. Tsuchiya, and T. Miyoshi, IEEE Trans. Nanotechnology **7**, 237 (2008).

[31] H. Tsuchiya, A. Maenaka, T. Mori, and Y. Azuma, IEEE Electron Device Lett. **31**, 365 (2010).

[32] C. Jacoboni and L. Reggiani, Rev. Mod. Phys. **55**, 645 (1983).

[33] S. S. Sylvia, H.-H. Park, M. A. Khayer, K. Alam, G. Klimeck, and R. K. Lake, IEEE Trans. Electron Devices **59**, 2064 (2012).

[34] S. R. Mehrotra, S.G. Kim, T. Kubis, M. Povolotskyi, M. S. Lundstrom, and G. Klimeck, IEEE Trans. Electron Devices **60**, 2171 (2013).

6. Conclusion

6.1 Summary

In this study, to conduct precise investigations and projections of device performance in the future integrated nanoscale devices, two MC simulators are developed to simulate scattering and quantum effects rigorously.

In chapter 2, a semi-classical MC simulator which can fully incorporate major scattering mechanisms for 2D electron gases (2DEGs), with increase in acoustic phonon deformation potential and spatial fluctuation of quantized subbands taken into account, is developed. To describe electron transport in the inversion-layers, electron states are obtained by self-consistently solving 1D Schrödinger equation and Poisson's equation along the gate-to-substrate direction, and the results are combined with the 1D MC simulator along the transport direction with the phonon scatterings and surface roughness scatterings.

The validity of the simulator is demonstrated by comparisons with the experimental results of electron mobility in a bulk MOSFET and SOI MOSFETs. As a result, it is shown that reliable scattering modeling is constructed.

In chapter 3, the simulator is extended to 2D semi-classical MC method for the DG MOSFETs with a significant improvement in the treatment of source and drain electrode, which enables us to estimate subthreshold characteristics. The quasi-ballistic transport parameters for ultrasmall DG MOSFETs is directly calculated by monitoring particle trajectories at the bottleneck point. The results have demonstrated that the ballistic transport in DG MOSFETs is enhanced due to channel length (L_{ch}) scaling until L_{ch} = 10 nm, but when L_{ch} is further scaled to less than 10 nm, SR scattering intensified by spatial fluctuation of quantized subbands drastically degrades ballistic transport. The results indicate that performance improvement is difficult even if MOSFETs are scaled less than 10 nm, which is very important viewpoint for the discussion of the miniaturization limits.

In chapter 4, a WMC simulator, which solves WTE using MC algorithm and incorporates not only scattering effects but also quantum transport effects more precisely, is developed for rigorously incorporating quantum transport effect along the source-to-drain direction. The WMC quantum simulation method is extended to MS simulation and effects of quantum transport in silicon DG MOSFETs with channel length of less than 10 nm are investigated. As a result, it is demonstrated that the quantum reflection makes significant differences in the microscopic features of electron transport and can even reduce the drain current at on-state. On the other hand, SD tunneling is shown to play a crucial role in the subthreshold properties of scaled MOSFETs with channel lengths of less than 6 nm.

In chapter 5, III–V MOSFETs with $In_{0.53}Ga_{0.47}As$ channel and InP channel are simulated and the applicability of WMC method to new channel material MOSFETs is demonstrated. Treatments of conduction band structure in III-V MOSFETs and polar optical phonon scattering intrinsic to the compound semiconductor materials are incorporated to WMC simulator in order to investigate the impact of SD direct tunneling in III–V channel MOSFETs. As a result, it was found that subthreshold current increase due to SD direct tunneling becomes more

remarkable in both $In_{0.53}Ga_{0.47}As$ and InP MOSFETs owing to its considerably lower effective mass compared to Si. The critical channel length for which a drastic increase in subthreshold current occurs due to SD direct tunneling was found to be about 20 nm for both $In_{0.53}Ga_{0.47}As$ and InP MOSFETs. Since this value is significantly larger than that for Si MOSFET, SD direct tunneling can be a major obstacle to downscale III-V MOSFETs into Lch < 20 nm. It is shown that we will need a material selection for suppressing SD direct tunneling while maintaining the high current drivability. The choice of a material with a heavier transport mass is also suggested.

To summarize the dissertation, MC simulators which can rigorously simulate scattering and quantum effects were developed and detailed discussion on the miniaturization limit of Si and III–V MOSFETs was made. It was demonstrated that miniaturization limit of gate length for Si MOSFET determined by SD tunneling is 6 nm, while if L_{ch} is scaled less than 10 nm, performance improvement can't be expected due to the drastically increased SR scattering occurred in ultrathin SOI channels. Furthermore, III–V channel MOSFETs, which have been expected to replace Si as a channel materials, were shown to be more vulnerable to SD tunneling and it can be a major obstacle to downscale III-V MOSFETs into L_{ch} < 20 nm, which is three times longer than that for Si MOSFETs. Therefore, the conclusion of this dissertation is as follows. To go beyond the end of the roadmap, a material selection so that SD direct tunneling can be removed and required on-state performance is achieved is needed. It is also suggested that the better choice for post silicon materials might be heavier transport mass materials.

6.2 Recommendations for future work

There are still many significant matters to be dealt for the future work. I note here what I think is important among them.

6.2.1 Improvement of scattering treatment in III–V channel MOSFETs

In chapter 5, scattering rates for 3DEG are employed to simulate the III–V channel DG MOSFETs to focus on the quantum transport effect. On the other hand, to make a more realistic device performance projection of on-state characteristics, a more reliable scattering treatment is necessary, as shown in chapter 3. For instance, Prange-Nee term employed in the scattering treatment for silicon MOSFETs assume no wave function penetration into the insulator region. However, more wave function penetration into the insulator is expected for III–V MOSFETs with high-k insulator [1]. So more advanced SR scattering treatment will be indispensable. Also, polar optical phonon scattering for 2DEG must be incorporated in the simulation.

6.2.2 Development of a 3D MSWMC simulator

Next, because electrons in FinFET will have the natures as 1DEGs if fin height is scaled less than 10nm, development of a 3D MSWMC simulator with a precise treatment of 1DEG will be necessary in the future. Electron transport in nanowire FETs is also a 1DEG problem. As for development of 1D phase-coherent simulation technique, Dr. Yamada [2] made a simulator of nanowire FETs with direct solution of WTE. However, as was discussed in chapter 4, direct solution of WTE has problems inherent with the treatment of diffusion term and scattering effects. Therefore, WMC approach is effective to improve such points as shown in this thesis. I

have conducted the formulation of scattering rates for 1DEG with Mr. Nagai of our laboratory, and 3D MSWMC simulator is completed except for treatment of some scattering mechanisms.

6.2.3 Inclusion of atomistic band structure treatment

In the dissertation, bulk effective mass approximation with a nonparabolicity is used for the expression of band structure. Although nanoscale device performance predicted with bulk band parameters is qualitatively reliable, quantitatively accurate prediction of extremely miniaturized devices should consider the band structures obtained by atomistic approach such as first-principles calculation and tight binding method [3].

6.2.4 Simulation of FETs with new principles and new concepts

Also, devices based on the new concepts, such as tunneling FETs (TFETs) and impact ionization MOSFETs (I-MOSFETs), which are called steep-slope FETs, should be considered.

A. TFETs

Device structure and its band diagram are shown in Fig. 6.1 and 6.2. TFETs utilize band-to-band tunneling (BTBT) and aims at achieving subthreshold slope of less than 60mV/dec. For WMC approach, a simulation of TFETs is considered a difficult task, because WTE used in WMC method is based on effective mass approximation, and BTBT is not included in principle.

One of the solution for solving such problem is to use extend Wigner function formalism with k.p Hamiltonian [4]. However, even if such approach is taken, treatment of scattering is a very difficult question to answer. Generally speaking, it is a difficult deal to incorporate mechanisms which is not included in principle itself. Therefore, for the simulation and performance prediction of TFET, I recommend using NEGF simulation, which can incorporate atomistic band structure and BTBT tunneling in principle.

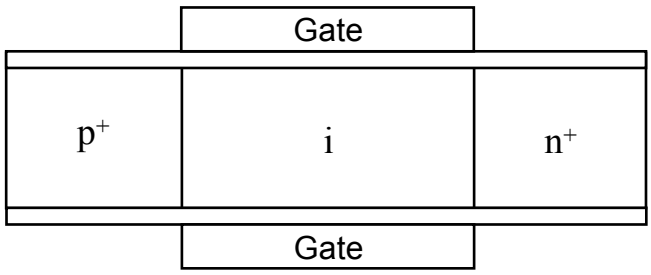

Fig. 6.1 Device structure of TFET. Unlike conventional MOSFETs, acceptors are injected to the source for n-type TFET.

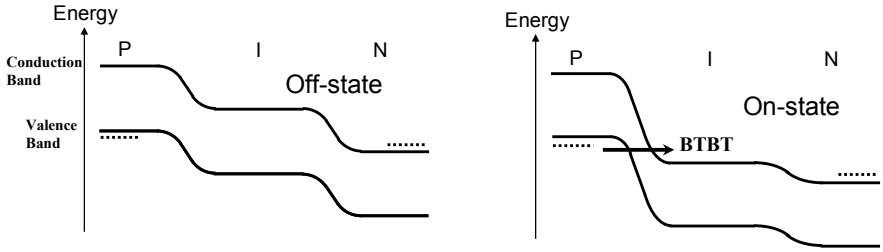

Fig. 6.2 Band diagram of TFET for off-state and on-state. In off state, intrinsic channel hinders BTBT and off-current is sufficiently suppressed. In contrast, in on state, BTBT takes place in source/channel junction, which makes steep slope in I_D–V_G characteristics.

B I-MOSFETs

An I-MOSFET is a transistor which make use of avalanche breakdown, obtaining subthreshold slope of less than 60 mV/dec [5, 6]. Typical device structure of I-MOSFET is shown in Fig. 6.3. MC simulation technique has a high degree of affinity for IMOSFETs, because impact ionization can be characterized using 'rate' of impact ionization. As shown in the modeling of scattering mechanisms, MC simulation has an advantage in treating any kinds of rates with dimension of s^{-1}. Therefore, if reliable formulation of impact ionization rate is incorporated in the MC simulator developed in this thesis, high reliability performance prediction of nanoscale I-MOSFETs is expected.

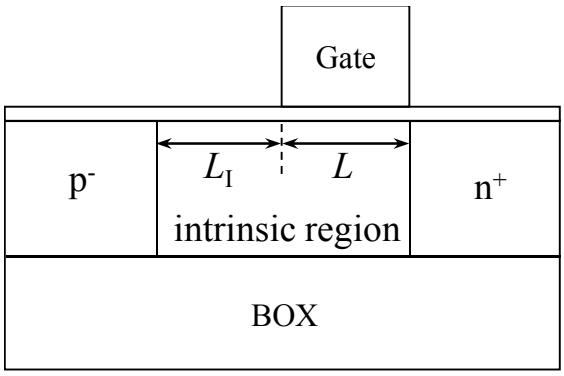

Fig. 6.3 Typical device structure of I-MOSFET [5]. Gate is underlapped in the channel region to make the electric field in the L_I higher, which makes avalanche breakdown easier to take place.

C Junctionless transistor (*JLT*)

JLT is an example of the new concept transistors [7]. As devices are scaled down, fabrication of p/n junction with extremely higher quality is required, which is becoming more and more difficult. On the other hand, device structure of JLT is shown in Fig. 6.4 (b). JLT has no junctions, which is the origin of its naming and makes fabrication process simpler. To switch off the JLT, high gate controllability is a must. Therefore, JLTs must be fabricated with multi-gate structures. On the other hand, the impact of ionized impurities in the channel region is a hotly-debated topic. An experimental result shows that almost the same performance as conventional MOSFETs

can be obtained with a JLT [7], but the detailed discussion and the performance predictions of the JLTs with various sizes and structures are highly expected.

It is worth noting that simulations of JLT with DG structures can readily be conducted using the simulator developed in this dissertation. Also, with a 3D MSWMC simulator introduced in subsection 6.2.2, Fin- or nanowire-JLT can also be readily simulated. Therefore, device performance projections of JLTs will be one of the main topics of future work.

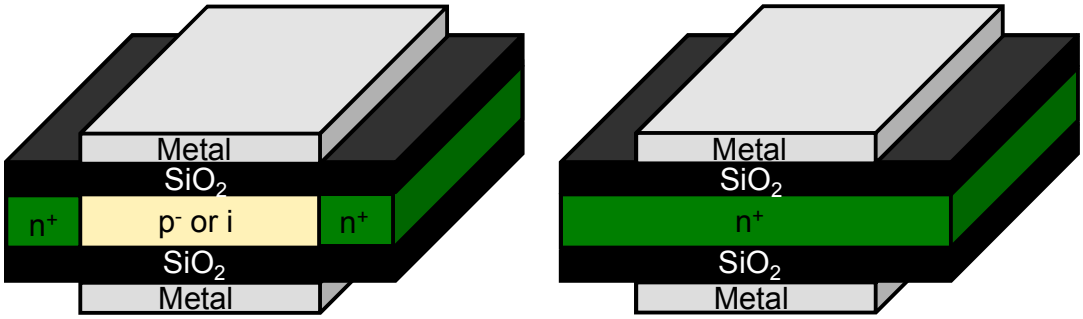

Fig. 6.4 Device structure of (a) conventional MOSFET and (b) JLT.

References

[1] D. Lizzit, D. Esseni, P. Palestri and L. Selmi, IEDM Tech. Dig., 2013, p. 120.

[2] Y. Yamada, H. Tsuchiya, and M. Ogawa, IEEE Trans. Electron Devices **56**, 1396 (2009).

[3] J. C. Slater and G. F. Koster, Phys. Rev. **94**, 1498 (1954).

[4] L. Demeio, L. Barletti, A. Bertoni, P. Bordone, and C. Jacoboni, Physica B **314**, 104 (2002).

[5] K. Gopalakrishnan, P. B. Griffin, and J. D. Plummer, IEEE Trans. Electron Devices **52**, 69 (2005).

[6] K. Gopalakrishnan, R. Woo, C. Jungemann, P. B. Griffin, and J. D. Plummer, IEEE Trans. Electron Devices **52**, 77 (2005).

[7] J.-P. Colinge, C.-W. Lee, A. Afzalian, N. D. Akhavan, R. Yan, I. Ferain, P. Razavi, B. O'Neill, A. Blake, M. White, A.-M. Kelleher, B. McCarthy, and R. Murphy, Nature Nanotech. **5**, 225 (2010).

Appendix

A. Transfer matrix (TM) method

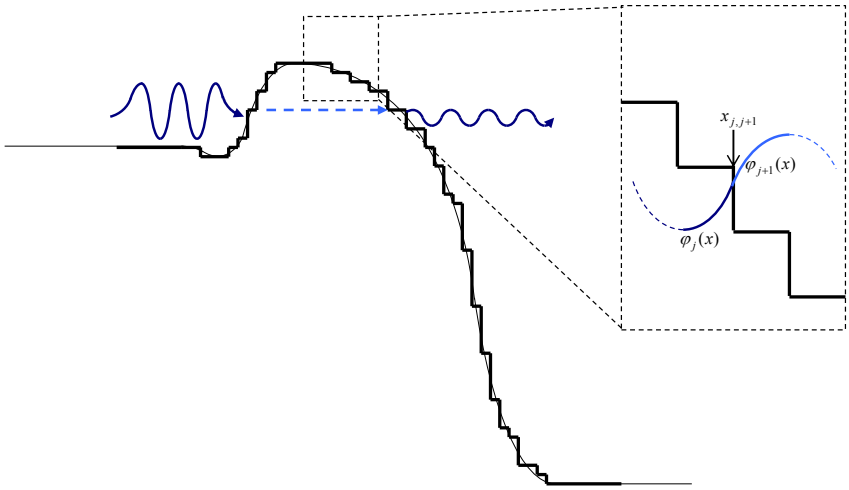

Fig. A.1 Schematic picture of TM method, in which potential energy profiles are discretized and transmission and reflection probability at the region boundary is calculated.

TM method divides continuous potential profiles into step-like regions and obtains the transmission probability of electron waves from source to drain. Boundary conditions between regions are given as following equations:

$$\varphi_j(x_{j,j+1}) = \varphi_{j+1}(x_{j,j+1}), \tag{A.1}$$

$$\left.\frac{d\varphi_j}{dx}\right|_{x=x_{j+1}} = \left.\frac{d\varphi_{j+1}}{dx}\right|_{x=x_{j+1}}, \tag{A.2}$$

where j is a mesh, $x_{j,j+1}$ describes the position of the boundary between mesh j and j+1, and $\varphi_j(x)$ is a wave function defined for the mesh j. These equations mean that wave function and its gradient defined for each mesh are smoothly connected at the boundary of adjacent discretized mesh points. By configuring discretized mesh small enough, the method can solve Schrodinger's equation rigorously.

A wave function for region j is described as the sum of rightward and leftward plane waves.

$$\varphi_j(x) = C_j^+ e^{ik_j x} + C_j^- e^{-ik_j x}, \tag{A.3}$$

where

$$k_j = \frac{\sqrt{2m^*(E - V_j)}}{\hbar}$$

and V_j is a potential energy at the point $x = x_j$. If boundary conditions (A.1) and (A.2) are applied to the wave function (A.3), coefficients of the wave functions in the region j and j+1 are obtained as follows.

$$\begin{bmatrix} C_{j+1}^+ \\ C_{j+1}^- \end{bmatrix} = M^{j+1,j} \begin{bmatrix} C_j^+ \\ C_j^- \end{bmatrix}, \tag{A.4}$$

where $M^{j+1,j}$ is called transfer matrix between regions j and j+1, and described as following equation.

$$M^{j+1,j} = \frac{1}{2}\begin{bmatrix} \left(1+\frac{k_j}{k_{j+1}}\right)e^{i(k_j-k_{j+1})x_{j,j+1}} & \left(1-\frac{k_j}{k_{j+1}}\right)e^{-i(k_j+k_{j+1})x_{j,j+1}} \\ \left(1-\frac{k_j}{k_{j+1}}\right)e^{i(k_j+k_{j+1})x_{j,j+1}} & \left(1+\frac{k_j}{k_{j+1}}\right)e^{-i(k_j-k_{j+1})x_{j,j+1}} \end{bmatrix}. \tag{A.5}$$

By multiplying the transfer matrices inside the simulation region, transfer matrix from the left boundary from the right boundary can be obtained. That is,

$$\begin{bmatrix} C_n^+ \\ C_n^- \end{bmatrix} = M^{n,m-1}M^{n-1,m-2}\cdots M^{3,2}M^{2,1}\begin{bmatrix} C_1^+ \\ C_1^- \end{bmatrix}. \tag{A.6}$$

To obtain transmission probability from the left boundary, electron wave can be assumed to be injected from region index 1 with amplitude of 1, reflected with amplitude r, and transmitted to region index n with amplitude of t. Therefore,

$$\begin{bmatrix} t \\ 0 \end{bmatrix} = M^T\begin{bmatrix} 1 \\ r \end{bmatrix} = \begin{bmatrix} M_{11}^T & M_{12}^T \\ M_{21}^T & M_{22}^T \end{bmatrix}\begin{bmatrix} 1 \\ r \end{bmatrix} \tag{A.7}$$

is obtained. If this equation is solved regarding r and t,

$$r = -\frac{M_{21}^T}{M_{22}^T} \tag{A.8}$$

and

$$t = M_{11}^T - \frac{M_{12}^T M_{21}^T}{M_{22}^T} = \frac{M_{11}^T M_{22}^T - M_{12}^T M_{21}^T}{M_{22}^T} = \frac{\left|M^T\right|}{M_{22}^T} \tag{A.9}$$

is obtained. Here, mathematical formula for determinant is utilized as

$$\begin{aligned} \left|M^T\right| &= \prod_{j=1}^{n-1}\frac{1}{4}\left[\left(1+\frac{k_j}{k_{j+1}}\right)^2 - \left(1-\frac{k_j}{k_{j+1}}\right)^2\right] \\ &= \prod_{j=1}^{n-1}\frac{k_j}{k_{j+1}} = \frac{k_1}{k_n}. \end{aligned} \tag{A.10}$$

As a result, transmission probability t is described as

$$t = \frac{k_1}{k_n}\frac{1}{M_{22}^T}. \tag{A.11}$$

Note that this is not transmission probability for probability current density. If one needs to obtain current density under a certain applied bias voltage, transmission probability for probability current density $T(E)$ can be calculated according to the following expression.

$$T(E) = \frac{v_n}{v_1}|t|^2 = \frac{\hbar k_n / m^*}{\hbar k_1 / m^*}\left|\frac{k_1}{k_n}\frac{1}{M_{22}^T}\right|^2 = \frac{k_1}{k_n}\left|\frac{1}{M_{22}^T}\right|^2, \tag{A.12}$$

In general, $k_1 \neq k_n$ under an applied bias voltage.

Acknowledgments

First and foremost, I would like to express my sincerest gratitude to my direct supervisor Dr. Tsuchiya, Associate Professor of Faculty of Engineering, Kobe University. This dissertation is accomplished under kind, precise, and stimulating supervisorship by Dr. H. Tsuchiya. This dissertation would not have been completed without his help. Every time I confronted problems, his precise pieces of advice helped solve the problems.

I would like to thank Professor Y. Yasaka, Professor H. Takeno, and Professor M. Numa for their helpful suggestions and comments on an earlier draft of this dissertation. Their comments and suggestions must have enhanced the quality of this dissertation.

I would also like to thank Professor M. Ogawa and Dr. S. Souma of our laboratory for their helpful pieces of advice and their effort to make better research environment. I would like to thank Dr. K. Sasaoka and Mr. T. Ijichi for their contribution to the laboratory environment maintenance.

Useful pieces of advice by Dr. N. Mori and Dr. Y. Kamakura, Associate Professor of Faculty of engineering, Osaka University, and Dr. S. Uno, Associate Professor of College of Science and Engineering, Ritsumeikan University contributed a lot during our collaborative work. I would like to thank them.

During my initial stage of study, I am really fortunate to have a lot of help and guidance from my senior colleagues Mr. Maenaka, Mr. Wang, Mr. S. Sawamoto and Dr. Y. Yamada. I would also like to thank my same-year roommates Mr. R. Aoyagi, Mr. H. Hosokawa, Mr. N. Takiguchi and Mr. H. Hayashi. I had a comfortable laboratory life thanks to them. I also thank Mr. K. Nagai, Mr. R. Ishida and Mr. M. Ohmori for their invaluable aids during the research.

I gratefully acknowledge many fruitful discussions with many research associates from STARC project.

This work was financially supported by Grants-in-Aid for Scientific Research from the Japan Society for the Promotion of Science (JSPS), the Semiconductor Technology Academic Research Center (STARC), and the Japan Science and Technology Agency (JST)/CREST.

Doctor Thesis, Kobe University
“Development of Monte Carlo Simulators for Integrated Nanoscale Devices”, 95 pages
Submitted on January 24, 2014

© Shunsuke Koba
All Rights Reserved, 2014